LABORATORI NAZIONALI DI FRASCATI
SIS – Pubblicazioni

LNF-02/027 (Thesis)
29 Novembre 2001

Università degli Studi di Roma
La Sapienza
Facoltà di Ingegneria

Dottorato di Ricerca in Elettromagnetismo Applicato
e Scienze Elettrofisiche
XII Ciclo

BEAM-BEAM INTERACTION EFFECTS IN DAΦNE

Tesi di Dottorato di
Manuela Boscolo

Tutore:
Prof. L. Palumbo
Correlatore:
Dott. Mikhail Zobov

Coordinatore dottorato:
Prof. Giorgio Gerosa

Gennaio 2000

Contents

List of Figures

List of Tables

Introduction

DAΦNE is a double annular electron-positron collider in operation at the Laboratori Nazionali di Frascati (LNF) of the INFN at the center-of-mass energy of 1.020 GeV, corresponding to the Φ-meson resonance that decays mainly in K mesons. The study of neutral K mesons is pointed to the investigation of the small CP symmetry violation present in nature which states that any reaction must not change if it undergoes a simultaneous mirror reflection and change of all particles into their antiparticles.

The accurate measurement of these rare phenomena require a very high luminosity . A value of about $10^{32}\mathrm{cm}^{-2}\mathrm{s}^{-1}$ is necessary in oder to improve by one order of magnitude the accuracy of the actual best measurement. This is a very demanding task for a collider at such low energies.

One of the intrinsic limit for the luminosity is the beam-beam interaction effect. It essentially consists in the force experienced by a particle in one beam due to the electromagnetic interaction with all the particles in the opposite one during collisions. Being a highly nonlinear interaction it is very difficult to be predictive on its effects and it is one of the most challenging problems to study on DAΦNE .

The dissertation is organized as follows. The first Chapter contains a description of the DAΦNE project with particular attention to the main rings optics, interaction region and luminosity measurement.

A basic description of the beam-beam interaction is discussed in Chapter 2. The first part is dedicated to the derivation of the beam-beam force and to its linearization which brings to the definition of the tune shift. In the second part an Hamiltonian analysis is used in order to study the beam-beam resonances and tune spread.

Chapter 3 describes the models that are used to simulate the beam-beam interaction with particular attention to the code I have used for DAΦNE .

Simulation results are presented in the next two Chapters. In Chapter 4 a detailed analysis has been performed to search for the DAΦNE working point with one interaction point. The performances of the working point have been studied carefully with the simulations in comparison with the experimental results in order to investigate the influence of various beams parameters on the luminosity and lifetime. Chapter 5 is dedicated to the search for a working point with two interaction points.

Experimental results are shown in Chapter 6 with particular attention on the luminosity optimization and beam-beam effects.

Chapter 1

The DAΦNE Collider

In this chapter the Frascati Φ-factory DAΦNE is described and the physics to be done with is very briefly summarized.

1.1 Physics at DAΦNE

Large high energy accelerators provide tools for investigation at the frontiers of our knowledge in sub-nuclear physics by probing the ultimate constituents of matter within always smaller space-time regions, and by generating new patterns of matter at always increasing energies. A complementary approach to the understanding of the fundamental properties of nature is the study at a very high degree of precision of rare phenomena, which clarify critical items of the theories and open the possibility of discriminating between different models of the physical reality. In order to follow the latter line of research in sub-nuclear physics, accelerators capable of delivering beams of extremely high intensity and accurate energy calibration are needed; in this way a wide variety of data even on the rarest phenomena can be obtained. DAΦNE[1] (Double Annular For Nice Experiments) is of this kind of accelerators, dedicated to the abundant production of Φ particles, coming from the annihilation of electrons and positrons at the energy of the Φ resonance. The Φ particle is of course unstable with a very short lifetime, it decays in lower energy particles, among which the K mesons. These particles have been discovered in 1947 and till then have shown new features. The study of neutral K mesons behavior is pointed to the study of the violation of the CP symmetry, which states that any reaction must not change if it undergoes a simultaneous mirror reflection and change of all particles into their anti-particles. The detailed measurement of the fundamental parameters of direct

CP violation $\mathcal{R}e(\frac{\epsilon'}{\epsilon})$ and its inclusion into a conceptual framework is one of the most challenging open problems in physics, and it represents the main research program of KLOE [2] (K LOng Experiment) at DAΦNE.

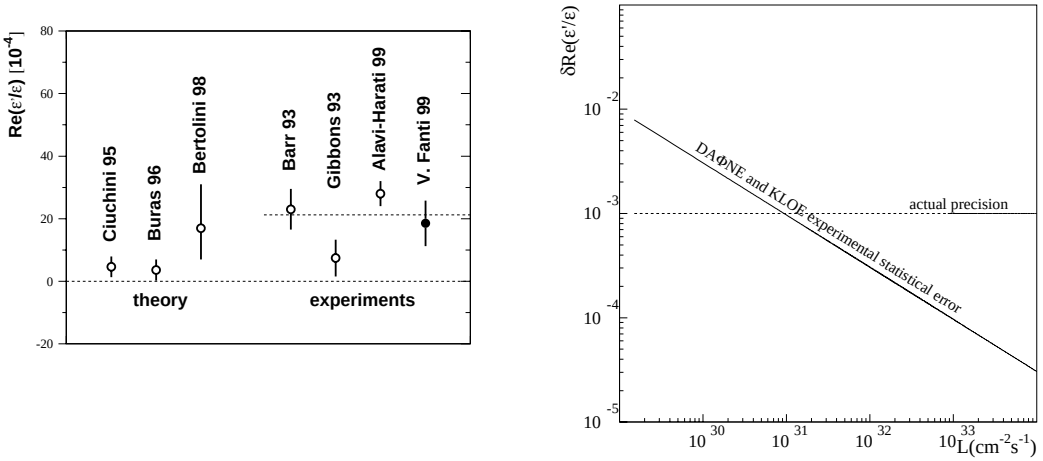

(a) (b)

Figure 1.1: (a) Review of the present measurements and predictions; (b) Behavior of the statistical error as a function of the instantaneous luminosity by assuming one year data taking. The following typical values have been used: $\sigma_\phi = 3.3\mu b$, $B(\phi \to K_L K_S) \simeq 0.3$, $B(K_L \to \pi\pi) \simeq 10^{-3}$ and the revelation efficiency Eff=0.3;

Particularly KLOE aims to measure

$$\mathcal{R}e(\frac{\epsilon'}{\epsilon}) = \frac{1}{6}(R-1) \tag{1.1}$$

where R is the double ratio

$$R = \frac{B(K_L \to \pi^+\pi^-)}{B(K_L \to \pi^0\pi^0)} / \frac{B(K_S \to \pi^+\pi^-)}{B(K_S \to \pi^0\pi^0)}. \tag{1.2}$$

The statistical error on $\mathcal{R}e(\frac{\epsilon'}{\epsilon})$ are dominated by the error on the smallest branching ratios $B(K_L \to \pi\pi)$, the ones related to the CP violating processes:

$$\delta\mathcal{R}e(\frac{\epsilon'}{\epsilon}) \simeq \frac{1}{6}\frac{\delta B(K_L \to \pi\pi)}{B(K_L \to \pi\pi)} \simeq \frac{1}{6}\frac{\delta N_{long}}{N_{long}} \simeq \frac{1}{6}\frac{1}{\sqrt{N_{long}}} \tag{1.3}$$

where N_{long} is the number of detected $K_L \to \pi\pi$ and is given by

$$N_{long} = L\sigma_\phi B(\phi \to K_L K_S) B(K_L \to \pi\pi) Eff \tag{1.4}$$

In Figure 1.1 (b) is shown the behavior of the statistical error as a function of the instantaneous luminosity by assuming one year of data taking. In Figure 1.1 (a) it is also shown the accuracy that recently has been obtained by KTEV [8] and NA48 [9] collaborations. It appears that a luminosity of about 10^{31} (which corresponds to 10^2 pb^{-1} for one year of data taking) is required in order to reach this sensitivity.

However, CP violation and K meson physics are not the only goals of the DAΦNE project: the abundant production of K mesons opens a wide range of experiments in nuclear physics, with unique characteristics of energy resolution and kind of observable reactions. A second experiment, FINUDA (FIsica NUcleare a DAΦNE) [3], will be installed on the second interaction point of the DAΦNE main rings to perform studies on the spectroscopy and decay modes of hypernuclei, where a nucleon has been replaced by a baryon made of strange quarks. In DAΦNE λ hypernuclei will be produced by stopping K mesons of known energy inside nuclear targets.
As FINUDA will roll-in later than KLOE, in the meanwhile the DEAR [4] experiment occupies the second IP. Due to its very high nominal stored currents DAΦNE is also an interesting high flux source of synchrotron radiation in the UV and soft X-ray wavelength region. There will be installed a small number of synchrotron radiation beam-lines from dipoles and wigglers of DAΦNE main ring.

1.2 DAΦNE Design Criteria and Project Overview

The construction and installation phase of the Frascati Φ-factory DAΦNE have been completed in autumn 1997. As I briefly discussed in the latter Section 1.1, this machine is optimized to explore in detail the physics of the reaction

$$e^+ + e^- \rightarrow \Phi \rightarrow K_S + K_L \tag{1.5}$$

The success of such an exploration demands a large number of events, which in turn demands high average luminosity and reliability of operation. The word "factory" is meant to emphasize these two requirements. The peak luminosity that DAΦNE aims to achieve is on the scale 10^{32} cm^{-2}s^{-1}, more than one order magnitude higher than in existing colliders at that energy. Thus, assuming an "experimental" year of 10^7 s, this machine is expected to deliver an integrated luminosity of 10^3 pb^{-1} per year in the *phase one* working with thirty bunches. The approach of DAΦNE to high luminosity, multibunch flat beams with a very high current stored in two separate rings, is common to the other two existing factories, KEK-B and PEP-II. The electron and positron beams collide in one of two potential Interaction Points

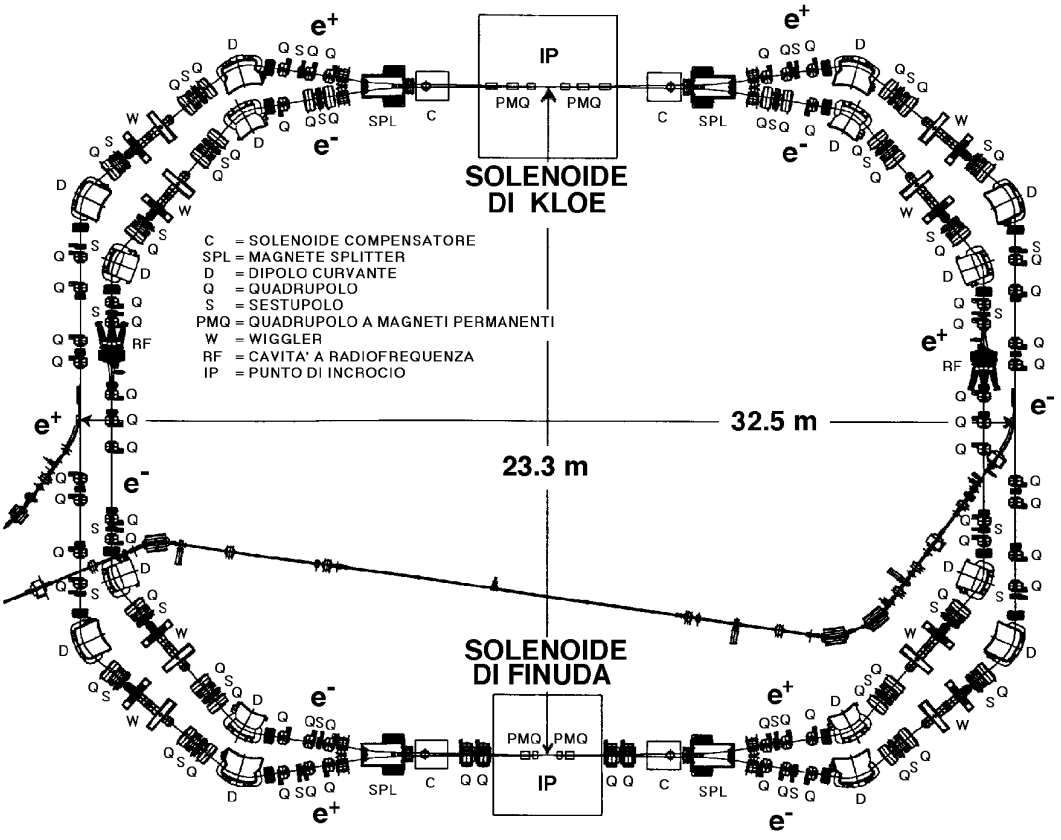

Figure 1.2: DAΦNE Main Rings Layout.

(IP). The crossing at a horizontal angle reduces the effect of parasitic collisions and it should allow to store up to 120 bunches per ring, corresponding to a colliding frequency of 368.26 MHz. For DAΦNE the horizontal crossing angle is 25 mrad satisfying the physical constraint

$$\frac{\theta\sigma_z}{\sigma_x} \ll 1$$

where θ is the crossing angle, σ_z and σ_x are the longitudinal and radial beam size respectively. The high rate of bunch collisions relaxes the single bunch luminosity parameters. The single bunch luminosity design value is $4.3 \cdot 10^{30}\mathrm{cm}^{-2}\mathrm{s}^{-1}$ with 44 mA per bunch. The DAΦNE main rings layout is shown in Figure 1.2 and the main design parameters have been reported in Table 1.1.

Electrons and positrons are stored in two symmetric separate rings. This is mainly due to the necessity of avoiding 240 IPs that there would be if the two beams circulated in the same ring. Flexibility is technically obtained by independently

Table 1.1: DAΦNE design parameters

Energy[GeV]	0.51
Maximum Luminosity[$\mathrm{cm}^{-2}\mathrm{s}^{-1}$]	$5.3 \cdot 10^{32}$
Single Bunch Luminosity[$\mathrm{cm}^{-2}\mathrm{s}^{-1}$]	$4.4 \cdot 10^{30}$
Trajectory length[m]	97.69
Emittance,$\varepsilon_x/\varepsilon_y$[mm $\cdot$ mrad]	1/0.01
β-function β_x^*/β_y^*[m]	4.5/0.045
Transverse size σ_x^*/σ_y^*[mm]	2/0.02
Beam-beam tune shift $\xi_x\xi_y$	0.04/0.04
Crossing angle θ_x[mrad]	25
RF frequency[MHz]	368.26
Number of bunches	120
Minimum bunch separation [cm]	81.4
Particles/bunch [10^{10}]	8.9
RF Voltage [MV]	0.250
Bunch length [cm]	2.5
Synchrotron radiation loss [KeV/turn]	9.3
Damping time τ_z/τ_x[ms]	17.8/36.0

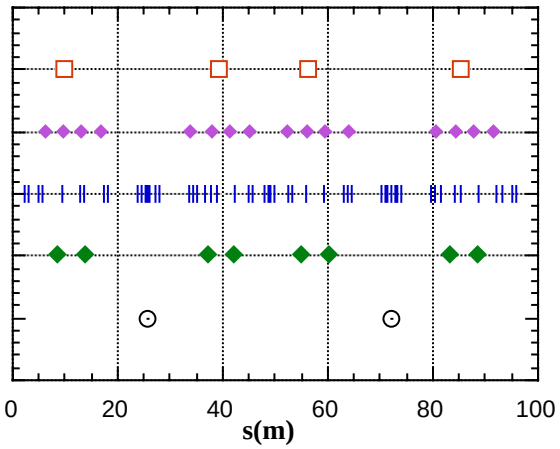

Figure 1.3: Position of the magnetic elements and of the two IPs along one of the two rings, from the bottom: IP, dipoles, quadrupoles, sextupoles and wigglers.

powering all quadrupoles and sextupoles.

Electrons and positrons intersect each other in two Interaction Regions (IR), where the beams travel in the same vacuum chamber, passing off-axis in the low-β quadrupoles. It can be shown that the betatron amplitude grows with the distance s from the minimum value in the low-β insert along the drift spaces on either side according to [5]

$$\beta(s) = \beta(0)[1 + s^2/\beta^2(0)].$$

The smaller $\beta(0)$ is, the faster $\beta(s)$ will grow with distance from the crossing point. So the low-β insertions produce only a localized region of very low vertical β-function β_y and they are needed to achieve high luminosity , as it is inversely proportional to β_y. They are placed as near as possible to the detector. The point of minimum beam cross section is placed exactly at the crossing point. At the end of each IR the beams are separated by 12 cm and a splitter magnet drives the two beams in the corresponding rings, with two independent vacuum chambers.
The periodical structure of the main ring consists of four arcs. The complexity of the machine and its main elements can be observed in Figure 1.2 and in Figure 1.3. The straight sections of the IRs are interleaved with by two sections used for injection, RF cavity and feedback kickers. The arc cell has been called BWB (Bending-Wiggler-Bending) and it is quasi-achromatic. The 1.8 T wiggler is 2 m long in the region of maximum dispersion.
The challenging parameter is the very high current, to be reached when all the 120 buckets are filled. Multibunch instabilities will have to be cured as the number of stored bunches will increase. Special RF cavities have been developed to allow stable

high current-multibunch operation; they have low parasitic high order modes (HOM) content. The RF cavities are one per ring and are normal conducting copper single cells, with a system of HOM damping waveguides which couple out and dissipate the HOM energy induced by the beam on external 50 Ω loads.
A longitudinal bunch-by-bunch feedback system has been implemented to damp residual oscillations of the beam. It consists of a modular time domain system employing digital techniques. A timing system provides synchronization of the RF cavities of the main ring, the accumulator's RF phase, the linac's gun trigger, the injection/extraction kickers in the accumulator ring and the main rings' injection kickers in order to fill the selected bucket with a precision of the order of picoseconds.

1.3 Main Ring Structure

The circumference of each ring is very short, about 100 m, in order to increase the single bunch luminosity and reduce the damping time. This makes the lattice extremely compact and has allowed the installation of the machine in the building of the ADONE accelerator shut down in 1993.
The two 10 m long IRs are limited by the splitter magnets used to separate the beams. In each ring two sections connect the IRs: an outer one called *Long* and an inner one called *Short*. Each of these two sections is made of two arc cells with an utility straight section in between. The *Short* straight section is dispersion free and it is used for RF, feedback and diagnostics. The *Long* straight section is used for injection and diagnostics.

1.3.1 The Arc Cell

Particular care has been taken in the design to make the damping times as short as possible in order to counteract possible instabilities at such low energy. Low bending radius in the dipoles and four high field wigglers in each ring produce large energy loss. The wigglers double the energy radiated in the bending magnets.

One of the parameters required to increase the luminosity is high emittance. The arc cell (BWB) with two bendings and a wiggler in between has been designed to increase the emitted radiation and tune the emittance. The cell is a double bend achromat with three quadrupoles (DFF) and a wiggler inside; a chromaticity correcting sextupole is placed on each side of the wiggler. One of the dipoles has parallel

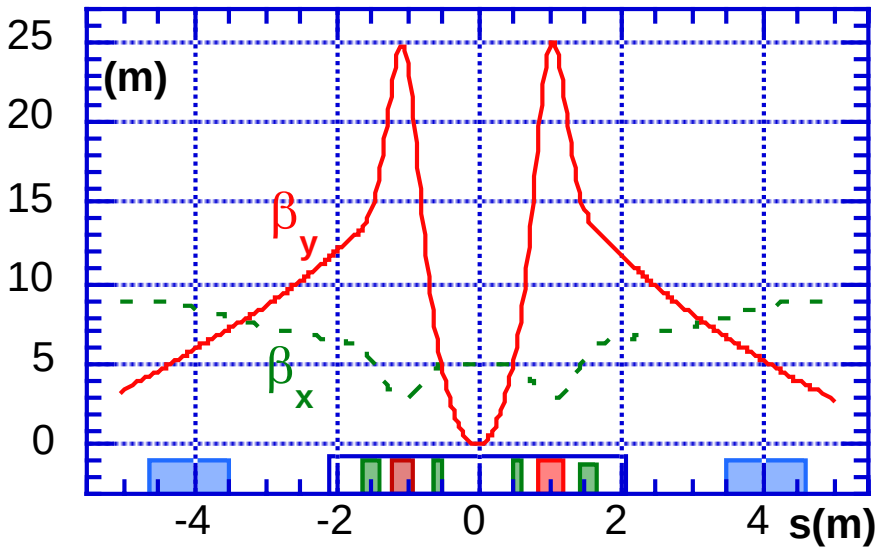

Figure 1.4: Optical functions in IR1

end faces allowing a better separation of the optical functions at the sextupoles. By varying the dispersion function in the wiggler the emittance can be tuned over a large range.

1.3.2 The Interaction Regions

A peculiar feature of the lattice is the interaction region where the two beams travel together in a common vacuum chamber. Due to the crossing angle in the horizontal plane the beams pass through the low-β quadrupoles off axis. A correction scheme with the splitter magnets and corrector dipoles allows to change the crossing angle so that the effect of parasitic crossings can be finely tuned. The beams are separated at the IR ends by about 12 cm. To increase the separation and to lower the chromaticity, mainly due to the low-β insertions, a focusing sequence FDF has been chosen. The optical functions inside the IR are symmetric with respect to the IP.

Four different IR lattices have been designed: three for the experiments and one for commissioning without the detectors. The total IR first order transport matrix is almost the same for all configurations, thus allowing to interchange the four IRs with small adjustments of the optical functions in the arc.

The *DAY-ONE IR* has been used for machine commissioning before KLOE installation. It housed seven electromagnetic quadrupoles to help tuning the optical

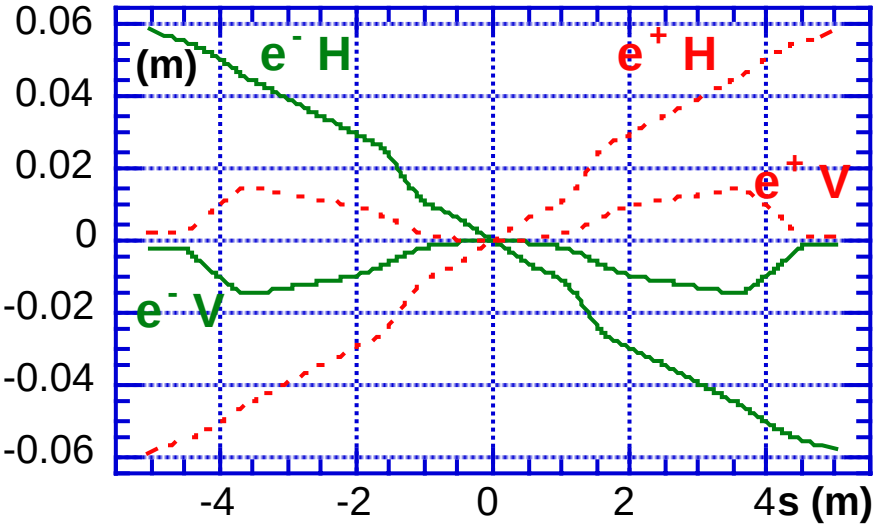

Figure 1.5: Beam trajectories in IR1

functions, with a quadrupole placed at the IP to reduce the chromaticity. A Beam Position Monitor (BPM) at the IPs allowed to align the two beams for collision.

At the beginning of 1999 the KLOE IR, which is described in detail in next Section 1.4 has been installed in IR1, while DEAR has been placed in IR2, which has been obtained by removing the central quadrupole at the IP.

1.4 The KLOE IR

KLOE is a large detector equipped with a longitudinal field solenoid. In order to leave the maximum free solid angle for the experiment the low-β triplets, which are embedded inside the detector, are realized with permanent magnet quadrupoles.

The three quadrupoles are confined inside a cone of 9° half-aperture; the free space around the IP is ± 0.45 m and the solid angle available for the detector is 99%. The optical functions and beam trajectories in the KLOE IR are shown in Figure 1.4 and 1.5. The KLOE detector consists of a cylindrical drift chamber surrounded by a lead-scintillating fiber electromagnetic calorimeter and immersed in the 0.6 T magnetic field of a 2.5 m radius superconducting solenoid. The integrated field of the KLOE solenoid is as high as BL=2.4 Tm: this is then a strong perturbation to the machine optics at the DAΦNE energy which corresponds to a rigidity of $B\rho = 1.7$ Tm. The KLOE solenoid rotates the normal modes of oscillation in the

transverse plane by an angle of $\theta_R = 45°$ where the angle θ_R is defined by

$$\theta_R = \frac{1}{2B\rho} \int B_z(s) ds \tag{1.6}$$

This is the major contribution to the coupling between radial and vertical oscillations, usually expressed by the factor $\kappa = \varepsilon_y / \varepsilon_x$ that is the ratio between the vertical and the radial emittance. This effect must of course be compensated in order to have the very flat beam required for high luminosity, that is in order to have a coupling as small as $\kappa \leq 0.01$.

To cancel the coupling at the IP and at the ends of the IR a matrix of each half-IR block diagonal using four skew quadrupoles would be sufficient. This method cannot be applied to DAΦNE for the lack of space. To correct such a large coupling the so called Rotating Frame Method (RFM) has been adopted [7] which exploits compensating solenoids plus rotated quadrupoles; the rotation introduced by the solenoidal field of KLOE is neutralized by two superconducting compensating solenoids of equal but opposite integrated field and symmetrically placed on each side of the detector.

The RFM allows to insert the low-β quadrupole triplets between the main and the compensating solenoids without affecting the coupling correction. This is based on a property of the solenoid matrix that can be written as the product of two matrices $\mathrm{R}(\theta_\mathrm{R})$ and F, which commute. $\mathrm{R}(\theta_\mathrm{R})$ is a rotation and F is a block diagonal matrix equivalent to a quadrupole focusing in both planes with strength $\mathrm{K} = (\theta_\mathrm{R}/\mathrm{L})^2$.

The half IR matrix consisting of half detector solenoid plus one compensator can be written as:

$$\mathrm{M_H} = \mathrm{F_C}\ \mathrm{R}(-\theta_\mathrm{R})\ \mathrm{R}(\theta_\mathrm{R})\ \mathrm{F_D} \tag{1.7}$$

where F_C is the matrix representing half compensator and F_D represents half detector. A quadrupole inserted between the detector and the compensator does not introduce coupling, provided that it is tilted by θ_R, that is by the same angle of the solenoid rotation angle.

In fact, when a quadrupole represented by the matrix Q is tilted by the angle θ_R its matrix becomes:

$$\mathrm{Q_R} = \mathrm{R}(\theta_\mathrm{R})\ \mathrm{Q}\ \mathrm{R}(-\theta_\mathrm{R}). \tag{1.8}$$

Inserting Q_R in the matrix M_H just between the detector and the compensating solenoid in the Equation 1.7 the rotations cancel out and M_H becomes $M_H = F_C Q F_D$, that is it becomes block diagonal being the product of block diagonal matrices.

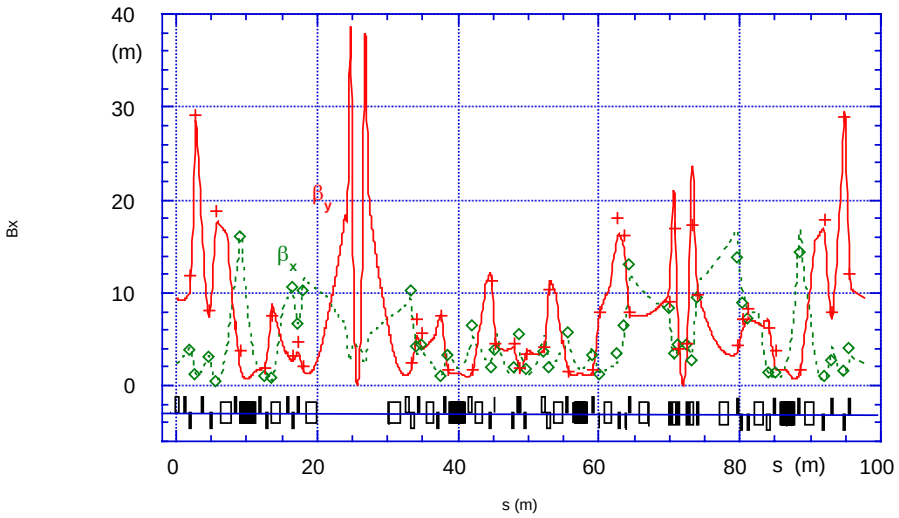

Figure 1.6: Horizontal and vertical β-functions in the positron ring.

In the KLOE IR the low-β quadrupoles are immersed in the detector solenoid. An exact application of the RFM would require that each quadrupole is continuously rotated like an helix. In practice the quadrupoles are rotated by the angle corresponding to their longitudinal midpoint. The resulting half IR matrix has a small residual coupling which is corrected by slightly adjusting four parameters: three additional rotations of the low-β quadrupoles and a correction of the compensating field.

1.5 Optics Measurements

As I have mentioned in Section 1.2, in order to have a large lattice flexibility all magnetic elements have independent power supplies. This allows to measure the β-functions at all quadrupoles. The β-functions measured along the ring are shown in Figure 1.6 where they are compared with the lattice model.

Due to the high beam emittance the machine aperture is large: both for this reason and because of the short length of the magnetic elements the effect of the fringing fields is not negligible and corrections have been applied to the dipoles, which account for a change of almost 0.5 in the vertical tune. The model also takes into account the focusing effects in the wigglers. In the KLOE IR short slices of solenoid interleaved by thin lens quadrupoles account for the overlap and for the longitudinal variation of the fields. In addition, in order to better fit the measured β-function some free parameters have been used as variables.

An independent check of the model can be obtained by using the information of the response matrix which is measured by recording the closed orbit displacements produced by unit variations of the dipole correctors. A procedure to derive the optical functions from the response matrix reducing the influence of calibration errors and correctors is in progress. This check of the model is especially important for the KLOE IR where a direct measurement of the optical functions cannot be performed by varying the quadrupole currents as they consist of permanent magnets.

The closed orbit before correction was inside the ring aperture in both rings. Since the two rings are very close to each other the stray fields from high field elements produce orbit changes on the nearby ring. The horizontal closed orbit is determined not only by magnetic misalignments but also by the compensation of the trajectory in the wigglers and by the splitter setting as a function of the crossing angle at the IP. Four methods to correct the closed orbit have been implemented:

- best corrector
- harmonic correction
- eigenvalues of measured response matrix
- bumps in the IRs

Orbit bumps in the IRs, with four or six correctors have been used to precisely adjust angle and displacement in the horizontal and vertical plane at the IP. The orbit measurement in the IRs is performed separately for each beam in the same monitors. Bumps are also used to vertically separate the beams in one IR when colliding the beams only in the other one.

During commissioning with the *DAY-ONE IR* a coupling of the order of $\kappa \approx 0.002$ has been obtained after closed orbit correction and with the sextupoles turned on, that is a much smaller value the the design one $\kappa = 0.01$. Coupling has been estimated from the synchrotron light monitor and by the closest tune approach distance. Another sensitive measurement of the relative variation of the coupling is the beam lifetime which is essentially determined by the Touschek effect and therefore it is inversely proportional to the beam density and, for small coupling, nearly proportional to the square root of the coupling. The minimum coupling has been found by measuring the beam lifetime as a function of the strength of a skew quadrupole.

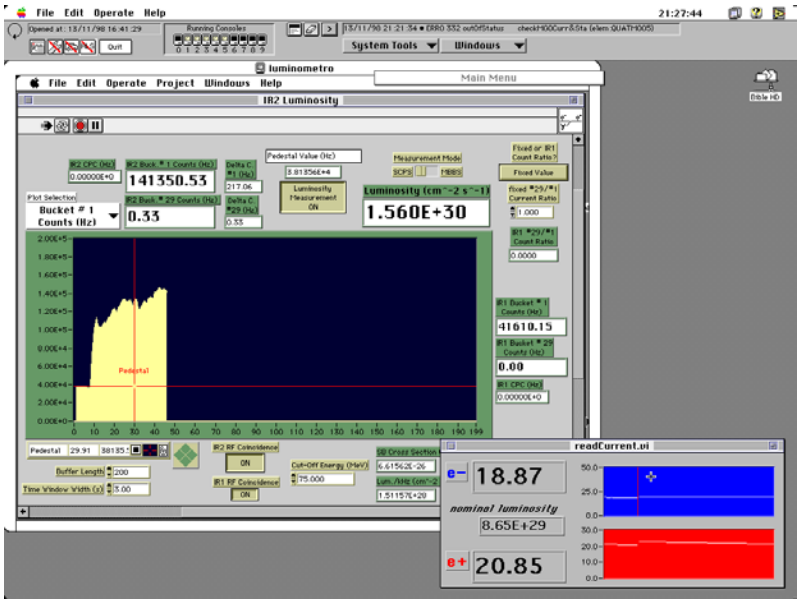

Figure 1.7: Single Bunch luminosity measured by the DAΦNE luminosity monitor.

The horizontal emittance measured by the synchrotron light monitor is in agreement with the value calculated by the model.

The chromaticity has been measured and corrected using the same sextupole strengths in both rings. The sextupole strengths have been tuned in order to improve the energy acceptance of the ring and therefore the beam lifetime. Indeed the lifetime depends on the physical and dynamic aperture for the betatron and synchrotron oscillations where the physical aperture corresponds to the physical dimensions of the vacuum chamber and the dynamic aperture is the innermost radius of the region in the phase space where the single particle motion is stable. The design value of the energy acceptance has been reached by powering only the eight sextupoles located in the arcs arranged in four families.

1.6 The DAΦNE Single Bremsstrahlung Luminosity Monitor

In this section the luminosity measurement technique [6] and the main set-up adopted in DAΦNE will be described. The more direct way to measure the luminosity consists in measuring the counting rate of a known cross-section electromagnetic process generated at the collision point. At DAΦNE it has been chosen to use the photon

production in the single Bremsstrahlung (SB) to measure the luminosity. The SB process is described by:

$$e^+ + e^- \rightarrow e^+ + e^- + \gamma \tag{1.9}$$

The photons are emitted in the direction of the beam particles within a cone of the order of $\sim 2/\gamma$ where γ is the beam's particle energy in rest mass units and for DAΦNE is $\simeq 10^3$. The maximum possible energy of the photons is the single beam energy. The single Bremsstrahlung has been selected because of its high counting rate, that permits on-line luminosity measurements. The counting rate $\dot{N}_{SB}$ is the number measured by the proportional counter, the luminosity is derived from $\dot{N}_{SB}$ from:

$$\mathcal{L} = \frac{\dot{N}_{SB}}{\sigma_{SB}(k_{min}\Omega_{det})} \tag{1.10}$$

where σ_{SB} is the cross section for the chosen SB process, Ω_{det} is the solid angle defined by the the detector and k_{min} is the minimum photon energy detected by the monitor. To find the value for this last quantity k_{min} a calibration with gas-Bremsstrahlung (GB) and only one beam in the machine is necessary.

Proportional Counter

The structure of the detector is a sample of the KLOE electromagnetic calorimeter. It consists in a proportional counter made of alternated layers of lead and scintillating fibers with photomultiplier read-out. The charge signal from the photomultiplier is proportional to the photon energy. Energy analysis and photon counting are provided by the data acquisition system.

Background subtractions

The main background affecting the measurement comes from photons produced by Bremsstrahlung on the residual gas. Two background subtraction methods can be used: the single counting channel pedestal subtraction (SCPS) and the missing bunch background subtraction (MSSB).

In the former (SCPS) method the contribution of photons produced by Bremsstrahlung on the residual gas is subtracted by measuring this gas Bremsstrahlung rate when beams are longitudinally separated. In DAΦNE it is used what has been called the *RF Phase Jump* [34] technique where the electron beam is injected 360 or 720 RF degrees far from collision and then brought in collision with a fast phase variation to zero degrees in ≈ 800 ns. Then the rate is measured with the beams in collision, and

the difference between the two is the SB counting rate that, when divided by the SB integrated cross section, gives the luminosity value. Using the SBBS scheme it is necessary to periodically separate the beams for updating the background value. The second method (MSSB) consists in injecting two positron bunches: a colliding one and a smaller one, in an out of collision bucket. Assuming that the residual gas pressure is the same for the two bunches and assuming that the background is due to the GB contribution only, it is possible to derive an expression relating the counting rates and the currents.

This method can be generalized to a multibunch operation if the collider is filled in such a way that all the bunches but one (or a few) are in collision. Both the background subtraction schemes assume that thickness and position of the GB source do not change between the in and out collision situations. In fact, any phenomenon that modifies the position or the angle at IP of the beam facing the counter will generate a modification in the GB target with a consequent variation in the background counting rate.

In Figure 1.7 is reported the luminosity read-out window during a single bunch luminosity measurement in the *DAY-ONE* commissioning phase. The picture shows the counting rate as a function of time. The dip in the counting rate corresponds to the beam separation obtained with the RF phase change. In the bottom right of the figure are the two beams currents, red for positrons and blue for electrons.

Chapter 2

The Beam-Beam Interaction

In this chapter I present a description of what is the beam-beam effect in e^+e^- storage rings, its main features and related problems.

2.1 Introduction

When the beams cross each other in the intersection region of a storage ring two distinct effects occur, either a particle of one beam sees the other beam as a collection of point charges or it can interact with a single particle of the opposite oncoming beam. It is these particle interactions which the experimental physicist studies. The average number of such events depends both on the cross section σ that characterizes the considered physical process and on beam's luminosity $\mathcal{L}$. When an electron of, say, beam 1 passes through a bunch of beam 2 the probability of an event is:

$$\frac{N_2\sigma}{A} \tag{2.1}$$

where A is the transverse area of the bunch, and $N_2\sigma$ is the target area occupied by the N_2 particles of beam 2[1].
The expected number of events of each crossing is consequently:

$$\Delta N_{ev} = N_1 \cdot \frac{N_2\sigma}{A} \tag{2.2}$$

[1] In the classical approximation σ is the electron's transverse area πr_e^2; the probability of an event is just given by the ratio between the area covered by the electrons ($N_2\pi r_e^2$) and the total area A.

and for the rate of events:

$$\dot{N}_{ev} = f N_1 \cdot \frac{N_2 \sigma}{A} \tag{2.3}$$

where N_1 is the number of particles in the bunch of beam 1 and f is the bunches revolution frequency. The machine physicists call luminosity $\mathcal{L}$ the parameter that multiplied by the cross section σ gives $\dot{N_{ev}}$ (see Equation 2.3) so that it is:

$$\mathcal{L} = \frac{f N_1 N_2}{A} \tag{2.4}$$

For a Gaussian beam distribution the equivalent transverse area is:

$$A = 4\pi\sigma_x\sigma_y$$

where σ_x and σ_y are the rms vertical and horizontal beam sizes at the collision point. A general expression for the luminosity has been derived in Appendix B. The luminosity is the main parameter that connects the machines with particle experiments. The events given by Equation 2.3 are very rare being $N_2 r_e^2 \ll \sigma_x\ \sigma_y$ (typical values are: $N_2 \approx 10^{11},\ \sigma_x \approx 10^{-3}$ m, $\sigma_y \approx 10^{-5}$ m).

A particle of one beam will be influenced by the electromagnetic field of the other beam at each crossing. This is called the *beam-beam interaction*. From Equation 2.4 it may seem that it is possible to enhance the luminosity as much as wanted, just increasing the number of the beam particles. Actually, this is not true. Experimentally it has been found a limit for the luminosity beyond which the beams are unstable.

This limit is translated into a limit on the betatron frequency shift (so called linear tune shift) that one beam produces on the other one. As it will be discussed in Section 2.3 only particles with very small betatron oscillations amplitudes experience a linear tune shift. For betatron oscillations larger than one σ the field becomes very nonlinear turning over to the well known $1/r$-law at large distances from the beam center. It is for this reason that a definite quantitative description of the actual beam-beam effect has not been possible yet.

The luminosity value is mainly related to the shape of the beam core determined by the beam-beam interaction. Nevertheless, the beam-beam interaction does not limit only the luminosity but it can also be dangerous for the beam lifetime. In fact the beam-beam interaction increases the population of the tails of the distribution; the lifetime becomes unacceptable when the beam is spread out in such a way that it is rapidly lost.

There are two treatments generally used to describe the beam-beam interactions:

- *weak-strong* model: interaction of a single particle at the collision point with a strong rigid Gaussian bunch;

- *strong-strong* model: two opposite bunches interacting at each turn in the collision point; to simplify the model it can be assumed that they are both Gaussian.

In both these models all effects which are consequences of the interaction between individual particles (i.e. Coulomb interaction of two individual particles) are excluded. In the weak-strong model the strong beam plays the role of an external perturbation for the weak beam dynamics. In the next section the beam-beam interaction is described in detail, starting from the weak-strong model.

2.2 Beam-Beam Forces

The distribution of each beam without interaction can be expressed by a charge density distribution $\rho(x, y, z)$ given by a three-dimensional Gaussian The beam-beam interaction changes both the parameters and the shape of the transverse density distribution.

As discussed in Section 2.1, the weak-strong model studies a single particle interacting with the electromagnetic field generated by the opposite Gaussian bunch, assuming that this is fixed at the interaction point and rigid, that is not perturbed by the opposite beam. In the strong-strong interaction instead, it is taken into account that both interacting bunches change the Gaussian distribution.
Two observations can be pointed out:

1. The weak-strong model is not accurate when it is applied to a strong-strong real case;

2. The strong-strong treatment is very difficult -I could say impossible if some simplifying assumptions are not made.

These two approaches can be compared with two other classical problems:

- weak-strong case $\rightarrow$ two bodies problem;

- strong-strong case $\rightarrow$ three -or more- bodies problem.

It is easy to imagine that the strong-strong treatment is complicated and difficult to understand. Much can be understood by considering the weak-strong interaction, at the limit of a single particle against a strong beam. The net kick given to a particle displaced by distances x and y can be expressed as integrals of the electro-magnetic forces over the particle's trajectory through the opposite bunch. The forces can be calculated using Gauss and Ampere laws for a Gaussian charge density distribution. I want to describe here the expression of this integrated transverse angular deflection received by a particle crossing a charged beam, with a Gaussian density distribution.

As a first approximation the variations of σ_x and σ_y with z at the crossing point are assumed to be very weak, that is the beam-beam interaction is assumed to be an impulsive force.

The electromagnetic tensor of a single electron traveling at velocity $\beta = v/c$ can be obtained by a Lorentz transformation of the electrostatic field of an electron at rest. In this transformation magnetic components are generated and the transverse electric field orthogonal to its direction is amplified by the Lorentz factor $\gamma = (1 - v^2/c^2)^{-1/2}$ and the total longitudinal magnetic action of the oncoming particle will be negligible.
Explicitly a particle moving along the longitudinal coordinate z with velocity $\vec{v} = \beta c\hat{z}$ ($\hat{z}$ is the versor along z) crosses the electromagnetic fields of the opposing beam with components

$$\vec{E} = (E_x, E_y, E_z) \qquad \vec{B} = (B_x, B_y, B_z)$$

in the laboratory frame. The electric and magnetic fields corresponding to a Gaussian charge distribution of the strong counter-rotating bunch is obtained starting from the electrostatic field $\vec{E}'$ of the strong bunch at rest:

$$\begin{cases} E_x = \gamma E'_x \\ E_y = \gamma E'_y \\ E_z = E'_z \end{cases} \qquad \begin{cases} B_x = \frac{\gamma\beta}{c} E'_y = \frac{\beta}{c} E_y \\ B_y = \frac{\gamma\beta}{c} E'_x = \frac{\beta}{c} E_x \\ B_z = 0 \end{cases}$$

The transverse components of the force are calculated using the Lorentz equation

$$\begin{cases} F_x = e(E_x + \beta c B_y) = e(1+\beta^2)E_x \approx 2eE_x \\ F_y = e(E_y + \beta c B_x) = e(1+\beta^2)E_y \approx 2eE_y \end{cases}$$

and being $\beta \simeq 1$ they become

$$\begin{cases} F_x = 2eE_x \\ F_y = 2eE_y \end{cases}$$

and the two transverse kicks are calculated integrating the corresponding component of the Lorentz force over time:

$$\Delta x' = \frac{\Delta p_x}{p_{tot}} = -\frac{e}{m_0 \gamma c}\int_{-\infty}^{\infty}(E_x + \beta c B_y)dt = -\frac{e}{m_0 \gamma c}\int_{-\infty}^{\infty} 2E_x dt \tag{2.5}$$

$$\Delta y' = \frac{\Delta p_y}{p_{tot}} = -\frac{e}{m_0 \gamma c}\int_{-\infty}^{\infty}(E_y + \beta c B_x)dt = -\frac{e}{m_0 \gamma c}\int_{-\infty}^{\infty} 2E_y dt \tag{2.6}$$

where m_0 is the electron rest mass, c is the light velocity, p_x and p_y are the two transverse components of the total particle momentum p_{tot}.

E_x and E_y are the derivates of the electric potential V_{BB}:

$$E_x = -\frac{\partial V_{BB}}{\partial x} \qquad E_y = -\frac{\partial V_{BB}}{\partial y} \tag{2.7}$$

where V_{BB} is given by the solution of the Poisson's equation

$$\bigtriangledown^2 V_{BB} = \frac{\rho}{\epsilon_0} \tag{2.8}$$

ρ gives the distribution charge of the opposite bunch:

$$\rho(x,y) = \frac{Ne}{2\pi\sigma_x\sigma_y} exp[-(\frac{x^2}{2\sigma_x^2} + \frac{y^2}{2\sigma_y^2})]. \tag{2.9}$$

It can be demonstrated that the potential that satisfies Poisson's equation (see Equation 2.8) with ρ given by Equation 2.9 can be written as [13]:

$$V_{BB}(x,y) = \frac{Ne}{4\pi\epsilon_0}\int_0^{\infty} \frac{exp[-(\frac{x^2}{2\sigma_x^2+q} + (\frac{y^2}{2\sigma_y^2+q})]}{\sqrt{(2\sigma_x^2+q)(2\sigma_y^2+q)}} dq \tag{2.10}$$

Assuming that $\sigma_x > \sigma_y$, setting

$$t^2 = \frac{2\sigma_y^2 + q}{2\sigma_x^2 + q}$$

and defining

$$r = \sigma_y/\sigma_x; \qquad a = \frac{x}{\sqrt{2(\sigma_x^2 - \sigma_y^2)}}; \qquad \text{and} \qquad \mathrm{b} = \frac{\mathrm{y}}{\sqrt{2(\sigma_\mathrm{x}^2 - \sigma_\mathrm{y}^2)}}$$

is obtained the famous formula derived by Bassetti and Erskine [14]:

$$E_x - iE_y = -i\frac{Ne}{2\epsilon_0\sqrt{2(\sigma_x^2 - \sigma_y^2)}}\Big[w(a+ib) - w(ar + i\frac{b}{r})e^{\left[-(a+ib)^2 + (ar + i\frac{b}{r})^2\right]}\Big] \propto -if_{bb} \tag{2.11}$$

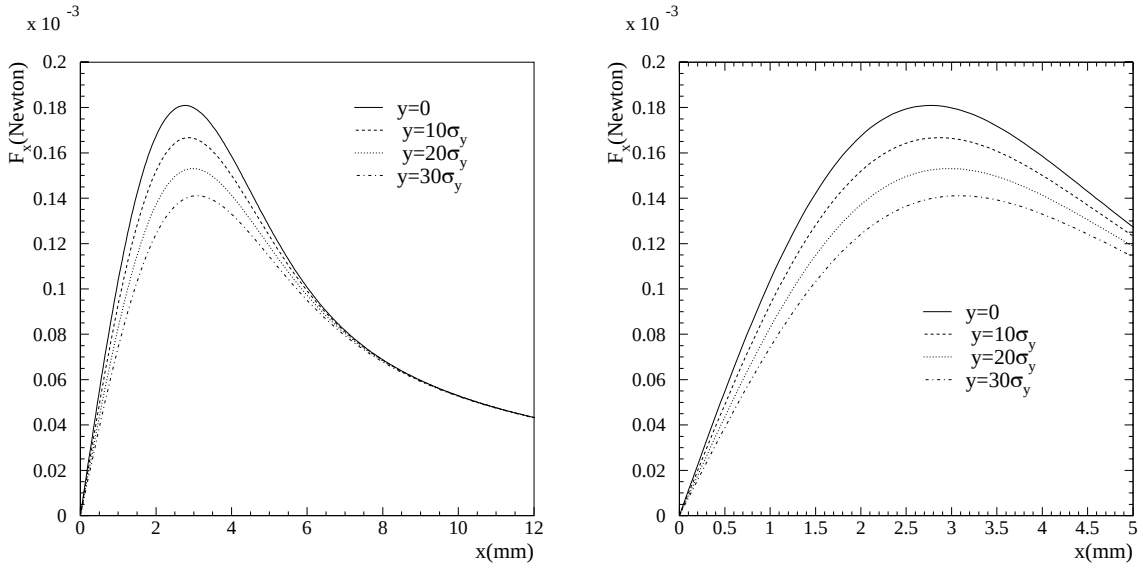

Figure 2.1: Beam-Beam integrated force seen by a horizontally displaced particle for a fixed vertical position (from Equation 2.14), with DAΦNE parameters, in particular: energy per beam $E = 0.51$ Gev and beam sizes $\sigma_x = 2.11$ mm and $\sigma_y = 21.1$ μm. F_x has been plotted in two different scales, in (a) is shown the behavior to zero for large displacements; in (b) it is evidenced the peak of the force at about 1.5 $\sigma_x \approx 3$ mm.

where N is the number of particles in a beam bunch, $w(z)$ is the complex error function defined as:

$$w(z) = e^{-z^2}\Big[1 + \frac{2i}{\sqrt{\pi}}\int_0^z e^{\zeta^2} d\zeta\Big]$$

and

$$\zeta = at + ib/t \quad , \quad (r \leq t \leq 1)$$

and I have called

$$f_{bb} = w(a + ib) - w(ar + i\frac{b}{r})e^{\left[-(a+ib)^2+(ar+i\frac{b}{r})^2\right]}$$

The two transverse fields from the previous expression 2.11 result

$$E_x = \frac{Ne}{\pi\epsilon_0\sqrt{2(\sigma_x^2 - \sigma_y^2)}}\mathcal{I}m f_{bb} \tag{2.12}$$

$$E_y = \frac{Ne}{\pi\epsilon_0\sqrt{2(\sigma_x^2 - \sigma_y^2)}}\mathcal{R}e f_{bb} \tag{2.13}$$

Formula 2.11 is generally used for beam-beam simulations, as it will be discussed in Chapter 3.

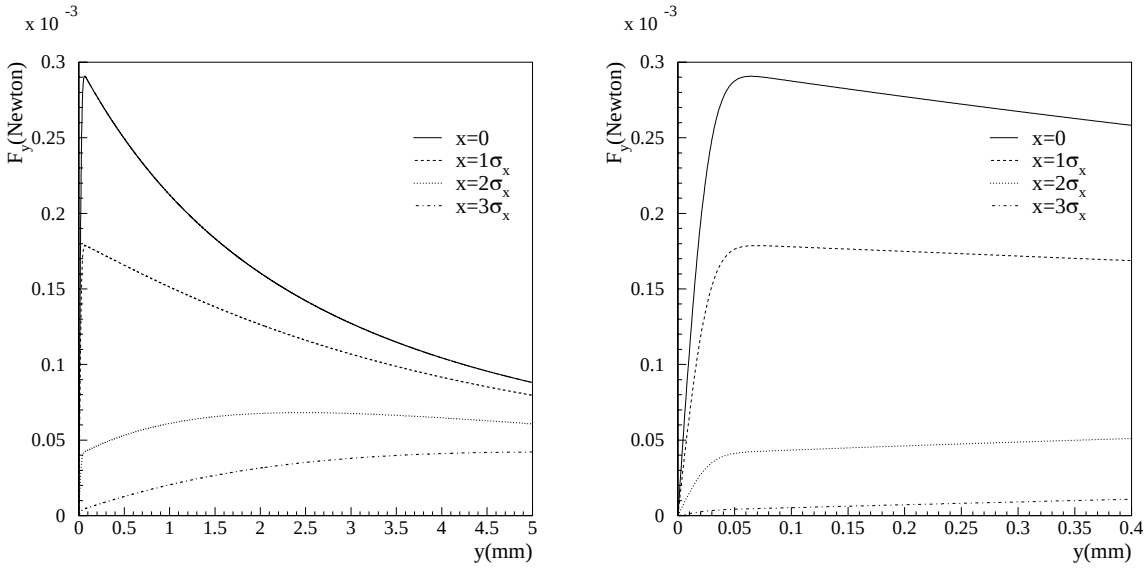

Figure 2.2: Beam-Beam integrated force seen by a vertically displaced particle for a fixed horizontal position (from Equation 2.15) with DAΦNE parameters, in particular: energy per beam $E = 0.51$ Gev and beam sizes $\sigma_x = 2.11$ mm and $\sigma_y = 21.1$ μm. F_y has been plotted in two different scales, in (a) is shown the slow behavior to zero for large displacements; in (b) it is evidenced the peak of the force at about 1.5 $\sigma_y \approx 0.3$ mm.

The two components of Equations 2.12 and 2.13 can be written as

$$E_x = \frac{Ne}{\pi\epsilon_0\sqrt{2(\sigma_x^2-\sigma_y^2)}}\int_r^1 a exp[a^2(t^2-1)+b^2(1-\frac{1}{t^2})]dt \tag{2.14}$$

$$E_y = \frac{Ne}{\pi\epsilon_0\sqrt{2(\sigma_x^2-\sigma_y^2)}}\int_r^1 \frac{b}{t^2} exp[a^2(t^2-1)+b^2(1-\frac{1}{t^2})]dt. \tag{2.15}$$

Finally, using the previous expressions 2.14 and Equations 2.5 the beam-beam kicks can be written:

$$\Delta x' = -\frac{4Nr_e}{\gamma\sqrt{2(\sigma_x^2-\sigma_y^2)}}\int_r^1 a\ exp[a^2(t^2-1)+b^2(1-\frac{1}{t^2})]dt \tag{2.16}$$

$$\Delta y' = -\frac{4Nr_e}{\gamma\sqrt{2(\sigma_x^2-\sigma_y^2)}}\int_r^1 \frac{b}{t^2} exp[a^2(t^2-1)+b^2(1-\frac{1}{t^2})]dt. \tag{2.17}$$

The beam-beam forces have been represented graphically in Figures 2.1 and 2.2 for $x \geq 0$ and $y \geq 0$, with the DAΦNE beam parameters: $N = 9 \cdot 10^{10}$ particles per bunch, $\sigma_x = 2.11$ mm and $\sigma_y = 0.0211$ mm. It is clear from the two plots that the nature of these two beam-beam transverse kicks is highly nonlinear. Moreover, the force is almost linear for small displacements, it is zero at the bunch center, it

increases with the distance from this bunch center and peaks close to 1.5σ of the bunch.

In fact, as it appears in Figure 2.1, $\Delta x'$ has a maximum radial value at 3 mm just corresponding to $1.5\sigma_x$. Similarly, from Figure 2.2, the maximum vertical value of the integrated force $\Delta y'$ is at 0.03 mm corresponding to $1.5\sigma_y$. For large displacements the integrated force goes like $1/r$ with the distance. A typical particle in a storage ring experiences all parts of these two curves due to its betatron oscillations.

To conclude, it can be pointed out a difference in the vertical and radial force behavior: in the vertical plane when a particle is at many σ_y far from the bunch center is still influenced by the beam-beam force (Figure 2.2 (b)), while in the radial plane the beam-beam force goes much more rapidly to zero as the particle is off a few σ_x from the bunch center (Figure 2.1 (b). This is intuitive as the beam is flat, so for vertical distances of many σ_y the particle still "sees" the other bunch horizontally. On the other hand, as the particle passes off the oncoming bunch a few σ_x radially, the vertical field component will be negligible.

2.3 Linearization of the Bassetti-Erskine formulae

The beam-beam force experienced by a particle near the bunch center can be linearized. Let us start writing explicitly Equations 2.16 and 2.17 respectively in the two cases y=0 and x=0.
Let us consider the horizontal plane first. In Appendix A is shown that Equation 2.16 in y=0 becomes:

$$\Delta x' = -\frac{4Nr_e}{\gamma\sqrt{2(\sigma_x^2-\sigma_y^2)}}\Big[F_D\Big(\frac{x}{\sqrt{2(\sigma_x^2-\sigma_y^2)}}\Big) - e^{-\frac{x^2}{2\sigma_x^2}}\cdot F_D\Big(\frac{x}{\sqrt{2(\sigma_x^2-\sigma_y^2)}}\cdot\frac{\sigma_y}{\sigma_x}\Big)\Big] \quad (2.18)$$

where F_D is the Dawson function defined by:

$$F_D(x) = e^{-x^2}\int_0^x e^{t^2}dt$$

For small x a linear approximation can be made:

$$F_D(x) \approx x + \mathcal{O}(x^2)$$

so that:

$$\Delta x' = -\frac{4Nr_e}{2\gamma(\sigma_x^2-\sigma_y^2)}(1-\frac{\sigma_x}{\sigma_y})x = -\Big(\frac{2Nr_e}{\gamma\ \sigma_x(\ \sigma_x+\ \sigma_y)}\Big)\cdot x \quad (2.19)$$

For the vertical plane, in Appendix A is shown that Equation 2.17 in x=0 becomes:

$$\Delta y' = -\frac{4Nr_e e^{b^2}}{\gamma\sigma_x\sqrt{2(1-r^2)}}\frac{\sqrt{\pi}}{2}\Big[erf\Big(\frac{y}{\sigma_y\sqrt{2(1-r^2)}}\Big) - erf\Big(\frac{y}{\sigma_x\sqrt{2(1-r^2)}}\Big)\Big] \tag{2.20}$$

where erf(x) is the error function defined by:

$$erf(x) = \frac{2}{\sqrt{\pi}}\int_0^x e^{-t^2}dt$$

For small x the following linear approximation holds:

$$erf(x) \simeq \frac{2}{\sqrt{\pi}}x + \mathcal{O}(x^2)$$

and inserting this approximation inside the Equation 2.20 one gets:

$$\Delta y' = -\Big(\frac{2Nr_e}{\gamma\sigma_y(\sigma_x+\sigma_y)}\Big)\cdot y \tag{2.21}$$

It appears from the two relations 2.19 and 2.21 that in the linear approximation the beam-beam interaction can be described by the transfer matrix:

$$\begin{pmatrix} 1 & 0 & 0 & 0 \\ -\frac{1}{f_x} & 1 & 0 & 0 \\ 0 & 0 & 1 & 0 \\ 0 & 0 & -\frac{1}{f_y} & 1 \end{pmatrix} \tag{2.22}$$

where the focal lengths f_x and f_y are defined by:

$$\frac{1}{f_y} = K_y = \frac{2r_eN}{\gamma\sigma_y(\sigma_x+\sigma_y)} \tag{2.23}$$

$$\frac{1}{f_x} = K_x = \frac{2r_eN}{\gamma\sigma_x(\sigma_x+\sigma_y)} \tag{2.24}$$

It is common to define two parameters

$$\xi_x = \frac{r_e}{2\pi}\frac{N\beta_x^*}{\gamma\sigma_x(\sigma_y+\sigma_x)} = \beta_x^*K_x/4\pi \tag{2.25}$$

$$\xi_y = \frac{r_e}{2\pi}\frac{N\beta_y^*}{\gamma\sigma_y(\sigma_y+\sigma_x)} = \beta_y^*K_y/4\pi \tag{2.26}$$

where β_x^* and β_y^* are the unperturbed values of the horizontal and vertical β-functions at the interaction point. The changes in the tune due to the beam-beam interaction are conventionally called the *linear tune shifts* ξ_y and ξ_x.

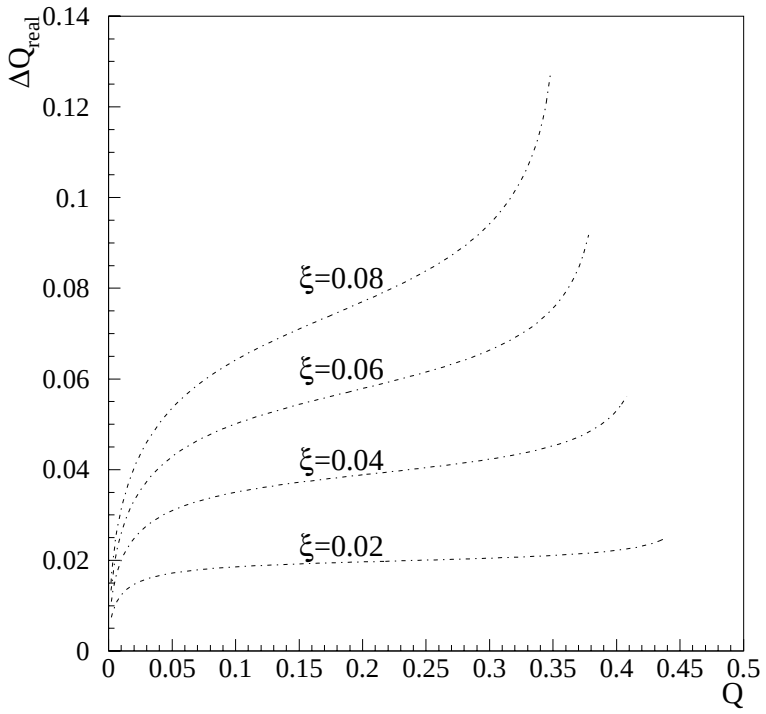

Figure 2.3: Beam-Beam Tune shift (ΔQ_{real}) dependence on ξ and Q as described by the Equation 2.31.

2.4 Linear Tune Shift Parameter and Effective Tune Shift

Let's consider the vertical plane. For symmetry reasons the beam-beam kick will be split into two halves, and the transfer matrix from one interaction point to the next one is given by:

$$\begin{pmatrix} 1 & 0 \\ -\frac{K}{2} & 1 \end{pmatrix} \begin{pmatrix} \cos 2\pi Q & \beta^* \sin 2\pi Q \\ -\frac{1}{\beta^*} \sin 2\pi Q & \cos 2\pi Q \end{pmatrix} \begin{pmatrix} 1 & 0 \\ -\frac{K}{2} & 1 \end{pmatrix} \tag{2.27}$$

which must coincide with the one-turn matrix:

$$\begin{pmatrix} \cos 2\pi(Q + \Delta Q_{real}) & \beta^{NEW} \sin 2\pi(Q + \Delta Q_{real}) \\ -\frac{1}{\beta^{NEW}} \sin 2\pi(Q + \Delta Q_{real}) & \cos 2\pi(Q + \Delta Q_{real}) \end{pmatrix} \tag{2.28}$$

where $2\pi\Delta Q_{real}$ is the phase shift caused by the beam-beam perturbation, ΔQ_{real} is the effective beam-beam tune shift felt by the beam. β^{NEW} is the perturbed

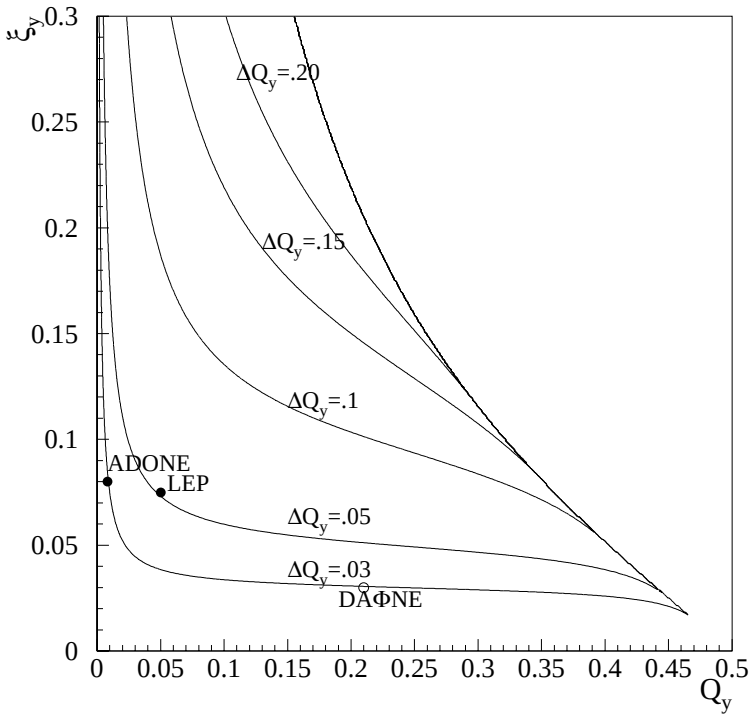

Figure 2.4: Contours of constant real tune shift ΔQ_{yreal} in the plane of the two scaling variables (Q_y, ξ_y). The measured values for ADONE and LEP are shown, for DAΦNE it is not a measured value.

β-function at the IP. The product matrices in 2.27 is:

$$\begin{pmatrix} \cos 2\pi Q - \frac{K}{2}\beta^* \sin 2\pi Q & \beta^* \sin 2\pi Q \\ -K\cos 2\pi Q - (\frac{1}{\beta^*} - \frac{\beta^* K}{4}\sin 2\pi Q) & \cos 2\pi Q - \frac{K}{2}\beta^* \sin 2\pi Q \end{pmatrix}. \tag{2.29}$$

The trace of matrix 2.29 must be equal to that of matrix 2.28; it follows, using also Equations 2.25 and 2.26 that

$$\cos(2\pi Q + 2\pi\Delta Q_{real}) = \cos 2\pi Q - 2\pi\xi \sin 2\pi Q. \tag{2.30}$$

I would like to stress here the difference between the real beam-beam tune shift experienced by the interacting beams ΔQ_{real} and its linear approximation ξ. Equation 2.30 that has been rewritten here for completeness:

$$\Delta Q_{real} = \frac{1}{2\pi}[\arccos(\cos 2\pi Q - 2\pi\xi \sin 2\pi Q) - 2\pi Q] \tag{2.31}$$

has been plotted for constant values of ξ in Figure 2.3 and for constant values of ΔQ_{real} in Figure 2.4.

ΔQ_{real} in the linear approximation (ΔQ_{real}^{lin}), that is in case of betatron tune Q not too close to zero or to 1/2, coincides with ξ. In fact, it is always true that:

$$\cos 2\pi(Q + \Delta Q_{real}) = \cos 2\pi Q \cos \Delta Q_{real} - \sin 2\pi \Delta Q_{real} \sin 2\pi Q. \tag{2.32}$$

For such tunes not too close to zero or to 1/2 Equation 2.32 can be approximated by the following one:

$$\cos 2\pi(Q + \Delta Q_{real}^{lin}) \approx \cos 2\pi Q - \Delta Q_{real}^{lin} \sin 2\pi Q \tag{2.33}$$

From Equations 2.30 and 2.33 it is found the relation:

$$\Delta Q_{real}^{lin} = \xi. \tag{2.34}$$

The linear-lens model is a good approximation for small amplitude particles. It results that the single particle motion is completely described by two parameters: the betatron tune Q and the strength parameter ξ.

As it can be observed from Figure 2.4, as the betatron tune advance Q between two interaction points satisfies the relation $Q < \xi$, the linear tune shift ξ gets much higher, and with ξ also the luminosity. In this case of betatron tune very near to zero the real tune shift ΔQ_{real} will be much different from the linear tune shift ξ and the linear approximation of Equation 2.34 is not valid anymore.

Two representative examples have been reported in the figure 2.4: ADONE and LEP. Let us discuss them more explicitly.

- ADONE [16] worked on the vertical tune $Q_y = .05$ with six interaction points per turn. This means in one period the tune advance was $Q_y = 0.00833$ and $\xi = 0.08$. From these two values the real tune shift is found to be $\Delta Q_{real} = 0.0292$ and Equation 2.34 is strongly violated, and:
$$\frac{\xi}{\Delta Q_{real}} = 2.74$$
- LEP [17] is now working with a tune advance between two interaction points of $Q_y = .05$ with a $\xi = 0.075$. In this case $\Delta Q_{real} = 0.0509$, so that
$$\frac{\xi}{\Delta Q_{real}} = 1.5$$
- DAΦNE is working with a vertical tune of $Q_y = .21$. It could be argued that with a linear tune shift $\xi = 0.03$ the linear approximation is very good, that is $\Delta Q_{real} = \xi = 0.03$:
$$\frac{\xi}{\Delta Q_{real}} = 1$$

For the same value of ΔQ_{real} very different values of ξ can be obtained, depending on the choice of the working point . This is one of the reasons why ADONE and LEP could get high luminosities. From Figure 2.4 it appears that the tune advance between two IP must be near to the integer in order to work with high ξ . I just would like to point out that in ADONE and LEP the low value of tune per crossing is due to the fact that there are six and four IP respectively.

Consequently, from Figure 2.4 it appears that ξ gets higher as the number of interaction points increases, as if one could get a higher luminosity increasing the number of interaction points (IP). Of course, this is true if the optics allows to tune the machine near the integer tunes and the working point does not fall within an integer resonance stop-band. In addition, at the increase of the interaction points depending on the phase advance between them new resonances may be generated or destroyed [19] (see for example Figure 4.12). In conclusion it is hard to say a priori what behavior is expected increasing the number of IPs at the same working point.

2.5 Hamiltonian Treatment of the Beam-Beam Interaction

The nonlinear variation of the beam-beam force with r causes a tune shift dependent on the particle betatron oscillations amplitude and a tune spread in the beams and it drives nonlinear resonances. The usual method for treating these effects is the Hamiltonian perturbation theory. In order to compute the excitation of nonlinear resonances and tune shift driven by the beam-beam collisions, the nonlinear effects of the new Hamiltonian [22] are studied perturbatively:

$$H(x, p_x, y, p_y, s) = H_0 + V_{BB}(x, y, s) \tag{2.35}$$

where H_0 is the unperturbed Hamiltonian described in the next Section 2.6 and V_{BB} is the beam-beam potential considered as a small perturbation given in Section 2.8.

As discussed in Section 2.2 the beam-beam potential is highly nonlinear and it is not possible to find constants of the motion. So a perturbation method must be used in order to analyze the induced resonances and the amplitude dependent phase advance, that is the beam-beam tune spread. In the following it has been enumerated what must be done in order to perform this beam-beam resonances analysis:

1. H has to be written in terms of the action-angle variables of the unperturbed H_0;

2. a Fourier transformation of H has to be performed;

3. the dependencies of tunes on action from the average value of the perturbation have to be calculated;

4. the resonance conditions and resonance properties have to be determined from the slowly varying terms of H.

2.6 The unperturbed Hamiltonian

The Hamiltonian for the transverse motion of a single particle with no beam-beam interaction is [20]:

$$H_0(x, p_x, y, p_y, s) = -eA_s(s) - (1 + \frac{x}{\rho(s)})(p^2 + p_x^2 + p_y^2)^{1/2}. \qquad (2.36)$$

In this equation s is the usual coordinate along the reference orbit, ρ is the bending radius, A_s is the s-component of the vector potential describing the magnet lattice, $p = (E^2/c^2 - m^2c^2)^{1/2}$ is the total momentum, and p_x and p_y are the momenta conjugate to x and y. The ideal solution is to find constants of the motion. With a linear lattice, that is in presence of dipoles and quadrupoles, a generating function is used to canonically transform the Hamiltonian using action-angle coordinates

$$(x, p_x) \rightarrow (\psi_x, J_x) \qquad \text{and} \qquad (\mathrm{y}, \mathrm{p_y}) \rightarrow (\psi_\mathrm{y}, \mathrm{J_y}).$$

Let us consider the simple case of a one-dimensional system (y=0) in which the beam-beam potential is equal to zero. Hamilton's equation $\partial H/\partial p_x = x'$ yields the relation $p_x = x'$ and confirms the conjugate coordinate of the position x as x'. A generating function is used to canonically transform the Hamiltonian into a new Hamiltonian using action-angle coordinates $(\vec{J}, \vec{\phi})$. The new Hamiltonian has the advantage of being independent of the longitudinal coordinate s if one introduces a periodic coordinate $\tilde{\psi_x}$, which is related to the phase advance of the particle's motion

$$\psi_x(s) = \psi_x(0) + \int_0^s \frac{ds'}{\beta(s')}$$

by the following expression

$$\tilde{\psi_x} = \psi_x - \mathrm{Q_x}\theta = \psi_\mathrm{x} - \frac{\mathrm{Q_x s}}{\mathrm{R}}$$

The generating function used in the canonical transformation is given by [20]

$$G_x(x, \phi_x; s) = -\frac{x^2}{2\ \beta_x}[\tan F_x + \alpha_x] \tag{2.37}$$

where

$$F_x \equiv \psi_x - \mathrm{Q_x}\theta + \phi_\mathrm{x}$$

This generating function produces the coordinate transformations

$$\begin{cases} x = \sqrt{2J_x\ \beta_x}\cos(\tilde{\psi_x} + \phi_x) \\ x' = -\sqrt{\frac{2J_x}{\beta_x}}\Big[\sin(\tilde{\psi_x} + \phi_x) + \alpha_x\cos(\tilde{\psi_x} + \phi_x\Big] \end{cases} \tag{2.38}$$

and the new Hamiltonian is

$$H_1 = H(x, x'; s) + \frac{dG_x}{ds} = \frac{\mathrm{Q_x J_x}}{R}. \tag{2.39}$$

The parameter R is a scaling of the longitudinal parameter s[2]. The equation of motions are given by

$$\dot{\phi}_x = \frac{\partial H_1}{\partial J_x} = \frac{\mathrm{Q_x}}{R} = \frac{2\pi}{C}\mathrm{Q_x} \qquad\qquad \dot{\mathrm{J}}_\mathrm{x} = \frac{\partial \mathrm{H_1}}{\partial \phi_\mathrm{x}} = 0 \tag{2.40}$$

where the dot indicates a derivative with respect to s and C is the circumference of the accelerator (it is $2\pi R = C$). From the two equations of the motion 2.40 it follows that the action J_x is a constant of motion, that is with no beam-beam interaction the amplitude of a particle at a given location remains constant.

From the Ehrenfest adiabatic theorem [21] it results that for a slow variation of an oscillator's parameters the canonical variables of the motion evolve in such a way that the action integral on one oscillation period is constant, that is:

$$J_x = \frac{1}{2\pi}\oint p_x dx = (\frac{1}{2\pi}\mathrm{area}) = \mathrm{constant} \qquad \rightarrow \qquad \mathrm{area} = 2\pi \mathrm{J_x}$$

J_x is an invariant related to the area enclosed by the ellipse in (x, x') phase space which rotates periodically is s . If a particle has initial conditions which begin on some ellipse given by a given action value then the particle stays on this ellipse.

[2]By rescaling the Hamiltonian using θ, the parameter R can be eliminated. Recalling that $d/d\theta = Rd/ds$ the Hamiltonian can be written as

$$H_2(J_x, \phi_x; s) \cdot R = \mathrm{Q_x J_x}.$$

An equivalent derivation of the equations of motion holds for both transverse degrees of freedom. The unperturbed part of the Hamiltonian H_0 described by Equation 2.36 is thus

$$H_0(J_x, \psi_x, J_y, \psi_y) = \frac{2\pi Q_{x0}}{C} J_x + \frac{2\pi Q_{y0}}{C} J_y \tag{2.41}$$

where and Q_{x0} and Q_{y0} are the betatron tunes of the particle.
This system is equivalent to a system of two uncoupled harmonic oscillators.

The equations of motion are

$$\begin{cases} \dot{\psi}_x = \frac{\partial H_0}{\partial J_x} = \frac{2\pi Q_{x0}}{C}; & \dot{J}_x = -\frac{\partial H_0}{\partial \psi_x} = 0 \\ \dot{\psi}_y = \frac{\partial H_0}{\partial J_y} = \frac{2\pi Q_{y0}}{C}; & \dot{J}_y = -\frac{\partial H_0}{\partial \psi_y} = 0 \end{cases} \tag{2.42}$$

From the two equations of phase motion 2.42 the betatron tunes come out to be:

$$Q_x = \frac{C}{2\pi}\frac{\partial H_0}{\partial J_x} \qquad \text{and} \qquad \mathrm{Q_y} = \frac{\mathrm{C}}{2\pi}\frac{\partial \mathrm{H_0}}{\partial \mathrm{J_y}} \tag{2.43}$$

2.7 The Beam-Beam Potential in Action-Angle Variables

Let us write the beam-beam potential V_{BB} in action-angle coordinates for a beam colliding at one interaction point, with the approximation $\sigma_L / \beta_y^* < 1$. The assumptions described by the last approximation is that the bunch length is short compared to the vertical betatron functions at the interaction point so that the transverse particle distribution in the x-y plane does not change significantly during the interaction and the impulse can be considered to be a localized delta function perturbation. If a Fourier decomposition is also performed, V_{BB} is given by [22]

$$\begin{aligned} V_{BB} = -\frac{N r_e}{C\gamma} \sum_{m,np,r=-\infty}^{+\infty} T_{pr}(J_x, J_y) exp\Big[-\frac{k_{pr}^2 \sigma_L^2}{8}\Big] \cdot \\ \cdot\, i^m J_m(k_{pr}\hat{\tau}c/2) exp\Big[i\Big(p\psi_x + r\psi_y - 2\pi(n - mQ_s)\frac{s}{C}\Big)\Big] \end{aligned} \tag{2.44}$$

where k_{pr} is the wave number:

$$k_{pr} = k + p(\frac{1}{\beta_x} - \frac{2\pi Q_{x0}}{C}) + r(\frac{1}{\beta_y} - \frac{2\pi Q_{y0}}{C}). \tag{2.45}$$

and the amplitude detuning function of the resonant Hamiltonian T_{pr} (see Section 2.9 for a brief description of its physical meaning) is found by averaging the beam-beam potential over all angles:

$$T_{pr} = \frac{1}{(2\pi)^2} \int_0^{2\pi} d\theta_x e^{-ip\theta_x} \int_0^{2\pi} d\theta_y e^{-ir\theta_y}.$$

$$\cdot \int_0^\infty \frac{dq}{\sqrt{(2\sigma_{x0}^2+q)(2\sigma_{y0}^2+q)}} \times exp\Big[-(\frac{2\beta_x J_x \cos\theta_x^2}{(2\sigma_{x0}^2+q)} + \frac{2\beta_y J_y \cos\theta_y^2}{(2\sigma_{y0}^2+q)})\Big] \quad (2.46)$$

The integral T_{pr} is zero when either p or r is odd. The symmetry of the potential expression dictates that only even-ordered resonances will be driven in head-on collisions.

Just like any nonlinear resonance driving term, caused by sextupole magnets or octupole magnets for example, these driving terms excite resonances whenever the betatron tunes $\mathrm{Q_x}, \mathrm{Q_y}$ and the synchrotron tune $\mathrm{Q_s}$ satisfy the resonance condition:

$$p\mathrm{Q_x} \pm \mathrm{rQ_y} \pm \mathrm{mQ_s} = \mathrm{n}$$

where the order of the resonance is given by summing the constants $|p| + |r| + |m|$. The integer n is the harmonic of the revolution frequency which drives the resonance. So in this case $|p| + |r|$ must be equal to an even integer and m can be any integer.

Odd-ordered resonances require the symmetry of the potential to be broken, and are present for example when the beams are separated transversely, when there is dispersion or a crossing angle at the collision point.

2.8 Beam-Beam Tune shift

The average value of the perturbation is given by the term with $p = r = m = n = 0$. All the other terms are oscillatory. When its phase varies rapidly, the effect of a term on the motion averages to zero quickly.
It is

$$< \frac{d\psi_{x,y}}{ds} > = < \frac{d(H_0 + V_{BB})}{dJ_{x,y}} > = \frac{2\pi}{C} Q_{x,y0} - \frac{Nr_e}{C\gamma} \frac{\partial T_{00}}{\partial J_{x,y}} \quad (2.47)$$

that is, the derivative of H_0 gives $2\pi/C$ times the nominal tune, and the average of the derivative value of the perturbation gives the average phase advance times $1/C$. A phase varies slowly if the tunes have special values leading to resonances.
As it results from Equations 2.42 that

$$< \frac{d\psi_x}{ds} > = \frac{2\pi}{C} Q_x \; ; \qquad < \frac{d\psi_y}{ds} > = \frac{2\pi}{C} Q_y \quad (2.48)$$

it follows from Equations 2.47 and 2.48 that the beam-beam tune shift is obtained from the derivative of the detuning term:

$$\Delta Q_x = \frac{Nr_e}{2\pi\gamma} \frac{\partial T_{00}}{\partial J_x} \; ; \qquad \Delta Q_y = \frac{Nr_e}{2\pi\gamma} \frac{\partial T_{00}}{\partial J_y} \quad (2.49)$$

The beam-beam interaction redefines the working point for particles with unperturbed tunes into a working area in tune space. Amplitude dependent tune shifts lead to a spread in particle tunes for a distribution of particles. For good beam lifetime and stable operating conditions, it is desirable to keep the entire area in which particles are spread in tune away from destructive resonance lines in tune space. Section 2.10 gives in detail the expression for both the radial and vertical tune shifts obtained starting from relations 2.49, relations that have been plotted in Figure 2.5 in the so called *beam-beam tune footprint*.

2.9 The Resonant Hamiltonian

In this section is studied in detail an isolated nonlinear resonance in two degrees of freedom supposing that the other resonances are far and only the isolated one determines the particle dynamics, that is, a 4-dimensional phase space with a time-dependent Hamiltonian.

A term in the Hamiltonian has resonant build-up when its phase varies slowly. The resonant condition is

$$\frac{d}{ds}\Big[p\psi_x + r\psi_y - 2\pi(n - mQ_s)\frac{s}{C}\Big] \approx 0 \tag{2.50}$$

or

$$p(Q_{x0} + \Delta \mathrm{Q_x}) + \mathrm{r}(\mathrm{Q_{y0}} + \Delta \mathrm{Q_y}) + \mathrm{mQ_s} = \mathrm{n} \qquad \mathrm{p, r\ \ even\ numbers} \tag{2.51}$$

where $(\mathrm{Q_{x0}}+\Delta \mathrm{Q_x})$, $(\mathrm{Q_{y0}}+\Delta \mathrm{Q_y})$ are the actual tunes, while $\mathrm{Q_{x0}}, \mathrm{Q_{y0}}$ the unperturbed betatron ones and $\mathrm{Q_s}$ the nominal synchrotron one. The resonance order equals to $|p| + |r| + |m|$.

The resulting *resonant* Hamiltonian is used to describe a particle's motion when its tune is close to a resonance of order $|p| + |r| + |m|$. The Hamiltonian of a single isolated resonance $H_{prm}(J_x, J_y, \psi_x, \psi_y)$ is [22]

$$H_{prm} = H_0 - \frac{Nr_e}{C\gamma}T_{00} - \frac{2Nr_e}{C\gamma}F_{prm}(J_x, J_y, \hat{\tau})\cos\left(p\psi_x + r\psi_y - 2\pi(n - mQ_s)\frac{s}{C}\right) \tag{2.52}$$

where F_{prm} for the case $\beta_x^* >> \beta_y^* \sim \sigma_L$ is:

$$F_{prm}(J_x, J_y, \hat{\tau}) \simeq T_{pr}(J_x, J_y) exp[-\frac{1}{2}(\frac{r\sigma_L}{2\ \beta_y^*})^2] J_m\Big[\frac{rc\hat{t}}{2\ \beta_y^*}\Big]. \tag{2.53}$$

The first term in the Hamiltonian of Equation 2.52 describes the linear motion of a particle with unperturbed betatron frequencies $\mathrm{Q_x}, \mathrm{Q_y}$ and synchrotron frequency

Q_s and it is given by expression 2.41. The last two terms are due to the beam-beam interaction. The term T_{00} is the *amplitude detuning* function which describes the variation of tune with amplitude due to the beam-beam interaction. The term F_{prm} is a beam-beam resonant excitation term and is known as the *resonant width* function.

A standard well-known canonical transformation can be used to go from action-angle coordinates of the unperturbed Hamiltonian to the action-angle coordinates of a resonance Hamiltonian:

$$(\psi_x, J_x) \rightarrow (\phi_x, K_x) \qquad \text{and} \qquad (\psi_y, J_y) \rightarrow (\phi_y, K_y)$$

where

$$\begin{cases} \phi_x = p\psi_x + r\psi_y - 2\pi(n - mQ_s)\frac{s}{C}; & \phi_y = \psi_y \\ J_x = pK_x; & J_y = rK_x + K_y \end{cases}$$

and the generating function for the transformation is:

$$F_2(\psi_{x,y}, K_{x,y}, \theta) = (p\phi_x + r\phi_y - 2\pi(n - mQ_s)\frac{s}{C})K_x + \psi_y K_y$$

The new Hamiltonian $H^1_{prm}(K_x, K_y, \phi_x, \phi_y)$ becomes

$$H^1_{prm} = \frac{2\pi}{C}(p\mathrm{Q_x} + \mathrm{rQ_y} - (\mathrm{n} - \mathrm{mQ_s})\mathrm{K_x} + \frac{2\pi}{\mathrm{C}}\mathrm{Q_y K_y} + \tilde{\mathrm{F}}(\mathrm{K_x}, \mathrm{K_y})\cos\phi_\mathrm{x}$$

where

$$\tilde{F}(K_x, K_y) = F_{prm}(pK_x, rK_x + K_y).$$

Since the Hamiltonian H^1_{prm} is independent of the independent variable s it is a constant of the motion. In addition however it is independent of ϕ_y. Therefore, the new action K_y is also an invariant. Thus, being

$$K_y = J_y - rK_x = J_y - rJ_x/p = \text{constant}$$

the following expression is obtained

$$J_y - \frac{r}{p}J_x = \text{constant} \tag{2.54}$$

Two distinct cases follow from Equation 2.54:

- Bounded motion in the case of a *difference* resonance:

  $$\mathrm{sign(p)} = -\mathrm{sign(r)} \qquad \rightarrow \qquad |\mathrm{p}|\mathrm{J_y} + |\mathrm{r}|\mathrm{J_x} = \text{constant}$$

  stability is guaranteed, the energy associated with the transverse motion can be transferred between the horizontal and vertical motions as long as the above sum remains constant; a growth in a particle's horizontal amplitude, for example, will lead to a decrease in a particle's vertical amplitude.

- Unbounded motion in the case of a *sum* resonance:

$$\text{sign(p)} = \text{sign(r)} \qquad \rightarrow \qquad |\text{p}|\text{J}_\text{y} - |\text{r}|\text{J}_\text{x} = \text{constant}$$

  there is no restriction on the energy associated with transverse motion, the horizontal and vertical actions can grow without bound and stability is not guaranteed.

It is usually said that sum resonances are dangerous resonances and that difference resonances are safe. It must be considered however that even in the case of bounded motion in amplitude space, a particle still has the potential of being lost due to a large amplitude growth in one dimension.

There are linear oscillations about the center of the resonance for small values of K_x and the full width of the resonance separatrix is

$$\Delta K_x = 4\sqrt{\left|\frac{2F_{prm}(J_{xR}, J_{yR}, \hat{\tau})}{p^2\frac{\partial^2 T_{00}}{\partial J_x^2} + r^2\frac{\partial^2 T_{00}}{\partial J_y^2} + 2pr\frac{\partial^2 T_{00}}{\partial J_x \partial J_y}}\right|} \tag{2.55}$$

In fact, it is found from [20] that in the case of an isolated resonance in two degrees of freedom with the Hamiltonian:

$$H = H_0 + \alpha(J_x, J_y) + f(J_x, J_y)\cos(p\psi_x + r\psi_y - 2\pi(n - mQ_s)\frac{s}{C}) \tag{2.56}$$

the maximum island width is:

$$\Delta J_x = \pm\sqrt{\frac{f(J_{x,R}, J_{y,R})}{[\frac{\partial^2\alpha(J_x,J_y)}{\partial J_x^2} + \frac{\partial^2\alpha(J_x,J_y)}{\partial J_y^2} + 2\frac{\partial^2\alpha(J_x,J_y)}{\partial J_x \partial J_y}]_{J_{xR},J_{yR}}}} \tag{2.57}$$

where J_{xR}, J_{yR} are defined as the amplitudes when the resonance condition is satisfied.

Only single isolated resonances have been discussed here. The interaction between resonances could be important, particularly for lifetime effects. Stochastic motion occurs when resonances overlap. I just mention that the *Chirikov criterion* [18] estimates the onset of stochastic instability.

2.10 Beam-Beam Tune Footprint

This section reports the expression for the beam-beam tune shift ΔQ_y that has been derived [22] starting from Equation 2.49[23]. With the same procedure ΔQ_x

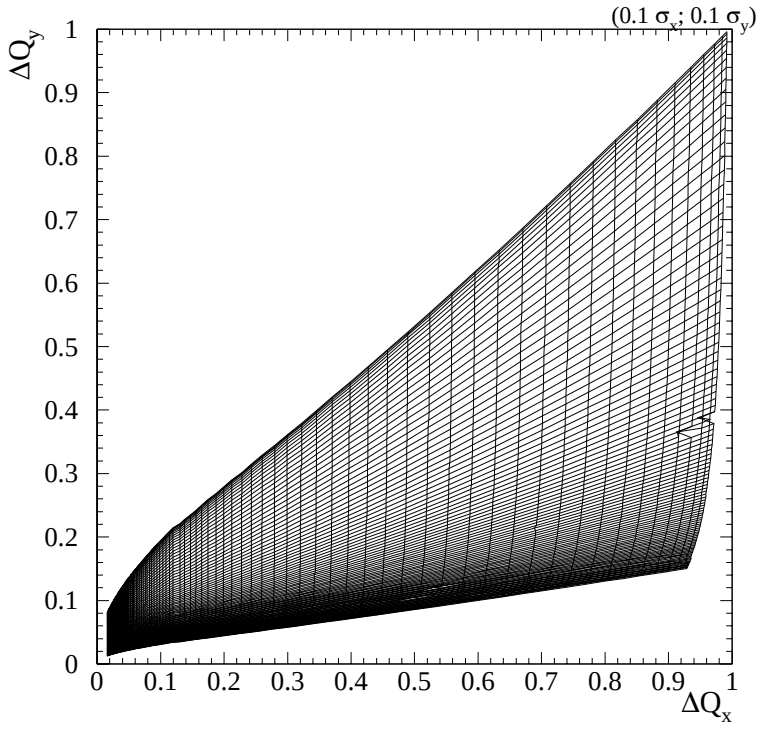

Figure 2.5: Beam-Beam tune footprint for one head-on collision. The footprint was calculated numerically for positrons with oscillation amplitudes ranging from 0.1σ to 10σ with steps of 0.1σ. The case of $\xi_x = \xi_y = 1$ is reported.

has been obtained:

$$\mathrm{Q_y} = \mathrm{Q_{y0}} + \frac{1}{2}\,\xi_\mathrm{y}\mathrm{r}(1+\mathrm{r})\int_0^\infty \mathrm{I_0(a)[I_0(b) - I_1(b)]}\frac{\mathrm{e}^{-(\mathrm{a+b})}\mathrm{dx}}{\sqrt{(1+\mathrm{x})(\mathrm{r}^2+\mathrm{x})}} \qquad (2.58)$$

$$\mathrm{Q_x} = \mathrm{Q_{x0}} + \frac{1}{2}\,\xi_\mathrm{x}\frac{(1+\mathrm{r})}{\mathrm{r}^2}\int_0^\infty \mathrm{I_0(a)[I_0(b) - I_1(b)]}\frac{\mathrm{e}^{-(\mathrm{a+b})}\mathrm{dx}}{\sqrt{(1+\mathrm{x})(1/\mathrm{r}^2+\mathrm{x})}} \qquad (2.59)$$

where $\mathrm{I_0}$ and $\mathrm{I_1}$ are the modified Bessel functions of zero and first order and

$$A_x = \frac{\sqrt{2\ \beta_x J_x}}{\sigma_x}; \qquad A_y = \frac{\sqrt{2\ \beta_y J_y}}{\sigma_y}; \qquad r = \frac{\sigma_y}{\sigma_x}$$

For the first integral 2.58 the variables a, b and x are given by:

$$a = \frac{\beta_x I_x}{2\ \sigma_x^2 + q} = \frac{A_x^2}{4(1+x)}; \qquad b = \frac{\beta_y I_y}{2\ \sigma_y^2 + q} = \frac{A_y^2}{4}\frac{r^2}{r^2+x}; \qquad x = q/2\ \sigma_x^2$$

For the second integral 2.59 the variables a, b and q are instead:

$$a = \frac{\beta_y I_y}{2\ \sigma_y^2 + q} = \frac{A_y^2}{4(1+x)}; \qquad b = \frac{\beta_x I_x}{2\ \sigma_x^2 + q} = \frac{A_x^2 r^2}{1/r^2+x}; \qquad q = 2\ \sigma_y^2 x$$

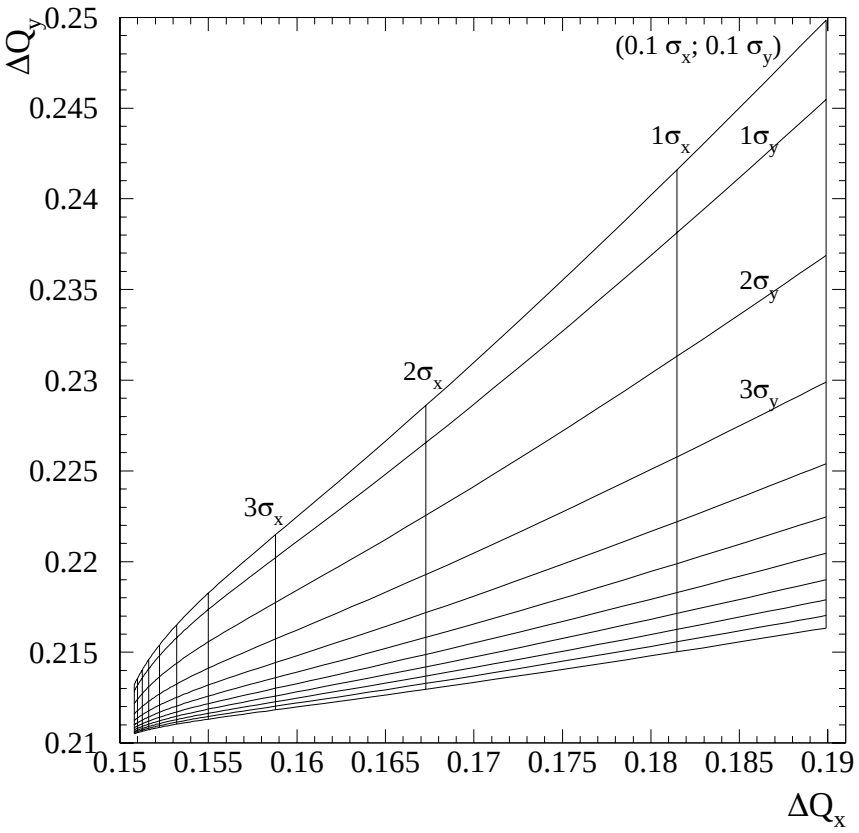

Figure 2.6: Beam-Beam tune footprint for one head-on collision in the flat beam approximation. The footprint was calculated numerically for positrons with oscillation amplitudes ranging from 0.1σ to 10σ with steps of 1σ, in the case of $\xi_x = \xi_y = 0.04$ and initial working point $(.15, .21)$ for $\sigma_y \ll \sigma_x$, as it is for DAΦNE , and $A_y \ll \sigma_x$.

The tune shifts of Equation 2.59 and 2.58 have been calculated numerically with oscillation amplitudes ranging from 0 to 10σ and the resulting plot is shown in Figure 2.5 for the case of $r = 0.01$ and $\xi_x = \xi_y = 1$.

In the DAΦNE machine it is $r = \sigma_y/\sigma_x = 0.01$, so the flat beam approximation is a very good one. For this reason can be used the tune footprint reported in Figure 2.6 which has been obtained with a numerical calculation of the two approximated equations evaluated for flat beams [24] in the region of $\sigma_y \ll \sigma_x$ and $A_y \ll \sigma_x$

$$\mathrm{Q_x} = \mathrm{Q_{x0}} + \xi_\mathrm{x}\frac{\sqrt{2}}{\pi \mathrm{A_x}}\int_0^{2\pi} \mathrm{F_D}(\mathrm{A_x}\cos\psi_\mathrm{x}/\sqrt{2})\cos\psi_\mathrm{x}\,\mathrm{d}\psi_\mathrm{x} \tag{2.60}$$

$$\mathrm{Q_y} = \mathrm{Q_{y0}} + \xi_\mathrm{y}\mathrm{I_0}\Big(\frac{\mathrm{A_x^2}}{4}\Big)\Big[\mathrm{I_0}\Big(\frac{\mathrm{A_y^2}}{4}\Big) + \mathrm{I_1}\Big(\frac{\mathrm{A_y^2}}{4}\Big)\Big]\exp\Big(-\frac{\mathrm{A_x^2}+\mathrm{A_y^2}}{4}\Big) \tag{2.61}$$

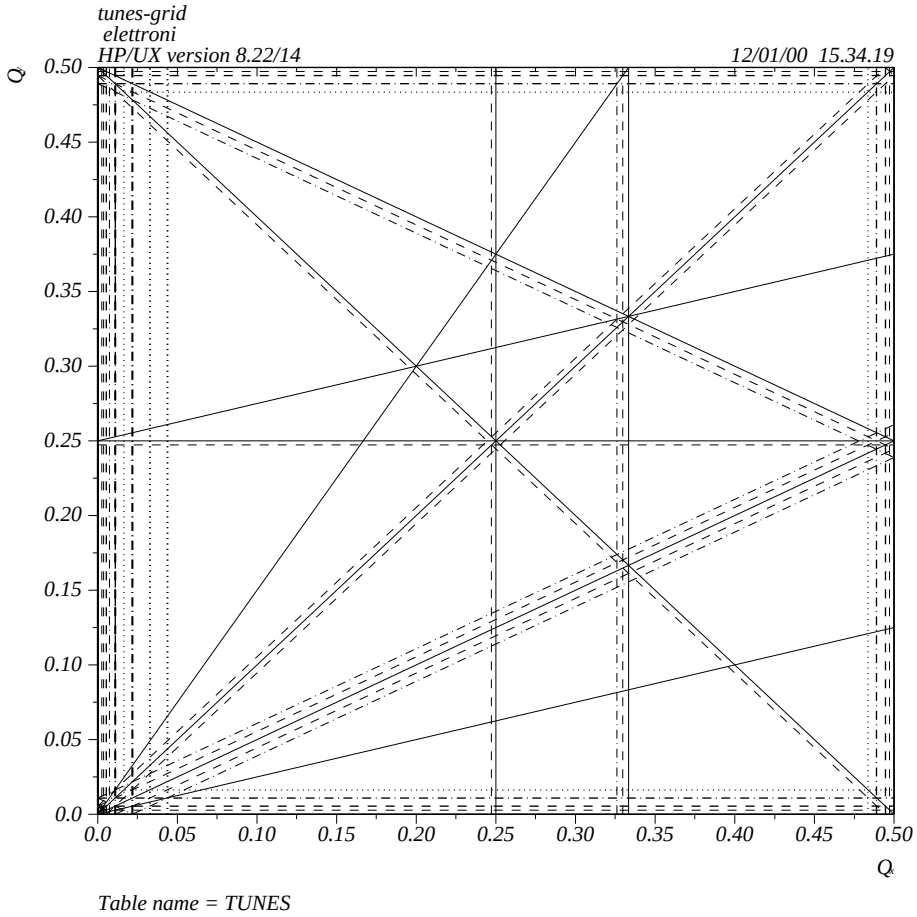

Figure 2.7: Typical working diagram or Q_x, Q_y plot showing some resonances near the operating region of DAΦNE .

These tune shifts are obtained from the derivative of the perturbation -the beam-beam potential- with respect to the action, where now the potential is the integral of the the flat beam approximated electric field.

As it results from the two Figures 2.5 and 2.6 the shift in tune decreases non-linearly with particle amplitude and very large amplitudes particles have almost no change in tune due to the beam-beam interaction. The beam has a range of tunes from $(\Delta Q_x, \Delta Q_y) = (\xi_x, \xi_y)$ at small amplitudes to $(0, 0)$ at very large amplitudes. For this reason ξ_x and ξ_y are often called the beam-beam tune spreads. The tune spreads are one consequence of the nonlinearity of the beam-beam interaction.
Figure 2.7 shows some resonances in the Q_x, Q_y plane. The beam-beam tune footprint has to be far from dangerous resonances. If any resonance line crosses the footprint then that will be a resonance induced by the beam-beam interaction.

The amplitude dependent tune shift which results from the beam-beam interac-

tion is predicted to have a stabilizing effect on a particle in resonance. If a situation in which a small amplitude particle is driven onto resonance and experiences amplitude growth is considered, the tune shift from the resonance as amplitude growth characterizes a *detuning* effect. The particle's amplitude will decrease as the particle is shifted in tune off a resonance. The detuning effect can bring the destructive effects of the resonance under control. This is an important aspect of the beam-beam force.

The Hamiltonian treatment helps to put the footprint between dangerous resonances in order to minimize collider performance degradation.

It also is very useful to understand experimental results and to undertake appropriate actions.

Chapter 3

Beam-Beam Simulations

Beam-beam simulations are particularly important in order to optimize luminosity and obtain a high performance of the machine. In this chapter there will be at first described the models that have been developed for beam-beam simulations, then will be presented the code I have used for the simulations.

3.1 Beam-Beam Simulations

Today's accelerator physicists do not seem to rely on beam-beam simulations in the same way as they do for other tools, like single-particle tracking. It is said sometimes that beam-beam simulations explain observed phenomena a posteriori rather than predict them. Of course the problem is the complexity of the beam-beam interaction. A rigorous simulation would require the solution of the equations of motions simultaneously for many billions of coupled particles for millions of turns. It is clearly impossible to reach the task with the present computers. Anyway, much is known qualitatively and quantitatively about the beam-beam interaction and many codes have been developed with different approximations. Simulations are of course an important part of beam-beam research. They are used to make performance estimates of colliders.

Test particles representative of those in the beams are tracked for a large number of turns with each turn consisting of transport between interaction points and collisions at the interaction points. Simulations of the arcs almost always include betatron and synchrotron oscillations, radiation damping and quantum excitations. Depending on the physics under study simulations have included other different phenomena, like lattice nonlinearities, wake fields, etc.

The difference between simulations is the treatment of the collisions. There are mainly two kinds of approaches: the so-called *weak-strong* model and *strong-strong* model. The main differences between these two approaches have been discussed from the physical point of view in Chapter 2. Let us see the implications for simulations.

3.1.1 Weak-Strong model

This is single particle, incoherent physics. Simulations are *weak-strong* when test particles in the *weak* beam are tracked and the distribution of the opposing *strong* beam is unaffected by the test particles. The strong beam is usually assumed Gaussian as it is described in Section 2.2, where it is shown that the electromagnetic kicks $(\Delta x', \Delta y')$ received by a positron from a thin-slice electron bunch are given by Equations 2.16 and 2.17. Actually, the value of the complex error function $w(z)$ defined in Equation 2.11 is calculated and stored for a grid of points. To calculate the actual beam-beam force of a particle in a certain position a Taylor expansion of $w(z)$ around this point is then sufficient. In tracking codes it is important to compute this function as fast as possible, being this the most CPU time consuming part of all beam-beam simulations (assuming a transverse Gaussian shape for the bunches).
The following assumptions are usually made in this weak-strong model:
(i) self-interactions of particles are neglected, being the particles relativistic;
(ii) there aren't lattice elements at the IP;
(iii) neither longitudinal nor transverse collective oscillations.
The beam-beam kick should be represented by a thick lens whose strength varies during the collision due to the s dependence of the transverse size of the opposing bunch. Usually the strong beam is passive and is represented by a Gaussian lens (thin or thick) that is not altered by the other beam [27]. The weak beam is dynamical, and its behavior can be observed as a function of time as it collides repeatedly against the strong beam. For the thin-lens case there is a single kick at the center of the bunch. For the thick-lens case, on the other hand, there is an infinite number of possible algorithms to decide the weights and locations of the kicks consistent with the basic constraints of symmetry distribution and of an accumulated effect of the kicks equal to the one in the original distribution.

I have used the beam-beam code LIFETRAC [26] for beam-beam analysis. This code is described in the following Section 3.2.

3.1.2 Strong-Strong model

In this section the aim is to give only a brief idea of some features related to the *strong-strong* modeling. So far I have described *incoherent, weak-strong* collisions. The particles in the second beam are independent of each other, and the fields and distribution of the first beam are unaffected by the second beam. But actually at the collision point the fields are strong and the beams modify each other's distribution and fields. So far I have been considering the incoherent motion of a single particle under the influence of the collisions. But usually, to get high luminosity the most usual mode of operation of a storage ring is that both beams are strong. It is not necessary that they are equal even though they usually are. This case of two equal bunches interacting with each other is called *strong-strong* case.

A first important effect that characterizes this strong-strong case which can not be observed in weak-strong simulations is the so-called *flip-flop*. It is observed that with the increased intensity of both beams one beam gains dominance over the other, blowing it up while reducing its own size. The collapsed beam becomes stronger and the blown-up beam becomes weaker. It is possible to reverse the roles of the two beams with an external asymmetrical influence. The flip-flop effect appears near the beam-beam limit at a given energy. Two beams tracked in *strong-strong* simulations modify each other's distributions. In simplified codes [28] [29] the test particles represent the beam and their coordinates are used to determine the distribution, and from that the electromagnetic fields at the interaction point and the beam-beam impulse. The means and rms widths from test particle coordinates are calculated and used in Equations 2.16 and 2.17 which give the beam-beam impulse for a given beam distribution -for example it can be assumed to be Gaussian.

Besides the flip-flop effects, strong-strong simulations using more sophisticated techniques [25] can see other effects not reproducible with weak-strong simulations, for example the coherent oscillations and the coherent beam-beam resonances where the two beams acquire very different beam sizes.

3.2 Description of LIFETRAC

LIFETRAC [26] is a weak-strong beam-beam code. It uses a special tracking technique for determination of lifetime, but it also predicts luminosity values. Although it is a simplification, the beam-beam problem can be divided into the two different regimes of core particles and halo particles. The core particles are those in the

high density part of the beam, and the distribution of these particles determines the luminosity. The halo particles are a different story. They do not determine the luminosity, but they affect the beam lifetime and the experimental backgrounds. These are as important as the luminosity, because the machine must operate with good lifetime and low backgrounds. Typically the tails are more populated than it is expected with a Gaussian distribution. I will briefly describe here the technique used to model these halo particles.

Let's start specifying the notations used in the code. The linear betatron motion around the ring is described with the variables:

$$\begin{cases} x(s) = A_x \sigma_x \cos\phi_x \\ x'(s) = -(A_x\sigma_x/\beta_x)(\sin\phi_x + \alpha_x \cos\phi_x) \\ y(s) = A_y \sigma_y \cos\phi_y \\ y'(s) = -(A_y\sigma_y/\beta_y)(\sin\phi_y + \alpha_y \cos\phi_y) \end{cases} \tag{3.1}$$

where A_x and ϕ_x are respectively the normalized amplitude and angle variables in the horizontal x betatron motion. x' is the non-canonical variable related to the canonical momentum by $x' \simeq p_x/p_0$. All the parameters σ, β, α are related to an unperturbed beam. The beam distribution in the radial plane (x, p_x) at the initial point is given by

$$P(x,p_x)dxdp_x = \frac{1}{2\pi\sigma_x\sigma_{p_x}} exp[-\frac{1}{2}((\frac{x}{\sigma_x})^2 + (\frac{p_x}{\sigma_{p_x}})^2)]dxdp_x \tag{3.2}$$

However is convenient to study the distribution in the space of amplitudes as they are slow variables. If a change of the coordinates system from (x, p_x) to (A_x, ϕ_x) is done as it is defined in the relations 3.1, one gets

$$dxdp_x = \left|\frac{\partial(x,p_x)}{\partial(\phi_x, A_x)}\right| dA_x d\phi_x \tag{3.3}$$

where the Jacobian is:

$$\left| det \begin{pmatrix} -A_x\sigma_x \sin\phi_x & \sigma_x \cos\phi_x \\ A_x\frac{\sigma_x}{\beta_x}(\cos\phi_x - \alpha_x \sin\phi_x) & -\frac{\sigma_x}{\beta_x}(\sin\phi_x + \alpha_x\cos\phi_x) \end{pmatrix} \right| = A_x\frac{\sigma_x^2}{\beta_x} = A_x\varepsilon_x \tag{3.4}$$

So Equation 3.2 becomes

$$P(A_x)dA_x d\phi_x = \frac{A_x}{2\pi} e^{-\frac{A_x^2}{2}} dA_x d\phi_x \tag{3.5}$$

Equation 3.5 integrated over 2π becomes a probability density function on normalized amplitude:

$$P(A_x)dA_x = A_x e^{-\frac{A_x^2}{2}} dA_x \tag{3.6}$$

This probability density function is normalized to 1 being

$$\int_0^\infty A_x e^{-\frac{A_x^2}{2}} dA_x = 1 \tag{3.7}$$

and it has a maximum for $A_x = 1$.
The amplitude is a non-canonical variable, but it is related to the canonical variable action by:

$$A_x = \sqrt{\frac{2J_x}{\varepsilon_x}} \quad ; \quad A_y = \sqrt{\frac{2J_y}{\varepsilon_y}} \tag{3.8}$$

For the canonical transformation of coordinates from (x, p_x) to (J_x, ϕ_x) the Jacobian is $\frac{\partial(x,p_x)}{\partial(\phi_x,J_x)} = 1$ and the probability density function in the action variable, after integration on ϕ_x is:

$$P(J_x)dJ_x = \frac{1}{\varepsilon_x} e^{-J_x/\beta_x} dJ_x \tag{3.9}$$

which is of course normalized to 1.

The actions -or amplitudes- are the appropriate variables to study because they change very slowly, due to nonlinear forces and quantum excitation. The idea is to take advantage of the slowly varying statistical nature of the changes in amplitudes. Thus, a particle in the tails does not jump from the core suddenly but it reaches the tails slowly after lots of beam-beam kicks, quantum excitations and dampings. So a particle in the tails loses memory of its history in the core. Instead of tracking billions of particle-turns in the core to get information about tail particles, LIFETRAC uses a technique briefly described below that permits to save a lot of CPU time to estimate the beam lifetime.

A single particle starts with zero amplitude and is tracked for a chosen number of steps where each step lasts for example 1000 damping times. During this time informations on the tracked particle are obtained. The algorithm proceeds with the following steps.

Step 1

In the normalized amplitude space a boundary is drawn that splits the plane in two. In this step is first necessary to obtain the initial distribution at small amplitudes and to draw the first boundary that is taken to be equal to one of the level lines (equal distribution density). The amplitude plane is divided in cells and when the particle is tracked the average number of times the particle falls in a cell is recorded. The cells with the same number make a level line. Each time the tracked particle

crosses the boundary (so called *outflight*) the particle's coordinates and momenta are recorded. This collected statistics will be used in the next step.

Step 2

In this step the internal region becomes a *hidden* region and the particles start from one of the recorded points during step 1. Each time it falls in the hidden region it is *restarted* from one of the *outflight* points selected randomly. In this step also the next boundary is calculated.

The algorithm proceeds in an iterative way: the old external region becomes hidden and the particle starts from the new external one.

It could be observed that this algorithm violates the course of events with time. But this rearrangement of events in time has no influence on the characteristics of motion due to the fact that it is a process with no memory, as the particle's behavior is independent from its history. What is important is to obtain the correct density and flows in the phase space and this is correct, as the probability of falling into a phase space cell when the particle leaves the hidden region is reproduced.

The final plots are made of level lines. The boundaries are level lines, but not all level lines are boundaries. The contour lines are spaced logarithmically, that is the density between two adjacent lines in the (A_x, A_y) plane decreases as $e^{-1/2}$ and the distance between the boundaries is usually chosen as 2.

The following ingredients are used to calculate the beam lifetime. The equivalent time that is the time necessary to get the same statistics with a conventional tracking technique (called *brute force technique*) in a given step (m+1) is given by

$$T_{eq}(m+1) = T_{eq}(m)\frac{N_R(m+1)}{N_C(m)}$$

where $T_{eq}(m)$ is the equivalent time calculated at the previous step, $N_R(m+1)$ is the number of *restarts* at the (m+1)th step and $N_C(m)$ is the number of crossings (*outflights*) at the mth step. The reduction of CPU time is the ratio between the number of restarts and that of crossings.

A died particle in a given step is an *outflight* particle.

Lifetime in a given step is the ratio between the *equivalent time* and the died particles in this step.

Noise is simulated by kicks whose values are given randomly by a Gaussian

distribution. The damping times are given in units of turns, they result from

$$\begin{cases} N_{dx} = N_{dy} = 2E_0/U_0 \\ N_{dz} = N_{dx}/2 \end{cases} \tag{3.10}$$

where E_0 is the rest energy and U_0 is the radiated energy of a single electron per turn. For DAΦNE it is $N_{dx} = 110540$, $N_{dy} = 109650$ and $N_{dz} = 54620$. Being N_{dx} the greatest one, it has been chosen as the natural time scale of the system.

As I said in the beginning of this chapter, in the weak-strong simulation codes a single particle interacts every turn with a fixed unperturbed strong Gaussian bunch. The luminosity is calculated in LIFETRAC according to its definition, it is the convolution between the unperturbed Gaussian distribution of the strong beam and the perturbed one of the weak beam multiplied by the revolution frequency:

$$\mathcal{L} = f_{rev} \cdot \int \rho_{STRONG} \rho_{WEAK} dxdydz \tag{3.11}$$

where f_{rev} is the particle's revolution frequency, ρ_{STRONG} is the density of the three-dimensional Gaussian representing the strong beam and ρ_{WEAK} is the weak beam's distribution. Actually the simulation gives the value of ρ_{WEAK}/N_{WEAK} that corresponds to a single particle distribution calculated averaging the particle's position each turn after many turns. Finally it is said that the luminosity is given by

$$\mathcal{L} = (f_{rev} N_{WEAK}) \cdot \int \rho_{STRONG} (\rho_{WEAK}/N_{WEAK}) dxdydz$$

where N_{WEAK} is given for an apriori fixed value of ξ and the value of the integral is given by the code output.
I just notice that N_{WEAK} in the end is set to be equal to N_{STRONG} and right here is the limit of the luminosity expected value found in the weak-strong beam: with this assumption we are not in the weak-strong case anymore and in this case the simulations should be done using the *strong-strong* model.

Chapter 4

Numerical Studies of Collisions with one IP in DAΦNE

Numerical simulations [31] have been carried out in order to find a suitable working point for beam-beam collisions with a single interaction point (IP) during the DAΦNE commissioning. Simulations have also been done to investigate the influence of the horizontal and vertical beam-beam separations at the second IP on the luminosity and lifetime. The possible degradation of machine performance due to vertical crossing angle and to sextupolar nonlinearities has been estimated.

Applying the model I have tried to explain some observations made during the machine luminosity runs. In particular the numerical luminosity scan carried out around the chosen working point with the experimental data has been compared, and attempt has been done to understand the bunch current saturation during injection into the nearest bucket while performing the so called *phase jump* procedure [34] and a sudden horizontal bunch widening of both electron and positron bunches at low currents have been analyzed.

Finally, modifications of the machine lattice necessary to provide successful DAΦNE operation with two interaction points are proposed.

4.1 Introduction

Numerical simulations [30] have shown that the optimal working point for DAΦNE is $(Q_x = 5.09; Q_y = 5.07)$, where Q_x and Q_y are the horizontal and vertical tunes, respectively. According to these simulations, at this working point the nominal

luminosity of $\mathcal{L} = 4 \cdot 10^{30}$ cm^{-2}s^{-1} in single bunch collisions can be reached with both the horizontal and vertical tune shift parameters ξ_x and ξ_y equal to 0.04.

However, during the commissioning stage it was decided to adopt a working point which is situated farther from integer numbers than (5.09; 5.07). In particular, as it will be explained in the following, the working point (5.15;5.21) has been chosen. Such a choice has been dictated by some reasons which were taken into account during the machine start-up, some of which are reported in the following.

1. The closed orbit distortions are more sensitive to machine errors for tunes closer to integers. For example, the orbit distortion Δx_{CO} due to an error kick $\delta\theta$ is proportional to:
$$\Delta x_{CO} \propto \frac{\delta\theta}{\sin \pi Q_x} \tag{4.1}$$

2. The machine straight sections and provisional *DAY-ONE* interaction regions (IR), which have been used only during the first stage of the commissioning, were not baked out. For this reason the pressure in the IR was substantially higher than its project value of 10^{-9} Torr, with the immediate consequence for the electrons of high positive tune shifts due to ion trapping in the residual gas. These tune shifts are proportional to the beam current I, to the neutralization factor η proportional to the gas pressure and inversely proportional to the transverse beam sizes σ_x and σ_y:
$$\Delta Q_{x,y} \propto \frac{I\eta}{\sigma_{x,y}(\sigma_x + \sigma_y)}. \tag{4.2}$$
Since the vertical beam size in DAΦNE is about one hundred times smaller than the horizontal one, the vertical tune shift ΔQ$_y$ is much higher than the horizontal one. This means that for the nominal working point (5.09; 5.07) the vertical tune is shifted towards the horizontal one, i.e. towards the main coupling resonance
$$Q_x = Q_y$$
and the betatron coupling is driven to values much above the design one ($\kappa = 0.01$).
This does not happen for working points which satisfy the relation: $Q_x < Q_y$.

3. A practical rule holds that the closer a working point is to integers or to resonances excited by sextupoles like:
$$\mathrm{Q_x} = 2\mathrm{Q_y} \qquad\qquad 3\mathrm{Q_x} = \mathrm{n}$$

the smaller the dynamic aperture will be.

An indirect indicator of the dynamic aperture variations due to changes of the working point for on-energy particles is the dependence of the tunes on the particle oscillation amplitudes. What is generally expected is that the dynamic aperture is reduced when there is a stronger dependence of tunes on amplitudes.

To the first order of perturbation the tune shifts depend linearly on the action variables J_x and J_y, introduced in Section 3.2:

$$\Delta \mathrm{Q_x} = 2\mathrm{c_{11}J_x} + \mathrm{c_{12}J_y} \qquad\qquad \Delta \mathrm{Q_y} = 2\mathrm{c_{12}J_x} + \mathrm{c_{22}J_y} \tag{4.3}$$

where the coefficients $c_{11}, c_{12}, c_{21}, c_{22}$ depend on the actual working point, but also on the sextupole strengths and on the phase advances between the sextupoles.

The working point (5.09; 5.07) is rather close to integers and to the sextupole resonance

$$\Delta \mathrm{Q_x} = 2\Delta \mathrm{Q_y}$$

So for this point stronger dependencies of the tune shifts on amplitudes and a smaller dynamic aperture than the point (5.15; 5.21) which is shifted far from integers and from sextupole resonance lines are expected . In fact, it is found analytically that the coefficients for the working point (5.09; 5.07) are higher than those for the point (5.15; 5.21) where only sextupoles necessary to correct chromaticity were switched on (50 A and 60 A alternated for the four families):

- for (5.09; 5.07) it is $c_{11} = 914; c_{12} = c_{21} = -39; c_{22} = 758$
- for (5.15; 5.21) it is $c_{11} = 294; c_{12} = c_{21} = 36; c_{22} = 117$

4. The second order chromaticity is responsible for the parabolic tune variation as a function of momentum deviation and it is very sensitive to the tune choice [32]:

$$Q''_{x,y} \propto \frac{\cos^3 2\pi Q_{x,y}}{\sin 2\pi Q_{x,y}} \tag{4.4}$$

According to the latter relation the chromaticity behavior for tunes closer to integers gets highly nonlinear and therefore the chromaticity correction becomes more difficult. Moreover, the betatron tunes of off-momentum particles decrease as the absolute value of momentum deviation grows. This implies that when the tunes are close to integers, the particles having a momentum

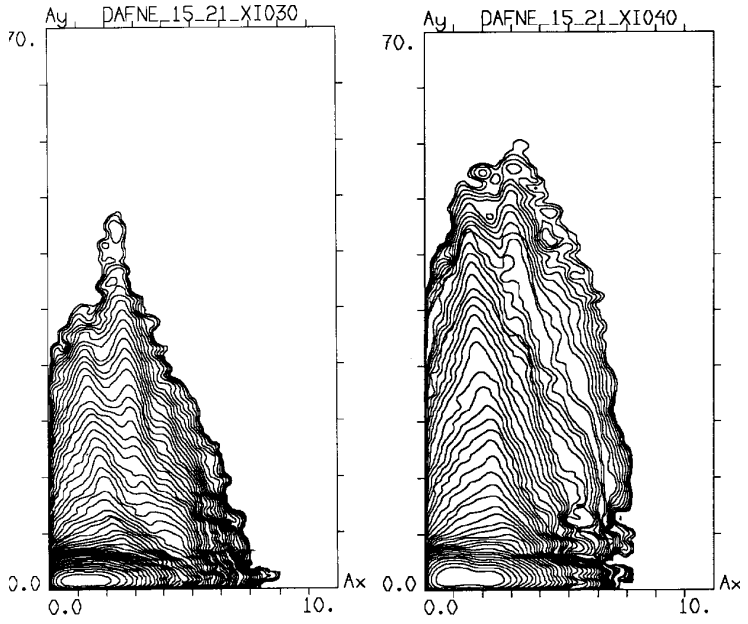

Figure 4.1: Equilibrium density in the space of normalized betatron amplitudes for DAΦNE working point (5.15; 5.21) with $\xi_x = \xi_y = 0.03$ (a) and $\xi_x = \xi_y = 0.04$ (b).

deviation above a certain value fall into the integer resonance stop-band and are lost. In particular, the short lifetime observed during machine tuning at the working point (5.09; 5.07) may, probably, be attributed to this effect.

4.2 Search for the DAΦNE Working Point

For the above considerations it has been looked for a working point situated far from integers and from sextupole resonances that could also provide a reasonable beam-beam performance, that means a good luminosity and an acceptable lifetime. Due to the lattice constraints the free betatron tune space is limited for the horizontal tunes in the range of $Q_x = 5.10 \div 5.20$ and for the vertical ones: $Q_y = 5.20 \div 5.30$. The numerical code BBC [33] is a weak-strong beam-beam interactions simulator and it has been used to perform a rough luminosity scan, i.e. in steps of 10^{-2} in both directions, in the useful tune space. Fifty particles interacting with a Gaussian strong bunch divided in five longitudinal slices have been tracked over ten radiation damping times, corresponding to about one million revolutions.

The results of the simulations with $\xi_x = \xi_y = 0.04$ have been summarized in Table 4.1. The first number in each cell represents the ratio between the calculated luminosity and the nominal one, defined as the value of luminosity for a given

Table 4.1: DAΦNE luminosity tune scan with $\xi_x = \xi_y = 0.04$.

Qx Qy	0.10	0.11	0.12	0.13	0.14	0.15	0.16	0.17	0.18	0.19
	0.7224	0.5568	0.4197	0.4173	0.5872	0.7076	0.4984	0.3047	0.1145	0.122
0.20	3.132	2.857	4.324	2.964	7.271	3.496	4.592	3.361	3.161	4.152
	23.52	16.46	17.05	35.12	30.10	14.81	20.19	34.68	41.45	67.49
	0.6925	0.5216	0.2660	0.3475	0.6843	0.6384	0.5512	0.5060	0.5209	0.2954
0.21	2.940	3.383	4.333	3.396	7.145	3.162	4.622	3.308	3.231	3.626
	13.85	18.67	24.07	30.80	39.60	23.56	10.87	18.74	17.82	35.48
	0.4821	0.4980	0.3988	0.3932	0.6204	0.5024	0.3656	0.5717	0.6132	0.6007
0.22	3.494	3.350	4.617	3.846	2.707	3.824	4.570	3.159	3.696	3.498
	36.92	15.89	21.17	38.36	17.03	23.02	29.53	13.77	20.73	12.63
	0.3541	0.3136	0.2538	0.4299	0.3677	0.3380	0.3160	0.4401	0.4102	0.3812
0.23	3.539	3.009	5.019	3.612	4.392	3.690	4.516	3.348	3.480	3.682
	12.07	12.51	18.70	25.24	20.27	17.14	17.63	19.47	16.85	21.57
	0.1702	0.1291	0.1333	0.1791	0.1782	0.1350	0.1846	0.1831	0.1536	0.1449
0.24	3.662	3.476	4.933	3.449	4.920	3.074	4.724	3.324	3.080	3.636
	25.75	23.18	23.59	20.74	23.40	28.88	24.81	20.71	26.85	27.27
	0.1179	0.0847	0.3658	0.1698	0.1204	0.0752	0.1671	0.5331	0.356	0.1636
0.25	3.089	3.669	5.295	3.091	4.547	3.242	4.870	3.326	3.442	3.520
	46.60	48.95	51.18	40.72	42.79	41.89	40.71	38.51	43.27	38.32
	0.5394	0.5465	0.6680	0.5413	0.5964	0.5485	0.5339	0.5990	0.3840	0.2516
0.26	3.718	3.579	4.327	3.550	3.726	3.990	4.601	3.226	2.905	3.584
	16.75	26.99	14.35	12.41	17.64	18.72	20.57	12.68	24.33	24.43
	0.5582	0.7437	0.468	0.5311	0.5667	0.6647	0.6086	0.4321	0.3551	0.1970
0.27	3.669	5.141	4.676	3.713	5.170	3.564	4.431	4.159	3.449	3.804
	20.24	25.86	17.47	20.37	26.59	23.21	19.25	25.11	23.15	24.12
	0.5196	0.3982	0.3580	0.4011	0.7884	0.7063	0.4572	0.4043	0.2124	0.1338
0.28	3.693	3.218	4.975	3.183	7.431	3.350	4.653	3.624	3.616	3.740
	29.37	24.01	23.88	24.93	35.63	25.48	11.59	11.54	14.77	19.71
	0.5165	0.3691	0.4959	0.5069	0.7724	0.5606	0.2777	0.2149	0.1046	0.0762
0.29	3.970	3.507	4.400	3.365	7.508	3.336	4.430	3.092	3.106	4.025
	29.48	27.46	38.50	31.40	34.46	12.81	15.38	18.13	28.80	38.45

Table 4.2: DAΦNE luminosity tune scan with $\xi_x = \xi_y = 0.02$.

Qx Qy	0.10	0.11	0.12	0.13	0.14	0.15	0.16	0.17	0.18	0.19
	0.9092	0.9105	0.8771	0.7383	0.6120	0.9893	0.8064	0.9733	0.6498	0.181
0.20	3.264	2.887	3.421	2.602	3.422	3.163	3.603	3.466	2.827	3.448
	29.19	5.755	5.405	7.064	17.47	4.731	5.680	9.042	15.98	27.17
	0.7144	0.9256	0.8724	0.4306	0.6175	1.006	0.8359	0.8357	0.8367	0.7833
0.21	2.950	2.786	3.178	2.958	4.808	3.536	3.345	3.196	2.980	3.326
	10.94	6.827	9.429	15.06	22.76	2.938	3.689	4.116	7.535	10.78
	0.7177	0.8623	0.815	0.6424	0.8687	0.8916	0.8270	0.7059	0.8479	0.8064
0.22	2.709	3.501	3.171	3.130	3.314	3.339	3.750	3.429	3.269	3.229
	10.85	12.89	5.735	13.81	10.48	5.674	5.066	16.60	9.512	4.671
	0.8418	0.6872	0.5902	0.7120	0.8116	0.8214	0.6128	0.7340	0.8609	0.8143
0.23	3.552	2.661	3.542	3.494	3.586	2.861	3.541	3.172	2.942	3.004
	8.965	12.69	8.429	17.12	4.880	10.25	5.320	10.01	5.042	4.038
	0.3407	0.3262	0.2429	0.342	0.3474	0.3395	0.2665	0.3196	0.363	0.3114
0.24	3.256	2.728	3.582	2.998	3.241	3.224	3.572	3.559	2.875	3.117
	8.555	12.05	14.03	13.40	11.79	12.02	16.43	13.99	11.49	10.26
	0.4910	0.2173	0.9101	0.3509	0.4197	0.2324	0.2056	0.3446	0.3983	0.3205
0.25	2.921	2.923	3.891	3.362	3.364	3.787	3.212	2.906	3.315	2.946
	20.86	20.64	26.00	19.87	21.45	21.01	20.93	20.93	20.70	20.69
	0.8449	0.5409	0.8024	0.9318	0.7542	0.7768	0.7655	0.8148	0.8969	0.8538
0.26	3.209	2.858	3.597	2.899	3.187	2.888	3.578	3.708	2.909	3.293
	6.512	12.64	8.895	8.053	6.675	10.26	7.184	8.982	4.085	4.996
	0.6213	0.8628	0.9089	0.7034	0.7016	0.9291	0.8668	0.8274	0.8994	0.7837
0.27	3.029	3.673	3.223	2.940	3.298	3.269	3.828	2.680	22.519	3.163
	8.697	17.23	3.227	11.93	9.139	12.96	5.438	9.614	14.79	8.938
	0.5687	0.9638	0.890	0.536	0.7106	0.9577	0.8580	0.9698	0.7899	0.5401
0.28	3.056	2.954	3.754	2.761	3.314	3.380	3.511	3.085	2.719	3.107
	17.86	5.888	5.992	11.30	17.61	5.754	3.195	2.992	6.169	7.556
	0.8465	0.9315	0.7271	0.7413	0.7401	0.9872	0.8929	0.8603	0.5453	0.1950
0.29	3.018	3.385	3.329	3.005	3.305	2.969	3.520	3.421	2.722	2.844
	14.24	10.53	12.72	17.20	13.15	2.966	2.711	3.995	8.910	16.23

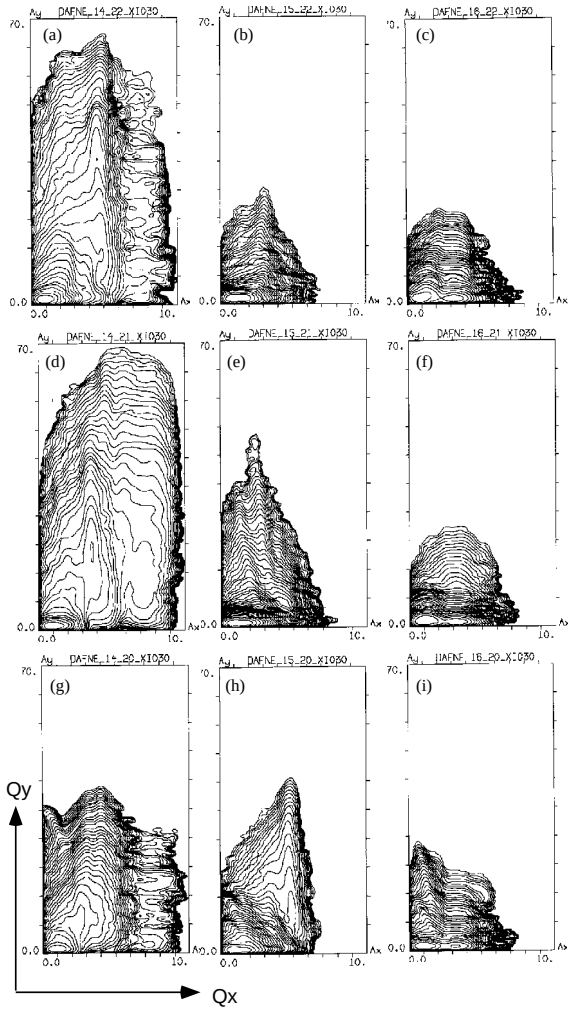

Figure 4.2: Luminosity scan around the working point (5.15; 5.21) with a tune step of 0.01: (a) (5.14; 5.22); (b) (5.15; 5.22); (c) (5.16; 5.22); (d) (5.14; 5.21); (e) (5.15; 5.21); (f) (5.16; 5.21); (g) (5.14; 5.20); (h) (5.15; 5.20); (i) (5.16; 5.20).

ξ_y and for the design values of the beam parameters. The second and the third number in each cell of the table are respectively the maximum horizontal and vertical amplitudes normalized to the rms beams sizes at zero current reached by the test particles. These numbers give a preliminary idea of the bunch distribution tail growth as a function of the working point . As it appears in Table 4.1 there is no working point in the explored tune area that withstands a strong beam-beam interaction, ($\xi_x = \xi_y = 0.04$), without beam blow-up. And for all these points a luminosity below its nominal value is predicted. Besides, long vertical tails created during the first ten damping times have been observed for almost all the investigated working points, and this sets a strong limit on the beam lifetime.

Reducing the value of the space charge parameter ξ it is possible to avoid the beam blow up and to enhance the lifetime, but this implies the reduction of luminosity. Table 4.2 shows the results of the numerical simulation for $\xi_x = \xi_y = 0.02$. The working point (5.15; 5.21) is the best among the investigated ones; in fact the simulation at this working point predicts a luminosity larger than the design one scaled by the reduction in ξ, and the tails distribution is confined horizontally in 4 σ_x and vertically in 3 σ_y.

In order to estimate the maximum luminosity and lifetime that can be reached at the chosen best working point simulations with the LIFETRAC code varying ξ from 0.04 to 0.02 have been carried out. Figure 4.1 shows the density contour plots for the cases $\xi_x = \xi_y = 0.03$ and $\xi_x = \xi_y = 0.04$: the contours are the lines of equal density of the equilibrium distribution in the space of normalized betatron amplitudes (see Section 3.2) and the density between two adjacent lines in the (A_x, A_y) plane decreases as $e^{-1/2}$. The displayed plots area is just the dynamic aperture of DAΦNE for a coupling of $\kappa = 0.01$, that is: $10 \cdot \sigma_{x0} \times 70 \cdot \sigma_{y0}$ [36].
One may compare these plots with Figure 4.9 (a) where the almost unperturbed Gaussian distribution is drawn. Generally, long tails in the distributions can limit the beam lifetime and increase the detector background. In these cases from the plots it is possible to understand how the nonlinear resonances disturb the equilibrium beam distribution. From now on I consider the value $\xi_x = \xi_y = 0.03$ of the space charge parameter as the maximum possible one for a non blown up beam at the working point (5.15; 5.21). The corresponding calculated horizontal and vertical normalized beam sizes are $\sigma_x/\sigma_{x0} = 1.08$ and $\sigma_y/\sigma_{y0} = 1.04$. The predicted luminosity for this working point and for these tune shifts values is equal to $2.2 \cdot 10^{30}$ cm^{-2}s^{-1}. As it results from Figure 4.1 (a) the beam distribution tails are well within the machine dynamic aperture. On the contrary, as it can be seen in Figures 4.1 (a) and (b) comparing the contour levels in the beam core at low amplitudes, in the case of $\xi_x = \xi_y = 0.04$ the beams sizes are significantly blown up. The corresponding calculated horizontal and vertical normalized beam sizes are $\sigma_x/\sigma_{x0} = 1.20$ and $\sigma_y/\sigma_{y0} = 1.46$. In this case of higher space charge parameter the beam tails get larger, but they are still contained within the dynamic aperture. Nevertheless, bunches with longer tails are more strongly affected by machine nonlinearities and in the end, they limit the lifetime.
Despite the blown sizes the luminosity is higher in the $\xi_x = \xi_y = 0.04$ case rather than in the $\xi_x = \xi_y = 0.03$ one, it it in fact $3.0 \cdot 10^{30}$ cm^{-2}s^{-1}. However I must remark that in the weak-strong simulations the strong beam is supposed to be

Gaussian and rigid, with nominal beam sizes. So, as the value of ξ gets higher the evaluation of the luminosity is less reliable, as the weak beam current in the end is set equal to that of the strong one. For high values of ξ a strong-strong simulation should be done. It is in this model, in fact, that the evolution of both interacting beams are taken into account.

4.2.1 Luminosity scan around the working point (5.15; 5.21)

In order to estimate the dimensions of a 'safe' area near the working point (5.15; 5.21) I have performed a numerical scan with the LIFETRAC code near this working point in steps of the order of 10^{-2}.

The results of this tune scan are reported in Figure 4.2 where the beam distributions are plotted in the amplitudes plane. As it appears from Figure 4.2 the working point is very sensitive to small tune variations. With a decrease of the radial tune from $Q_x = 5.15$ to $Q_x = 5.14$ the beam lifetime gets worse. When there is also a reduction of the vertical tune from $Q_y = 5.22$ to $Q_y = 5.20$ there is a fast tail growth, see Figures 4.2 (a),(d) and (g).
Some comparisons between the code's predictions and the experimental data can be done.
In the first stage of DAΦNE commissioning before KLOE installation the maximum single bunch luminosity has been $\mathcal{L} = 1.5 \cdot 10^{30}$ cm^{-2}s^{-1} reached at the working point (5.150; 5.210). This luminosity is somewhat smaller than the maximum value of $\mathcal{L} = 2.2 \cdot 10^{30}$ cm^{-2}s^{-1} predicted numerically for the same working point with $\xi_x = \xi_y = 0.03$ and design bunch current scaled with ξ $I_- = I_+ = 33$ mA because the collisions have been done at the lower current $I_- = I_+ = 25$ mA and with a lower beam-beam tune shift $\xi_x = \xi_y = 0.025$. This may suggest that a further improvement of the machine performance should be possible.
The direct comparison of the numerical results presented in Figure 4.2 with the experimental tune scan around the working point (5.150; 5.210) showed a good qualitative agreement. Let me explain better this comparison.

- $Q_x = 5.15 \rightarrow Q_x = 5.16$: increasing the radial tune the core horizontal beam size increased and the beam lifetime slightly improved. This is in agreement with the numerical simulations, in fact the points with $Q_x = 5.16$ (see Figures 4.2 (c),(f) and (i)) show an horizontally blown-up core with shorter vertical distribution tails, especially for (5.16; 5.20) (Figure 4.2 (i)).

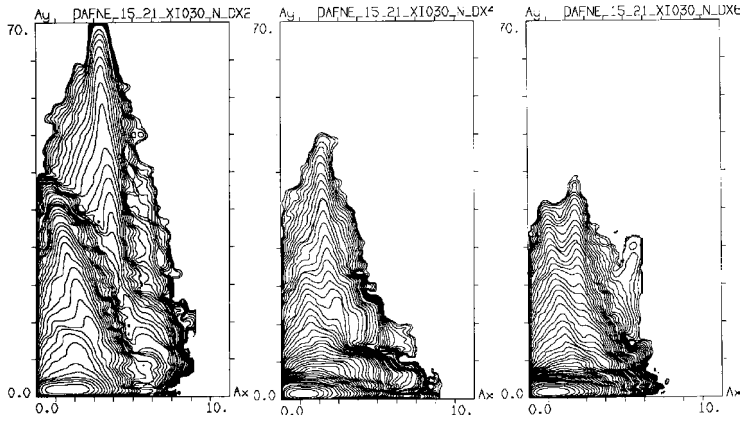

Figure 4.3: Equilibrium density contour plots for the working point (5.150; 5.210) with horizontal separations at the second IP of 2 σ_x (a), 4 σ_x (b) and 6 σ_x (c) respectively.

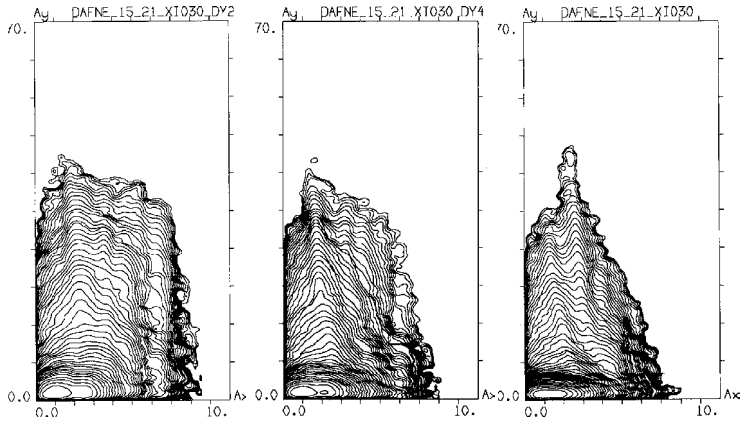

Figure 4.4: Equilibrium density contour plots for the working point (5.150; 5.210) with vertical separations at the second IP of 100 σ_y (a), 200 σ_y (b) and without the second IP (c) respectively.

- $Q_x = 5.14$ and $Q_y = 5.22 \rightarrow Q_y = 5.21 \rightarrow Q_y = 5.20$: reducing the vertical tune with the radial tune fixed at $Q_x = 5.14$ a degradation of the lifetime is experimentally observed. Numerically a tail growth for these points is predicted, as it is clear from Figures 4.2 (a),(d) and (g).

4.2.2 Beam-beam separations at the second IP

During commissioning, with collisions at a single IP horizontal and vertical localized orbit bumps have been applied to separate the electron and the positron beams at the second IP, in order to reduce the effects of parasitic interaction due to this second IP. Numerical simulations have been carried out to investigate how the DAΦNE

luminosity and lifetime depend on the beam-beam separations and in order to estimate the separation required to avoid beam-beam performance degradation.
The simulations have been performed for the working point (5.150; 5.210) taking into account the phase advance difference between the two IPs in the horizontal plane. For the simulations $\Delta Q_x = 2.453$ for the short-half and $\Delta Q_x = 2.97$ for the long-half of DAΦNE have been considered. The vertical phase advances have been assumed equal between the IPs.
Figure 4.3 shows the bunch distributions with radial beam separations at the second IP, respectively: 2 σ_x (a),4 σ_x (b) and 6 σ_x (c), where the nominal rms horizontal beam size at the IP is $\sigma_x = 2.12$ mm. It results from Figure 4.3(c) that with a beam separation of 6 $\sigma_x (\sim 12.7$ mm) the influence of the parasitic interaction at the second IP is practically canceled out. The luminosity keeps a value around $\mathcal{L} = 2.2 \cdot 10^{30}$ cm^{-2}s^{-1} with $\xi_x = \xi_y = 0.03$ and the distribution tails are not strongly affected by the parasitic collisions. A decrease of the horizontal separation from 6 σ_x (Fig. 4.3(c)) to 4 σ_x (~ 8.5 mm) (Fig. 4.3(b)) does not lead to a luminosity decrease but only to slightly longer tails. Reducing this beam separation from 4 σ_x to 2 σ_x (Fig. 4.3(a)), (~ 4.2 mm) there is a luminosity drop to the value $\mathcal{L} = 1.5 \cdot 10^{30}$ cm^{-2}s^{-1}. Moreover it is clear from Figure 4.3(a) that the long tails reach the borders of the DAΦNE dynamic aperture. The beam-beam induced tails together with the machine nonlinearities -not taken into account here- can drastically limit the lifetime.

The beams arriving at the second IP can also be separated in the vertical plane. The vertical separation has to be larger than about twice the horizontal rms size, and since the DAΦNE bunch is very flat ($\sigma_y / \sigma_x = 10^{-2}$) this implies that the vertical separation has to be bigger than $\sim 2\ \sigma_x = 200\ \sigma_y$.
In Figure 4.4(a) there is the beam distribution with a vertical beam separation of 100 $\sigma_y \sim 2$ mm, in (b) of 200 $\sigma_y \sim 4$ mm and in (c) with no second IP at all. Decreasing the bunch separation, that is going from the situation represented in the second case (b) of Figure 4.4 to the first case (a), the distribution enlarges horizontally so that it almost occupies all the horizontal dynamic aperture. The luminosity, in this last case (a) comes out to be $\mathcal{L} = 1.6 \cdot 10^{30}$ cm^{-2}s^{-1} and it reaches $\mathcal{L} = 1.9 \cdot 10^{30}$ cm^{-2}s^{-1} by increasing the vertical separation -case of Figure 4.4(b) that is not far from the value found with no second IP at all (Figure 4.4(c) $\mathcal{L} = 2.2 \cdot 10^{30}$ cm^{-2}s^{-1}).
Comparing Figures 4.3 and 4.4 it seems that the vertical beam separations are more effective, that is to get higher luminosity and shorter tails vertical bumps must be

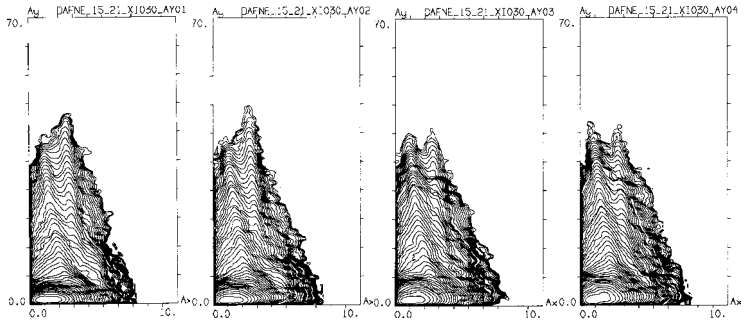

Figure 4.5: Equilibrium density contour plots for the working point (5.150; 5.210) with vertical crossing angle of 100 μrad (a), 200 μrad (b), 300 μrad (c) and 400 μrad (d).

applied.

4.2.3 Vertical crossing angle

As in DAΦNE the electron and positron beams are stored in two different rings they have different closed orbits. Even if the beams are carefully monitored and overlapped at the IP there is a not negligible probability of a vertical crossing angle between them at the IP, since at the low-β position any orbit change or drift is translated to an angle. It has been estimated that the possible vertical angle is of the order of $\sim 100 \div 200$ μrad, that is within the resolution measurement.
It has been numerically estimated whether such an angle can produce a bad lifetime or a degradation of the luminosity for the chosen working point . Figure 4.5 compares the amplitude distribution for different crossing angles: 100 μrad (a),200 μrad (b), 300 μrad (c) and 400 μrad (d). It results that up to 400 μrad the distribution tails are practically not affected by the vertical crossing angle. A moderate beam core blow up at the increase of the vertical crossing angle is predicted instead. Figure 4.6 represents the luminosity value predicted by the code as a function of the crossing angle. It can be deduced that the estimated vertical crossing angle does not limit the machine lifetime nor reduce the luminosity .

4.2.4 Machine nonlinearities

Lattice nonlinearities can significantly change the beam-beam performance with respect to that expected from simulations which do not take them into account. Besides, the combined effect of the nonlinearities and of the beam-beam collisions

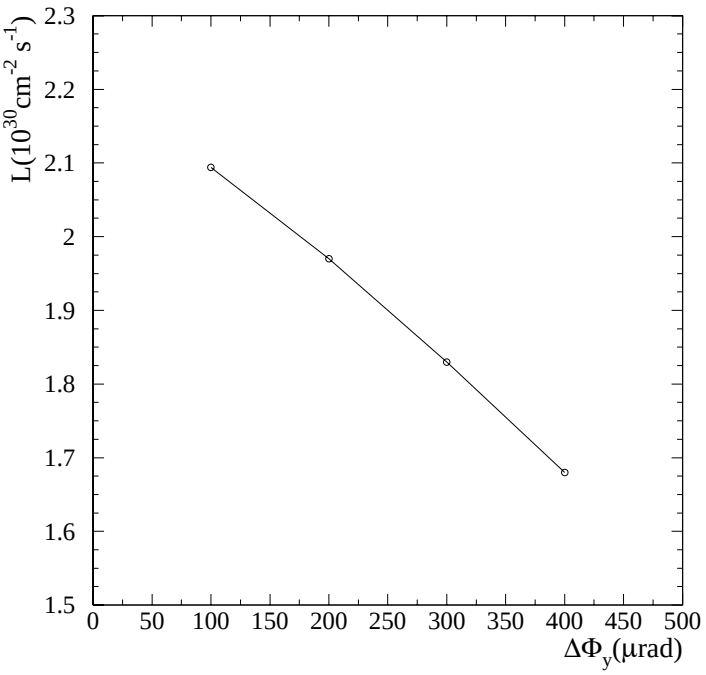

Figure 4.6: Luminosity as a function of the vertical crossing angle.

can differ from what is obtained when the two factors are considered separately.

The beam-beam interaction drives the particles to higher amplitudes where the nonlinearities get stronger, so that the distribution tails are changed. This can reduce the beam lifetime. However, strong nonlinearities can also affect the beam core leading to a decrease of the luminosity.
The machine sextupoles are the strongest source of nonlinearities in DAΦNE . It has been estimated numerically with the LIFETRAC code the situation when only the sextupoles for the chromaticity correction are switched on. The coefficients of the cubic nonlinearity introduced by the sextupoles have been calculated analytically, assuming the model β-functions and phase advances between the sextupoles.

Figure 4.7(b) shows the resulting beam distribution for the working point (5.150; 5.210). As it appears from this figure comparing to the case of the beam-beam interaction without nonlinearities (a), the beam core remains unchanged but the tails have strongly grown in case (b) reaching the dynamic aperture boundaries and limiting the lifetime. Neither the actual DAΦNE nonlinearities nor the dynamic aperture have been measured yet, so the above result is not a final answer about the machine lifetime. It is just a demonstration that one should tune carefully the sextupoles to

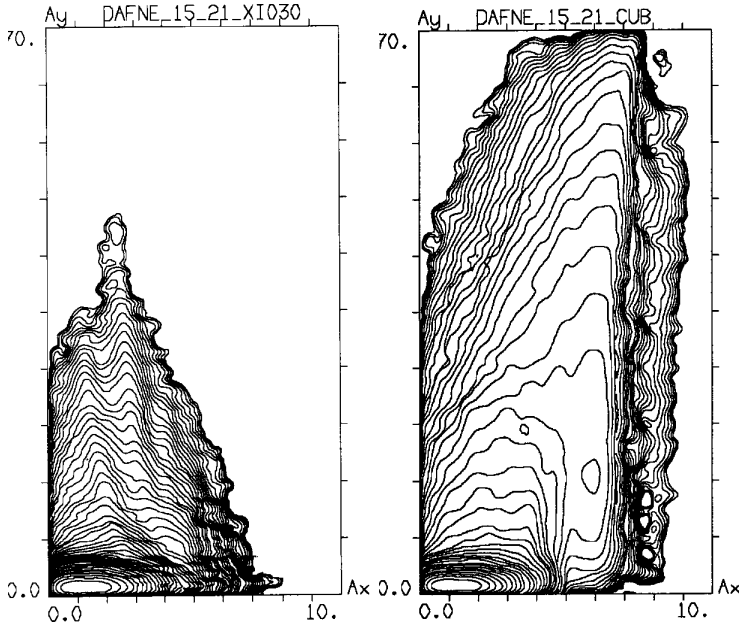

Figure 4.7: Equilibrium density in the space of normalized betatron amplitudes for the working point (5.150; 5.210): without lattice nonlinearities (a); with sextupole nonlinearities (b).

avoid lifetime problems.

4.2.5 Injection with parasitic crossings (PC)

During injection it has been observed that in the collision mode the intensity of the beam which was being injected saturated much below the nominal level. This has been explained by the fact that the injected bunch has both longitudinal and transverse oscillations for a period of time comparable with a radiation damping time. Such a bunch looses its intensity when it interacts with an opposite stored bunch.

A *RF Phase Jump* procedure has been adopted to fix this problem. Initially, the two bunches are injected into two RF buckets in such a way that they would not collide, in order to avoid beam-beam interactions during the accumulation of the current. Then, when the nominal intensity is reached, the stored bunches are brought into collisions by changing rapidly the phase of one of the RF cavities. In this way the orbit length in one of the main rings changes to compensate the initial longitudinal separation of the bunches.
The procedure has proven to be efficient when initially the bunches are separated by two RF buckets. However, when the longitudinal separation is reduced to a single

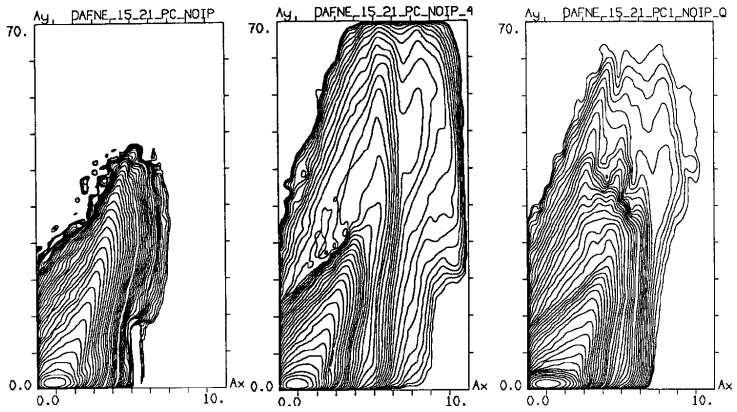

Figure 4.8: Tail growth due to parasitic collisions of bunches separated by one RF bucket: (a) *DEAR-IR* optics without sextupoles nonlinearities; (b) *DEAR-IR* optics with sextupoles nonlinearities; (c) *DAY-ONE* optics with sextupoles nonlinearities.

bucket the injection is still limited.

This can be explained in terms of parasitic crossings of the two bunches at a distance equal to a half bucket length from the main interaction point. In order to confirm this guess I have simulated this parasitic interaction with the LIFETRAC code. In particular, the situation when the opposite bunches do not collide at the main IP and the electromagnetic beam-beam interaction occurs only at a single parasitic crossing about 40 cm away from the main IP has been considered. The simulations have been carried out for both the *DAY-ONE* interaction region (IR) optics including the central quadrupole and the *DEAR-IR* optics with the quadrupole removed. In the first case of the *DAY-ONE* optics the interacting bunches are separated horizontally by 5.6 σ_x at the parasitic crossing point and the corresponding vertical β-function is $\beta_y = 4.11$ m. In the second case of the *DEAR-IR* optics the horizontal separation is 4.7 σ_x and $\beta_y = 3.69$ m. Figure 4.8(a) shows the equilibrium bunch distribution for the *DEAR-IR* optics not including lattice nonlinearities. In this case the tails grow beyond the parasitic crossing horizontal position that is $\sim 5\ \sigma_x$. However, the tails are well within the assumed dynamic aperture of $10 \cdot \sigma_{x0} \times 70 \cdot \sigma_{y0}$.

But, when the sextupole nonlinearities are taken into account, as it appears from Figure 4.8(b), the tails reach the dynamic aperture boundary and the lifetime gets as short as ~ 3 min. This means that the parasitic crossings acting together with the lattice nonlinearities may complicate the injection into the bucket next to the one where the opposite bunch is stored.

During commissioning the *DAY-ONE* optics was used. Since the horizontal separation for that optics is bigger than that for the *DEAR-IR* one the resulting

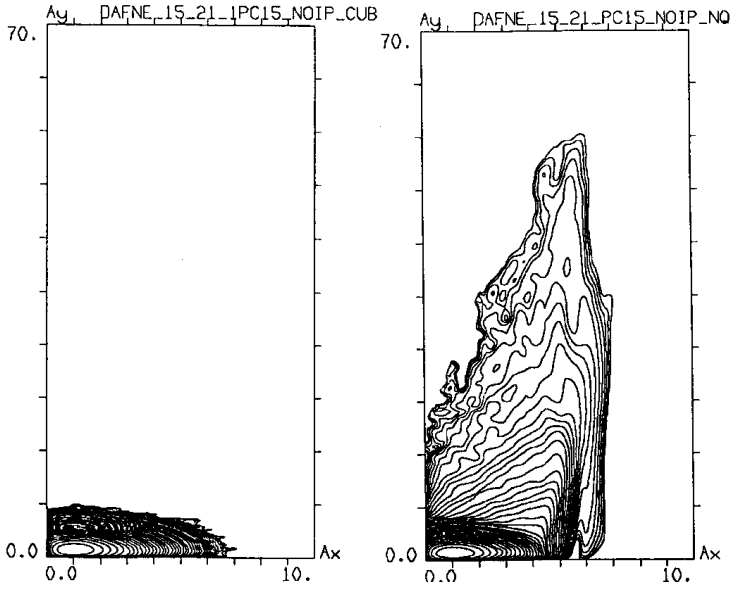

Figure 4.9: Tail growth due to parasitic collisions of bunches separated by 1.5 buckets one to the other and with the sextupolar machine nonlinearities taken into account: (a) *DAY-ONE* optics; (b) *DEAR-IR* optics.

distribution tails are shorter, as it appears in Figure 4.8(c) and the calculated lifetime is long enough, ($\approx$ 20 hours when only beam-beam is taken into account). It should be noticed however that the actual dynamic aperture and the machine nonlinearities are not measured yet and the sextupole correction has not been applied. This implies that the real situation can be significantly worse than that considered in the simulations, i.e. the dynamic aperture is smaller and the stronger actual nonlinearities may drastically reduce the machine lifetime with respect to the simulated one. In our opinion, the common effect of the parasitic crossings and the nonlinearities could explain injection saturation during the luminosity runs. At this point the question of how large the separation between the opposite bunches should be in order to avoid the parasitic crossing problem must be answered, or, in other words, how many bunches can be stored in each beam in order to apply the phase jump procedure without luminosity degradation due to injection saturation.

As the numerical simulations have shown, increasing the separation between the bunches to the distance of 1.5 buckets the problem of the parasitic crossings is practically eliminated. Figure 4.9 (a) shows the the bunch equilibrium density for the *DAY-ONE* optics, it is clear from the figure that the distribution remains practically Gaussian. Figure 4.9 (b) shows instead the density with the *DEAR-IR* optics and in this case there is a growth of weakly populated tails which do not limit

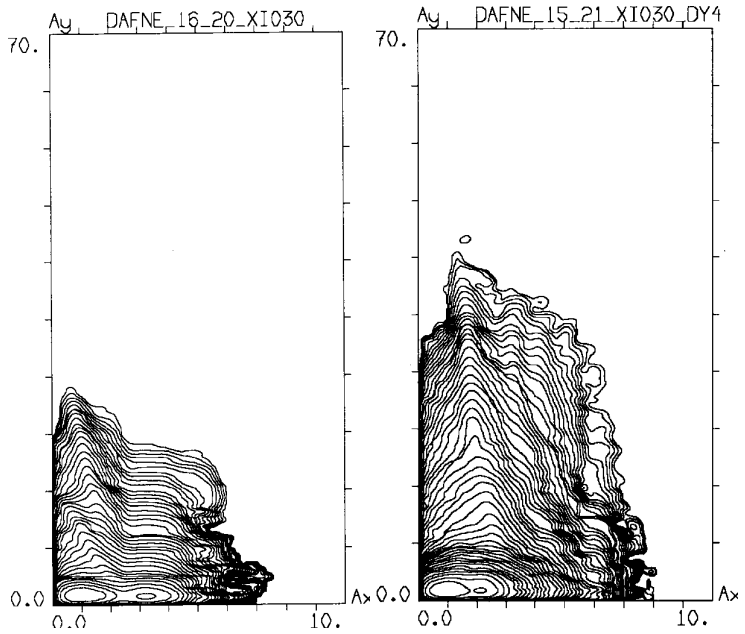

Figure 4.10: Examples of the horizontal bunch widening: (a) single IP interaction at (5.16; 5.20); (b) interaction at (5.150; 5.210) with the vertical separation of 4 mm at the second IP.

the lifetime.

It can be concluded that the phase jump procedure can be applied successfully for a maximum number of forty bunches stored in each colliding beam. The collisions of beams composed of sixty equidistant bunches is complicated by parasitic crossings forced by the lattice nonlinearities . However one can try to improve the situation by adjusting the machine sextupoles to compensate the cubic nonlinearity and by increasing the dynamic aperture. Nevertheless the most effective solution for the problem could be an increase of the horizontal separation in terms of σ_x, as it has been already proposed to avoid the PC problem in multibunch operation. In particular, the horizontal β-function at the IP has to be decreased by a factor two and by the same factor must be increased the vertical emittance. In this way the separation at the PC would increase by a factor of $\sqrt{2}$ in terms of σ_x and the luminosity and the beam-beam tune shifts are maintained unchanged.

4.2.6 Horizontal beam size widening

During DAΦNE luminosity operation a sudden widening of the horizontal beam sizes has been observed at some particular working conditions. The horizontal size of both interacting bunches seen at the synchrotron light monitor was blown up by

a factor of $2 \div 3$ and the vertical size remained instead unchanged. Sometimes, at the rather low and equal currents in the two bunches of $2 \div 10$ mA, two local density peaks separated horizontally on the monitor image could be distinguished.

In order to understand the origin of the phenomena a strong-strong beam-beam simulation with lattice nonlinearities would be necessary. Due to the absence of a reliable 3D strong-strong code, it is practically impossible to understand the above described effect. However, an hypothesis can be forwarded giving a possible explanation based on the weak-strong simulations. While performing the weak-strong simulations reported above situations with blown up radial dimensions and with two local maxima have been found .
Figure 4.10 shows two examples: (a) single IP interaction at the working point (5.16; 5.20) which is quite close to the nominal working point (5.150; 5.210); (b) interaction at the nominal working point (5.150; 5.210) with vertical separation of 4 mm at the second IP. The conclusion is that even small deviations from the nominal working conditions can excite a horizontal blow up with the appearance of the two local maxima.

Our analysis has shown that in both cases a strong betatron resonance of the sixth order $6Q_x = n$ was responsible for the above described effect. In addition, the external non linearity can increase or decrease significantly the resonance bandwidth, depending on its nonlinearity sign. In the most unfortunate case the bandwidth can be very large if the beam-beam induced nonlinearity is canceled by the machine nonlinearity.
So, it can not be excluded that the sixth order resonance was driving the effect. On the other hand, it is difficult to imagine a coherent strong-strong effect which could cause this phenomena since it has been observed at very low currents and correspondingly with low beam-beam tune shifts parameters $(0.002 \div 0.01)$.

4.2.7 Interaction with two IPs

It is highly desiderable to collide beams at the two interaction points in DAΦNE . This would allow to perform two DAΦNE experiments simultaneously.
However, an increase of the number of IPs usually leads to a luminosity reduction per each IP. One may expect a strong luminosity performance degradation if the phase advances of betatron oscillations between the IPs are different since the phase advance differences introduce new beam-beam resonances of low order. Because of that the choice of a suitable working point for the two IP collision scheme in

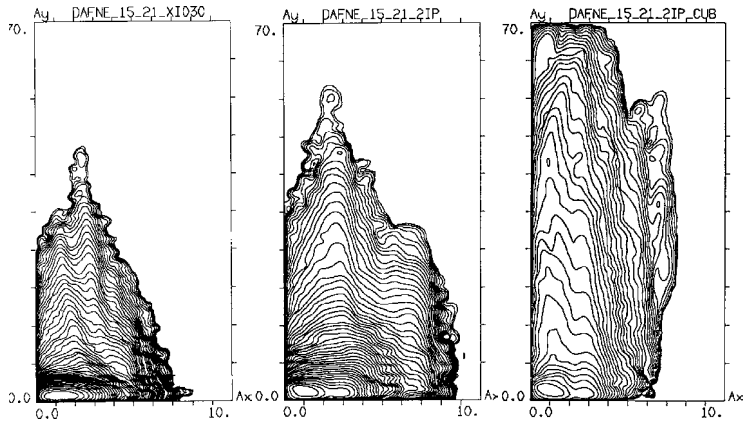

Figure 4.11: Equilibrium density in the space of normalized betatron amplitudes for the working point (5.150; 5.210): (a) single IP collisions without lattice nonlinearities ; (b) two IP collisions without lattice nonlinearities ; (c) two IP collisions with cubic (sextupoles) nonlinearities where the value of the coefficients of the cubic nonlinearity introduced by the sextupoles is: $c_{11} = -86; c_{12} = c_{21} = -144; c_{22} = 136$.

DAΦNE is not a simple task. Such a working point must satisfy the following, often contradicting, requirements:

- provide a good luminosity and a satisfactory lifetime with two IPs;
- provide a good beam-beam performance with a single IP since the luminosity should be maintained at a good level at the first IP while performing the luminosity adjustments at the second IP, like transverse beam-beam scan or longitudinal timing;
- provide a good dynamic aperture.

It appears that there are only a few working points which can satisfy these conditions. Their full description is presented in the next Chapter 5. The possibility to adopt the actual working point (5.150; 5.210) for the two IP collisions is now considered.

Figure 4.11 (b) shows the beam equilibrium density distribution for the working point (5.150; 5.210) with the two collision points and no lattice nonlinearity. As in the previous calculations, the horizontal phase advance difference between the two IPs is $\Delta Q_x = 0.24$ has been assumed as predicted by the machine lattice model. For comparison Figure 4.11 (a) shows the density distribution for the same working point but with a single collision point. As it is clearly seen the beam core is larger when the beams collide at the two IPs. The calculated luminosity decreases from

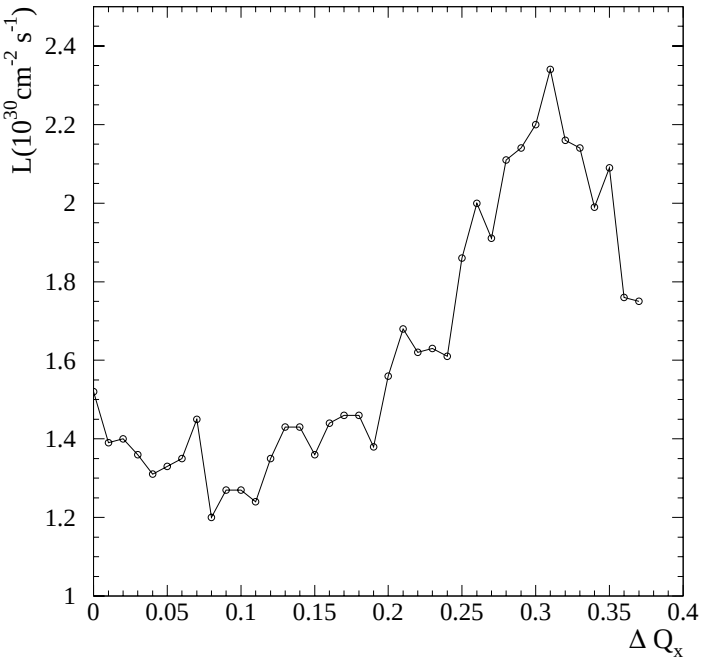

Figure 4.12: Luminosity as a function of the horizontal tune advance difference between the two IPs.

$\mathcal{L} = 2.2 \cdot 10^{30}$ cm^{-2}s^{-1} in the single IP collisions to $\mathcal{L} = 1.7 \cdot 10^{30}$ cm^{-2}s^{-1} per each IP in the case of the beams colliding at the two IPs.

The most important point is that the tail distribution gets much wider with two IPs. As it is shown in Figure 4.11 (b) the beam distribution occupies almost all the allowable horizontal dynamic aperture. This means that practically any small lattice nonlinearity could drive the particles beyond the dynamic aperture limits. Numerical simulations have been performed with the cubic nonlinearities estimated analytically for the most favorable case when the sextupoles for the chromaticity correction are adjusted to weaken the tune dependence on the betatron amplitudes. Indeed the density distribution in the case represented in Figure 4.11 (c) has very long relatively populated tails spreading beyond the vertical aperture boundary so reducing dramatically the beam lifetime to $\approx$ 25 s. This could be an explanation why the first experimental attempt to collide the bunches with currents higher than 10 mA at both IPs without the working point change and without any lattice correction has failed.

Figure 4.12 shows the dependence of the luminosity per each IP calculated with the LIFETRAC code as a function of the radial phase difference at $\xi_x = \xi_y = 0.03$.

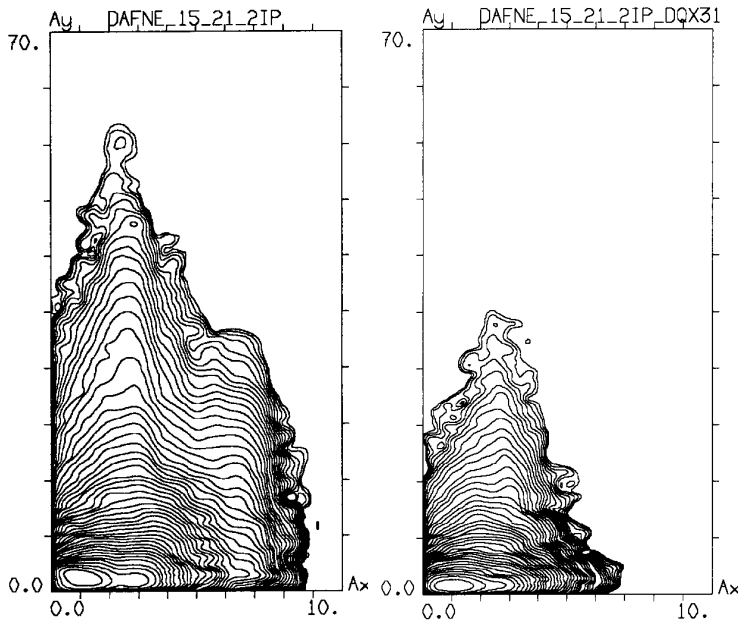

Figure 4.13: Equilibrium density in the space of normalized betatron amplitudes for the working point (5.150; 5.210) with two IPs and tune advance difference between the two IPs of: $\Delta Q_x = 0.24$ (a); $\Delta Q_x = 0.31$ (b).

I have assumed that the vertical phase advances are equal between the IPs. This assumption is very close to reality, as the vertical phase advance difference is small, it is $\Delta Q_y \approx 0.04$, and it can be easily be corrected. The result presented in Figure 4.12 is rather surprising for me since the maximum luminosity was expected to be reached when the phase (tune) advance difference is equal to zero. Instead, the maximum luminosity of $\mathcal{L} = 2.3 \cdot 10^{30}$ cm^{-2}s^{-1} corresponds to $\Delta Q_x = 0.31$. It seems that the phase advance differences not only create new beam-beam resonances, but can destroy some of the old strong ones. It would be very interesting to investigate this effect theoretically.

Fortunately, the tail growth is limited in such a way that all the bunch distribution stays well within the dynamic aperture for $\Delta Q_x = 0.31$.

Figure 4.13 compares the equilibrium density distributions for $\Delta Q_x = 0.24$ (a) and $\Delta Q_x = 0.31$ (b). By observing the Figures 4.12 and 4.12 it can be concluded that the slight readjustment of the machine lattice aimed at increasing the tune advance difference between the IPs from $\Delta Q_x = 0.24$ to $\Delta Q_x = 0.31$ can greatly improve the beam-beam machine performance with two interaction points.

The above result has also been checked simulating the quasi strong-strong beam-beam interaction with the dedicated code TURN [28].

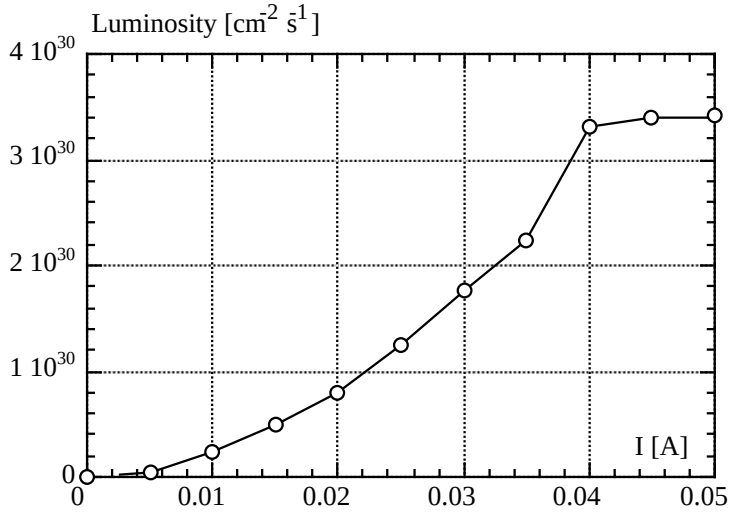

Figure 4.14: Luminosity as a function of the bunch current (quasi strong-strong simulation).

Figure 4.14 shows the dependence of the machine luminosity on the bunch current. In the simulations it has been assumed that the interacting bunches have equal currents. It appears from this figure that according to the quasi strong-strong simulations the luminosity that can be reached by increasing the tune advance difference to $\Delta Q_x = 0.31$ exceeds $\mathcal{L} = 3.0 \cdot 10^{30}$ cm^{-2}s^{-1} per each IP and saturates at the level of $\mathcal{L} = 3.4 \cdot 10^{30}$ cm^{-2}s^{-1} for currents close to the nominal DAΦNE current per bunch of 43 mA.
Weak-strong simulations with the LIFETRAC code with $\xi_x = \xi_y = 0.04$ that corresponds to the nominal current of 43 mA have been repeated and exactly the same luminosity as it is given by the TURN code has been found, that is $\mathcal{L} = 3.4 \cdot 10^{30}$ cm^{-2}s^{-1}, with slightly blown up beam sizes of the weak beam: $\sigma_x/\sigma_{x0} = 1.24$ and $\sigma_y/\sigma_{y0} = 1.29$.

4.2.8 Conclusions on the search of the DAΦNE working point

1. The numerical simulations have predicted that the working point (5.150; 5.210) seems to be the best one in the given tune range that can provide a reasonable DAΦNE beam-beam performance. The experimental luminosity runs are in a good agreement the numerical predictions. According to the simulations the maximum luminosity that can be reached at this point is $\mathcal{L} = 2.2 \cdot 10^{30}$ cm^{-2}s^{-1} without a significant size blow up.

2. Unfortunately, as the numerical tune scan have shown (see Tables 4.2 and

4.1) the safe area around the working point is very restricted. Tune shifts of $\Delta Q = 0.01$ in either direction lead either to bunch core blow up or to drastic lifetime reduction. This conclusion has been checked experimentally and the experimental data are in a good agreement with the simulations results.

3. A set of numerical simulations has been carried out to estimate the influence of the beam-beam separations at the second IP, both horizontal and vertical, on the machine luminosity performance. It has been found that the vertical separation at the second IP is more effective than the horizontal one. A vertical separation of more than 4 mm at the second IP would allow to minimize luminosity loss and lifetime reduction in the single IP collisions.

4. It has been shown numerically that a vertical crossing angle of the order of $100 \sim 200$ μrad neither limits the lifetime nor reduces significantly the luminosity . For a vertical crossing angle of 200 μrad the luminosity reduction is estimated to be of the order of ~ 0.1.

5. According to the simulations the sextupole nonlinearities can drastically reduce the lifetime. In order to minimize their effect one has to make a strong effort while performing the chromaticity and the dynamic aperture correction.

6. The numerical simulations indicate that the phase jump procedure can be applied successfully for equidistant forty bunches stored in each colliding beam. The phase jump procedure for the beams composed of sixty equidistant bunches is complicated by the parasitic crossings forced by the lattice nonlinearities . However, since the parasitic crossings themselves are not strong enough to limit the machine lifetime one should try to adjust the machine sextupoles to compensate or weaken the cubic nonlinearity and to increase the dynamic aperture in order to make possible the phase jump procedure with sixty bunches.

7. The hypothesis that the bunch widening observed at rather low currents for the given working point could be explained by strong horizontal betatron resonances of the sixth order $6Q_x = n$ has been forwarded. It should not be excluded that the bandwidth of the resonance is largely increased due to the compensation of the beam-beam nonlinearity by the machine nonlinearity -or the nonlinearity due to the parasitic beam-beam interaction at the second IP.

8. The numerical simulations of the beam-beam interactions with two IPs at the working point (5.150; 5.210) taking into account the cubic sextupole nonlinearity have shown a luminosity drop and fast tail growth of the bunch density

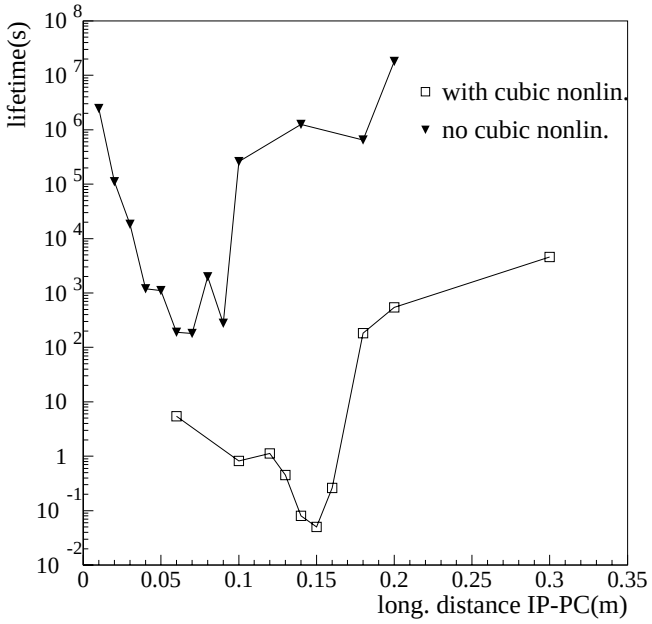

Figure 4.15: Beam lifetime at the increase of the longitudinal distance between a parasitic crossing and the IP, with and without nonlinearities .

distribution limiting the machine lifetime to about 20s. This seems to be an explanation why the first attempt to collide beams at two IPs with a reasonable current per bunch -higher than 10 mA- has failed. In order to fix the problem it can be proposed to increase the horizontal tune advance difference between the IPs from $\Delta Q_x = 0.24$ to $\Delta Q_x = 0.31$. In this case, according to LIFETRAC simulations, the luminosity at $\xi_x = \xi_y = 0.03$ is estimated to be $\mathcal{L} = 2.35 \cdot 10^{30}$ cm^{-2}s^{-1} per each IP with distribution tails well within the dynamic aperture. Moreover, both the quasi strong-strong code TURN and the weak-strong code LIFETRAC predict the possibility to increase the luminosity farther to about $\mathcal{L} = 3.4 \cdot 10^{30}$ cm^{-2}s^{-1} with moderate beam size blow up increasing the current per bunch to $40 \div 43$ mA, corresponding to $\xi_x = \xi_y = 0.04$.

4.3 Simulations on RF Phase Jump technique

Simulations on the *RF Phase Jump*[34] have been done using the LIFETRAC code.

RF Phase Jump is used mainly for multibunch operations in order to store a multibunch beam without disturbing the already stored opposite beam. The *Fast RF*

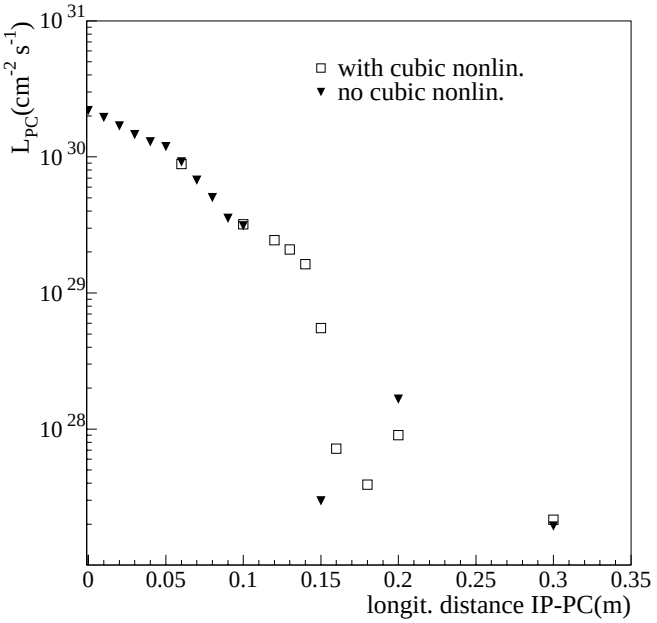

Figure 4.16: Expected beam luminosity at the parasitic crossing versus its longitudinal distance to the IP, with and without nonlinearities .

Phase Jump technique consists in injecting the beams longitudinally separated by two buckets and in putting them suddenly in collision by changing fast one RF phase by 4π radians. If the phase shift is fast enough the region of the parasitic crossings is traversed so rapidly that the beam-beam effects can not be disruptive.

On the other hand, moving slowly one beam to the other by adiabatically changing the phase of one RF, all the possible parasitic crossing points starting from one beam's initial position down to the IP are scanned. In this way the moving beam certainly crosses positions where the beam-beam effect is more critical than what expected at the IP and the beams, at least the weak one should be lost.

This hypothesis has been checked with simulations undertaken with the beam-beam code of an injected bunch with no interaction point (IP) but with a parasitic crossing (PC) at different longitudinal positions. The chosen working point for these simulations has been (5.15;5.21) that corresponds to the betatron tunes of the machine at the time of the phase jump technique adjustments. Parasitic crossings have been simulated both with and without nonlinearities, as it is shown in the two Figures 4.15 and 4.16.

Figure 4.15 reports the expected beam lifetime evaluated from the beam-beam code, that is taking into account the beam-beam interaction in the PC point, as a function

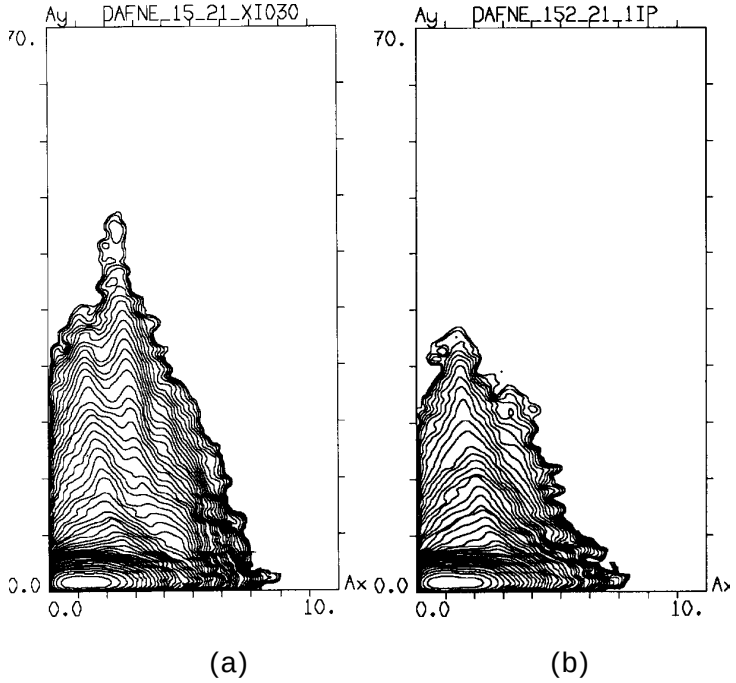

Figure 4.17: Beam tail reduction moving the working point from (a) (5.150; 5.210) to (b) (5.152; 5.210) .

of the longitudinal distance between the position of the PC and the IP. It is possible to compare in the figure the behavior of the beam in the case where only the beam-beam force is essential and that with cubic nonlinearities . It appears that the behavior is different for the two cases, as the beam lifetime is strongly reduced when nonlinearities are taken into account. In particular, a lifetime of 0.05 s is predicted for a PC at a longitudinal position of 15 cm.

Figure 4.16 reports the expected beam luminosity in the PC point as a function of the longitudinal distance between the position of the PC and the IP. The smaller the luminosity in the PC point, the better it is. The two cases with and without cubic nonlinearities are reported and the result is that the behavior is quite similar for the two cases.

To conclude, if the phase change is slow the beam will be lost.

4.4 Fine Tune Scanning around (5.150; 5.210)

During the first period after KLOE installation it has been found experimentally that the two DAΦNE beams are sensible to changes of the order of 10^{-3} in the betatron

tunes. In particular it has been observed a reduction of the beam tails moving the working point from (5.150; 5.210) to (5.152; 5.21). Firstly, the experimental results with the beam behavior predicted with simulations have been compared. As it appears from Figure 4.17 with a shift of the radial tune of $2 \cdot 10^{-3}$ the simulated tails are reduced.

This observation suggested to perform a fine betatron tune scanning nearby the working point (5.150; 5.210), moving with steps of the order of 10^{-3}.

4.4.1 Lifetime Optimization

In order to improve the DAΦNE beam lifetime a fine tune scanning has been performed from the starting point (5.150; 5.210) with a particular attention on the tails produced by the beam-beam force. Luminosity is in fact not so sensible to such small tune variations, as it keeps on values around 0.9 with respect to its nominal value for a beam-beam tune shift of $\xi_x = \xi_y = 0.03$ for all the investigated points.

It is reported in Figure 4.18 the beam distribution starting from (5.150; 5.210) and moving with steps of $2 \cdot 10^{-3}$: (a) in the radial plane from (5.150;5.210) to (5.160;5.210) and (b) in the vertical plane from (5.150;5.210) to (5.150;5.220). It has been considered a beam-beam tune shift of $\xi_x = \xi_y = 0.03$ and no cubic nonlinearities . These simulations show a reduction of the beam tails moving both horizontally and vertically, but the behavior is different for the two planes. As it appears from Figure 4.18 (a) from $Q_x = 5.150$ to $Q_x = 5.160$ the tails shrink a little bit but at the same time the beam core enlarges horizontally as Q_x gets near to 5.160. In the vertical plane instead the tails shrink from $Q_y = 5.210$ to $Q_y = 5.214$ where they reach a minimum and afterwards the tails enlarge again, as it is shown in Figure 4.18 (b).
Looking at the results of the simulations shown in Figure 4.18 it appears that in the explored area the best working point is (5.150; 5.214) as it presents the shortest tails.

In order to be sure that the minimum beam tails condition has been found also the working points (5.152;5.214) and (5.152;5.212) have been analyzed. The resulting distributions are shown in Figure 4.19 where they are compared to (5.150;5.214) and (5.150;5.212) respectively in Figure 4.19 (a) and (b).

In conclusion, this analysis suggests for DAΦNE to work at the point (5.150; 5.214). The simulations results agree with the experimental observations. The dedicated ex-

Table 4.3: Lifetime results for an experimental tune scan.

Q_{x-}	Q_{y-}	I_- (mA)	I_+ (mA)	τ_- (s)
5.153	5.211	15.0	5.0	2100
5.151	5.213	16.5	5.8	1500
5.150	5.212	15.8	5.6	3200
5.150	5.214	15.3	5.5	4000
5.150	5.214	13.9	5.9	4600

perimental tunes scan has been done for Q_y ranging from 5.210 to 5.214 with Q_x around 5.150. The summary of the lifetime results are shown in Table 4.3. It appears that the best lifetime correspond to the point (5.150; 5.214) as predicted by the simulations.

In the following section is shown the detailed analysis to verify this preliminary result.

4.4.2 Injection at the (5.150; 5.214)

As the previous section has shown simulations predict a better performance at the working point (5.150; 5.214) rather than (5.150; 5.210). Further analyses have been carried out to investigate the injection performance at the working point (5.150; 5.214).

As it is discussed in Section 4.2.5 the parasitic collisions may cause injection saturation for the working point (5.150; 5.210), the same analysis has been performed for the working point (5.150; 5.214). In order to compare the beam behavior at injection for these two wprking points the situation of opposite bunches beam-beam interacting with a PC at 40 cm from theIP has been considered. The DEAR IR optics has been considered, that is without the central quadrupole in the second IP and with a horizontal separation of 4.7 σ_x and a vertical β-function of $\beta_y = 3.69$ m at the parasitic collisions point. In Figure 4.20 is reported the resulting equilibrium bunch distribution without lattice nonlinearities . It clearly appears that at the working point (5.150; 5.214) the beam-beam parasitic collisions do not affect the Gaussian injected bunch.

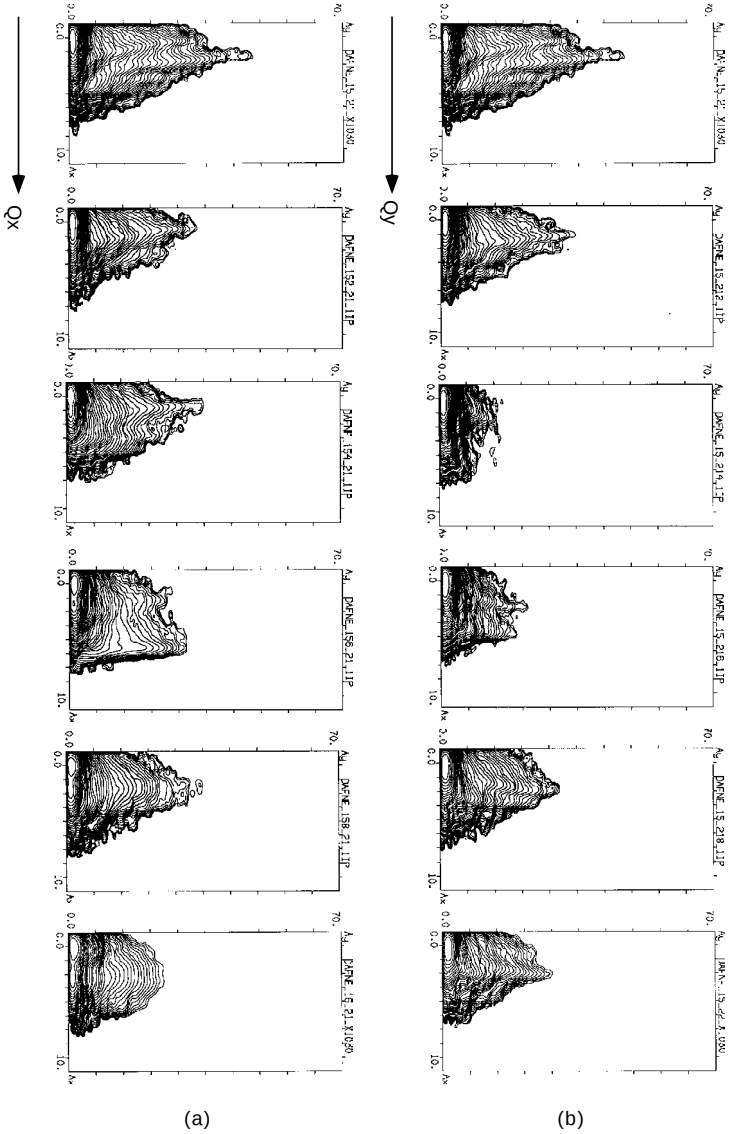

Figure 4.18: Fine scan starting from the working point (5.150; 5.210) the following points are:(a) (5.152;5.210), (5.154;5.210), (5.156;5.210), (5.158;5.210), (5.160;5.210); (b) (5.150;5.212), (5.150;5.214), (5.150;5.216), (5.150;5.218), (5.150;5.220).

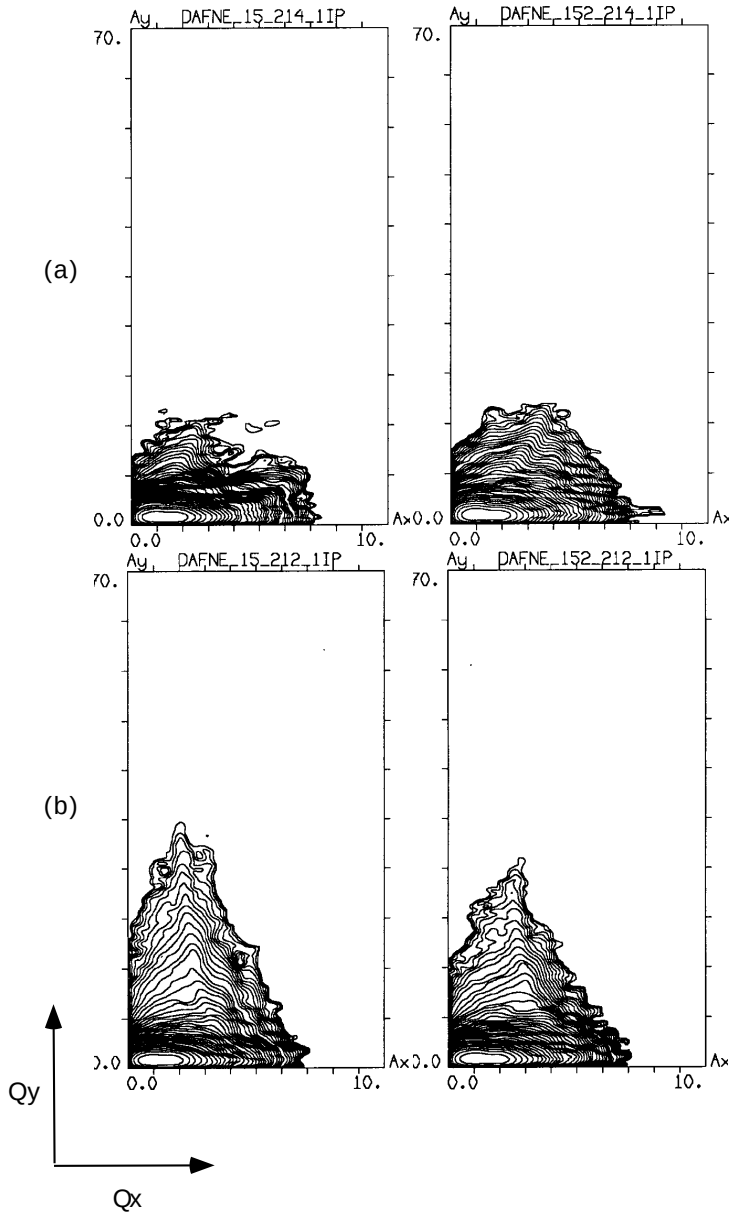

Figure 4.19: Beam distribution of the working point clockwise starting from the top left: (a)(5.150;5.214) (5.152;5.214) , (5.152;5.212) and (b)(5.152;5.212), (5.150;5.212).

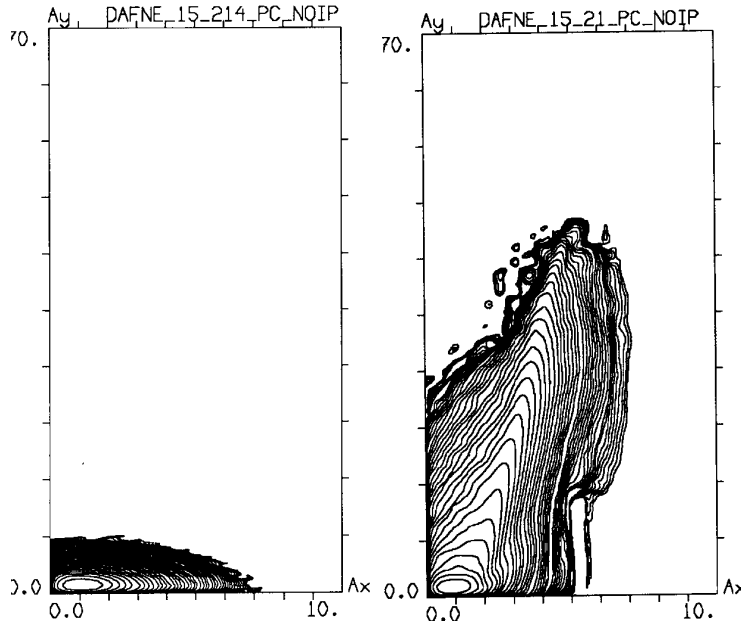

Figure 4.20: Tail growth due to parasitic collisions of bunches separated by one RF bucket with the DEAR IR optics and without sextupoles nonlinearities for the two working point (5.150; 5.210) and (5.150; 5.214).

Chapter 5

Numerical Studies of Collisions with 2-IPs in DAΦNE

Numerical simulations have been carried out in order to find a suitable working point for beam-beam collisions with two interaction points.

During the *DAY-ONE* phase of the commissioning the first tests with two IPs has been performed, showing 40% of luminosity reduction per IP and lifetime degradation. This pushed us to perform a study aimed to search a working point which could provide a good luminosity and acceptable lifetime while working for two experiments simultaneously. Now, after the KLOE detector installation, with the DEAR experiment ready to take data, the task of finding such a working point is getting more urgent.

Different working points have been investigated using the beam-beam code LIFETRAC and varying the phase difference between the two IPs with the aim to obtain decent machine performance in both single IP and two IPs collisions at the same time.

5.1 Introduction

An increase of the number of IPs usually leads to a luminosity reduction. In principle different phase advances of betatron oscillations between the two IPs produce a luminosity reduction because of the introduction of new beam-beam low order resonances [19]. But the phase difference between the two IPs can also be adjusted in such a way to destroy otherwise dangerous resonances. So, a scan on the tune

advance difference between the two IPs has been performed for each investigated working point in order to optimize the luminosity performance by varying this free parameter.

A good working point for the two IPs collision scheme in DAΦNE must satisfy the following requirements:

- it must provide a good dynamic aperture;
- it must provide a good luminosity and lifetime with a single IP in order to allow the tuning of each IP separately;
- and finally it must provide a good luminosity and lifetime with two IPs.

The investigated tunes with the weak-strong code LIFETRAC are the following ones: $(5.15; 5.21)$; $(5.16; 5.21)$, $(5.11; 5.21)$, $(5.145; 5.09)$, $(5.10; 5.14)$, $(5.52; 5.59)$.

The first working point is that which has been used during the *DAY-ONE* commissioning phase (see the previous Chapter 4), our studies start from here.

The second and the third working points are situated near the present working point and it is not necessary to modify substantially the machine lattice to tune the collider at these points. Moreover, the second one has been experimentally found to be a good point during the commissioning with the KLOE optics providing the best lifetime.

The fourth and fifth point have been investigated after the satisfactory results of a luminosity scan with the BBC code. These points provide good luminosities in single IP collisions.

The last point is the one where CESR collider successfully works [35]. This point is also suitable for DAΦNE , since it is one of the few working points where the DAΦNE nominal luminosity of $\mathcal{L} = 4.3 \cdot 10^{30}$ cm^{-2}s^{-1} is predicted by the code in single IP collision with a tune shift of ξ_x and ξ_y equal to 0.04 and with the machine nominal parameters.

For all the simulations a space charge tune shift parameter of $\xi_x = \xi_y = 0.03$ has been adopted and the DAΦNE nominal beam parameters have been used. No vertical phase advance difference between IPs has been assumed, as it is for the machine. Only the horizontal phase advance difference is optimized.

In the following we describe in more details the luminosity performance for each of these tunes.

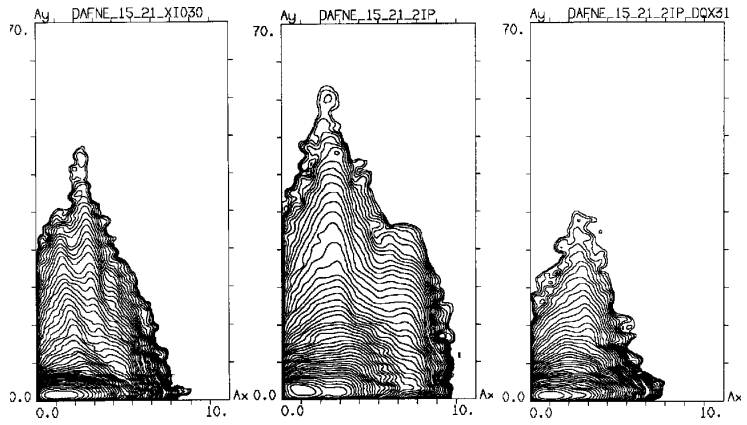

Figure 5.1: Equilibrium density in the space of normalized betatron amplitudes for DAΦNE working point (5.15; 5.21) for the following three cases: (a) 1-IP; (b) 2-IPs and a tune advance difference between them of $\Delta Q_x = 0.24$; (c) 2-IPs and a tune advance difference between them of $\Delta Q_x = 0.31$;

5.2 Studies on the WP (5.15;5.21)

The working point (5.150; 5.210) has been adopted as the nominal one for the *DAY-ONE* commissioning and it has been fully analyzed in the previous Chapter 4. Here I report the results concerning the beam-beam interaction at the two IPs at this point.

Figure 5.1 shows the beam equilibrium distributions for the working point (5.150; 5.210) corresponding to the space charge tune shift parameter of $\xi_x = \xi_y = 0.03$. Figure 5.1 (a) shows the beam distribution for one IP, for which a luminosity of $\mathcal{L} = 2.2 \cdot 10^{30}$ cm^{-2}s^{-1} is predicted with normalized horizontal and vertical beam sizes of $\sigma_x/\sigma_{x0} = 1.08$ and $\sigma_y/\sigma_{y0} = 1.04$, respectively. Figure 5.1 (b) and (c) show the beam behavior for two IPs with different tune advance between them: $\Delta Q_x = 0.24$ corresponds to the *Day-One* experimental situation, while $\Delta Q_x = 0.31$ corresponds to the maximum predicted luminosity by the code, as it can be seen in Figure 5.2. In all the three cases the beam tails are within the dynamic aperture, but it can be observed comparing Figure 5.1 (b) and (c) that not only the luminosity is higher but also the tails result shorter for the case 5.1 (c), even in comparison with the single IP collision shown in Figure 5.1 (a). At $\Delta Q_x = 0.24$ it was experimentally found a 40% reduction of the luminosity per single IP. Simulations give a value near to $30 - 35\%$.

Figure 5.2 shows the dependence of the luminosity (per each IP) calculated with the LIFETRAC code as a function of the horizontal tune advance difference. It

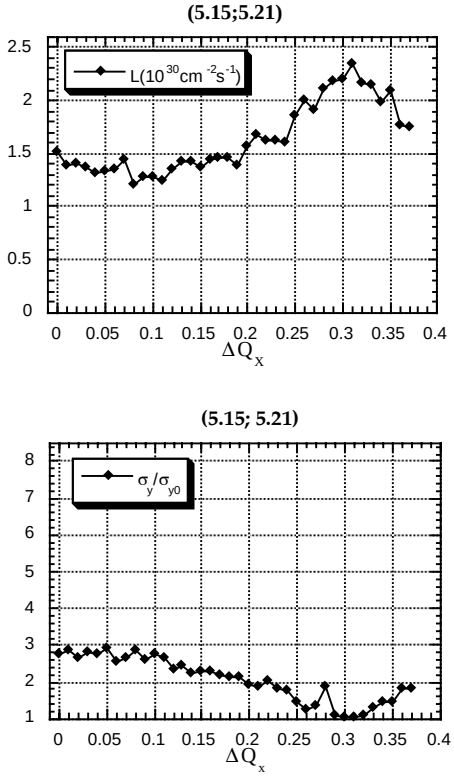

Figure 5.2: Luminosity (above) and normalized vertical beam size (below) as functions of the horizontal tune advance difference for the working point (5.150; 5.210).

appears that the maximum luminosity of $\mathcal{L} = 2.35 \cdot 10^{30}$ cm^{-2}s^{-1} is to be expected for a tune difference of $\Delta Q_x = 0.31$. This means that the phase differences may create new beam-beam resonances but they may also destroy some of the old strong ones. As expected from the luminosity values the vertical size minimum blow-up is reached at $\Delta Q_x = 0.31$ (see Figure 5.2).

The radial size has not been reported since no relevant horizontal blow up has been observed at any variations of the parameter ΔQ_x.

5.3 Studies on the WP (5.16;5.21)

During the commissioning of the machine in the *KLOE-IR* configuration it has been noted that the beam lifetime improves working with a higher radial tune with respect to $Q_x = 5.15$, but always near to it. The beam tails for this working point

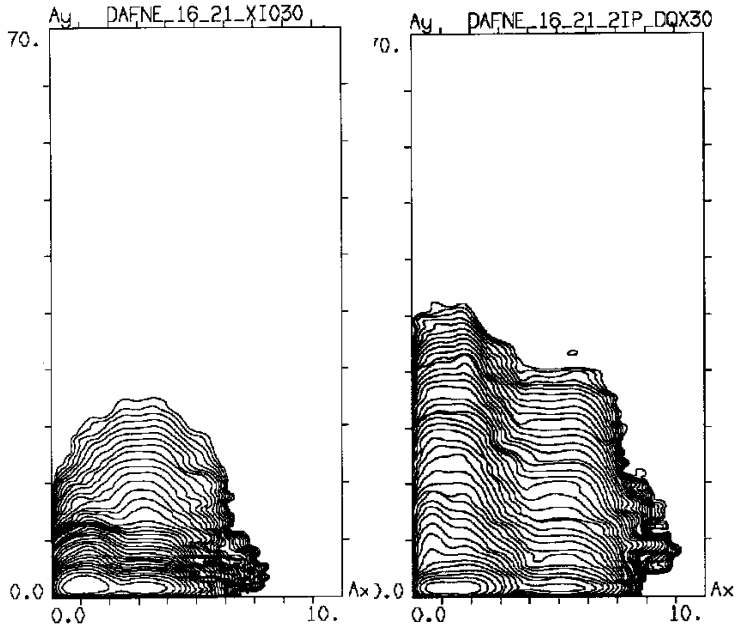

Figure 5.3: Beam distribution tails relative to the tunes (5.16;5.21) (a) for 1-IP and (b) for 2-IPs and a radial tune advance difference between them of $\Delta Q_x = 0.30$.

are shown in Figure 5.3. In Figure 5.3 (a) the beam distribution corresponds to one IP; Figure 5.3 (b) corresponds instead to two IPs with a tune advance difference of $\Delta Q_x = 0.30$ between them being the situation with the maximum predicted luminosity , as it appears from the peak in the above plot of Figure 5.4.

Figure 5.4 shows in fact a rough scan with steps of 0.10 in the horizontal phase difference. As just discussed there is a peak of the luminosity around $\Delta Q_x = 0.30$ and respectively a minimum for the beam sizes (Figure 5.4 below).

The estimated luminosity for this working point with a single IP is $\mathcal{L} = 1.64 \cdot 10^{30}$ cm^{-2}s^{-1} while the maximum luminosity for the two IPs configuration of $\mathcal{L} = 1.8 \cdot 10^{30}$ cm^{-2}s^{-1} is predicted for a radial tune difference of $\Delta Q_x = 0.30$. It must be pointed out that in both cases the core and the tails enlarge horizontally leading to luminosity reduction in comparison to the point (5.150; 5.210) and with two IPs the horizontal tails tend to reach the dynamic aperture.

5.4 Studies on the WP (5.11;5.21)

This working point is close to the sextupole resonance $2Q_x - Q_y = 5$. In fact, while tuning the ring at this point it has been observed a decrease of the dynamic aperture

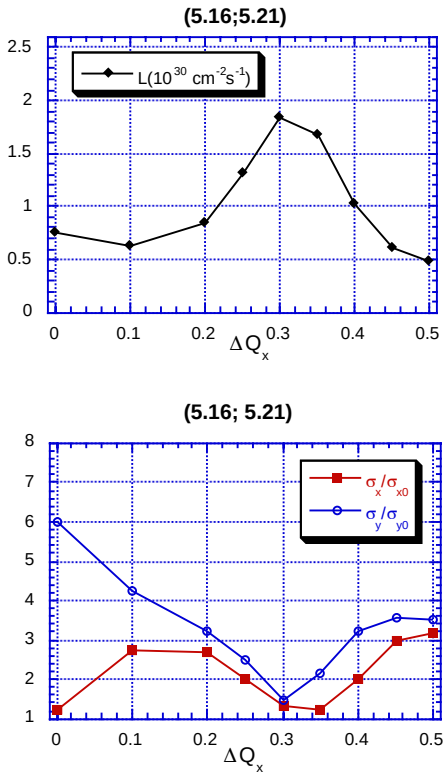

Figure 5.4: Luminosity (above) and normalized vertical and horizontal beam sizes (below) as functions of the horizontal tune advance difference for the working point (5.16;5.21).

and an increase of coupling with the result that the beam was not stable.

Anyway, from the beam-beam point of view, this working point is a good point and it is situated not very far from the actual tune (5.150; 5.210). LIFETRAC predicts a luminosity of $\mathcal{L} = 2.24 \cdot 10^{30}$ cm^{-2}s^{-1} in single IP collision for this WP. The corresponding beam tails are shown in Figure 5.5 (a).

For two IPs the maximum luminosity is expected in the symmetric configuration with no tune difference between the two IPs, as it appears from Figure 5.6. In Figure 5.5 (b) is shown the beam distribution for this symmetric case where the maximum luminosity of $\mathcal{L} = 2.47 \cdot 10^{30}$ cm^{-2}s^{-1} is reached.

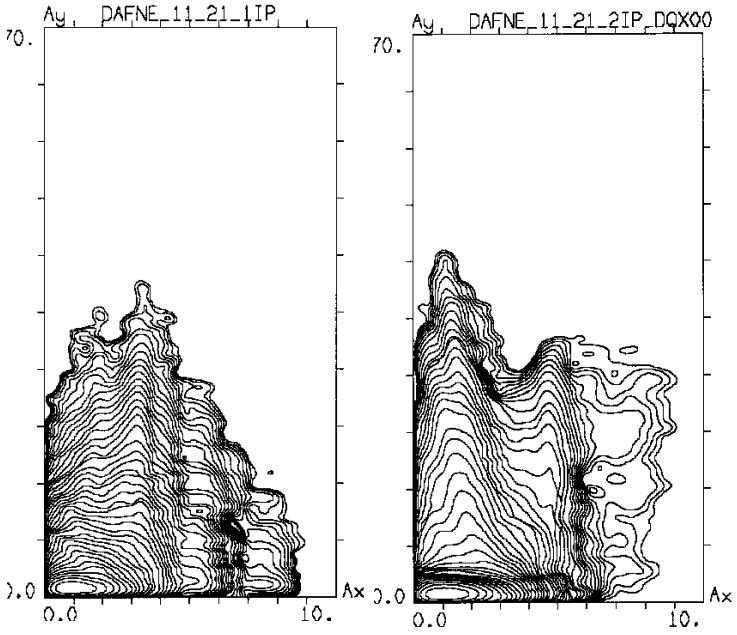

Figure 5.5: Beam tails relative to the tunes (5.11;5.21) (a) for 1-IP and (b) for 2-IPs no radial tune advance difference between them.

5.5 Studies on the WP (5.145;5.09)

This point has been investigated after the indications given by the BBC code. The horizontal tune is very close to the actual one $Q_x = 5.15$, the vertical one is instead lower being closer to the integer.

As for the previous points, Figures 5.7 (a) and (b) show the beam tails for one IP and for two IPs. In the first case a luminosity of $\mathcal{L} = 2.20 \cdot 10^{30}$ cm^{-2}s^{-1} is predicted, in the second one of $\mathcal{L} = 2.40 \cdot 10^{30}$ cm^{-2}s^{-1}. The tails are well within the dynamic aperture in both cases.

As it appears from Figure 5.8 the maximum luminosity is obtained when the phase advance difference is equal to zero, just like the previously discussed case of tunes (5.11; 5.21), but for $\Delta Q_x = 0.1$ the vertical beam size is smaller.

5.6 Studies on the WP (5.10;5.14)

The working point could be a good one for DAΦNE . The beam tails, as Figures 5.9 (a) and (b) show, stay well within the dynamic aperture and the estimated luminosity is as high as for all the other described points: for the 1-IP case is $\mathcal{L} = 2.34 \cdot 10^{30}$ cm^{-2}s^{-1}, for the 2-IPs case is equal to $\mathcal{L} = 2.43 \cdot 10^{30}$ cm^{-2}s^{-1}.

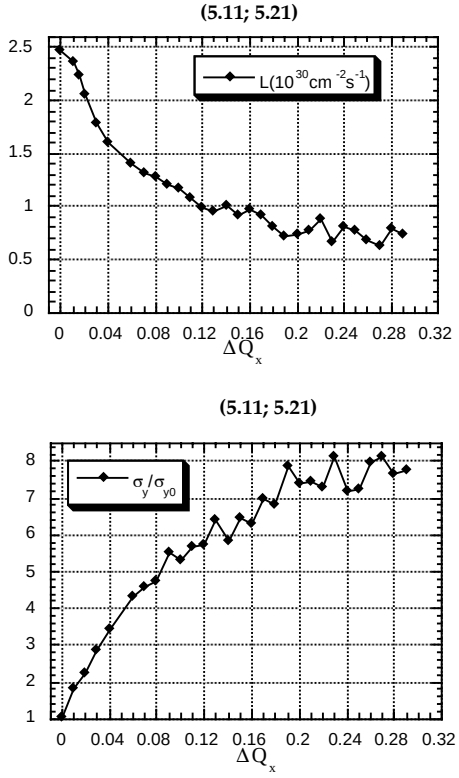

Figure 5.6: Luminosity (above) and normalized vertical beam size (below) as functions of the horizontal tune advance difference for the working point (5.11;5.21).

Moreover for these betatron tunes, as we can notice from Figure 5.10, the luminosity remains almost unchanged around the value of $2 \cdot 10^{30}$ cm^{-2}s^{-1} for different tune advances. Anyway the highest value corresponds to the symmetric case with equal phase advances. In Figure 5.10 we observe that the normalized vertical beam size increases together with the decrease of the luminosity , but the luminosity reduction does not seem to be big even for $\sigma_y/\sigma_{y0} \approx 3.5$.

In this case the simulation with the design tune shift value of $\xi_x = \xi_y = 0.04$ for the single IP has been carried out. The expected luminosity results $\mathcal{L} = 3.50 \cdot 10^{30}$ cm^{-2}s^{-1} with normalized beam sizes of $\sigma_x/\sigma_{x0} = 1.01$ and $\sigma_y/\sigma_{y0} = 2.07$, that is there is a vertical blow up but the luminosity value is quite close to the nominal one of $\mathcal{L} = 4.3 \cdot 10^{30}$ cm^{-2}s^{-1}.

Cubic nonlinearities have been added to the simulations for 1-IP and 2-IPs with tune shift of $\xi_x = \xi_y = 0.03$. The lifetime is not reduced even if there is an

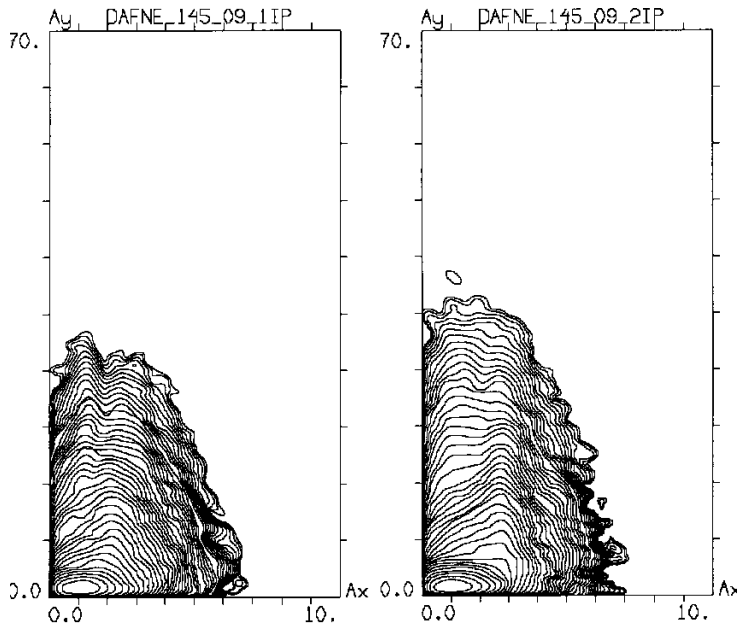

Figure 5.7: Beam tails relative to the tunes (5.145;5.09) (a) for 1-IP and (b) for 2-IPs and no radial tune advance difference between them.

enlargement of the beam tails. For the 1-IP case simulations give a luminosity of $\mathcal{L} = 2.25 \cdot 10^{30}$ cm^{-2}s^{-1} and beam sizes $\sigma_x/\sigma_{x0} = 0.99$ and $\sigma_y/\sigma_{y0} = 1.60$. For the 2-IPs case the expected values are: $\mathcal{L} = 2.42 \cdot 10^{30}$ cm^{-2}s^{-1} and $\sigma_x/\sigma_{x0} = 0.94$ and $\sigma_y/\sigma_{y0} = 1.18$.

5.7 Studies on the WP (5.52;5.59)

This working point is very close to the half integer, so it would be very desirable to tune the machine at this point, in order to have higher allowable beam-beam tune shifts and luminosity values.

However, since the collider nonlinear behavior has not been completely studied yet, it is difficult to say a priori whether the working point will fall within a stop band of the half integer resonance. Nevertheless beam-beam simulations for these tunes may result useful in future, when the machine nonlinearities are studied and corrected for example by sextupoles adjustments. Figure 5.11 shows the beam distribution tails in the three following cases: (a) single IP; (b) two symmetric IPs and (c) a tune advance difference between the two IPs of $\Delta Q_x = 0.30$. The beam tails do not enlarge much and the beam appears quite stable in all the three cases. For the 1-IP case the expected luminosity is of $\mathcal{L} = 2.5 \cdot 10^{30}$ cm^{-2}s^{-1}; for the symmetric

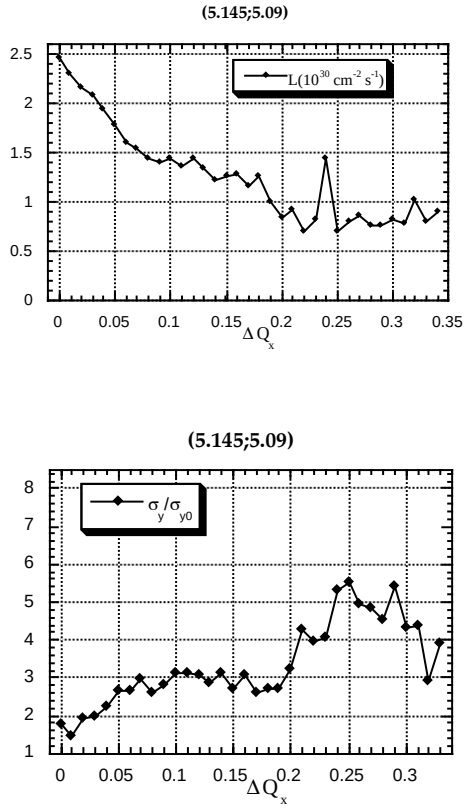

Figure 5.8: Luminosity (above) and normalized vertical beam size (below) as functions of the horizontal tune advance difference for the working point (5.145;5.09).

case is of $\mathcal{L} = 1.9 \cdot 10^{30}$ cm^{-2}s^{-1} and for a tune difference between the two IPs of $\Delta Q_x = 0.30$ the very similar value of $\mathcal{L} = 1.84 \cdot 10^{30}$ cm^{-2}s^{-1} is predicted.

Figure 5.12 shows that moving the phase advance between the two IPs from $\Delta Q_x = 0$ to $\Delta Q_x \approx 0.3$ the luminosity values do not vary much from values slightly below $2 \cdot 10^{30}$ cm^{-2}s^{-1}. The case of a single IP has been simulated also with the nominal tune shift parameter and the given luminosity is just the nominal value $\mathcal{L} = 4.3 \cdot 10^{30}$ cm^{-2}s^{-1}.

5.8 Conclusions

Table 5.1 summarizes the results of the study presented in this chapter. For the considered working points the estimated luminosity for one IP and for two IPs collision is given (second and third columns respectively). In the case of two IPs it

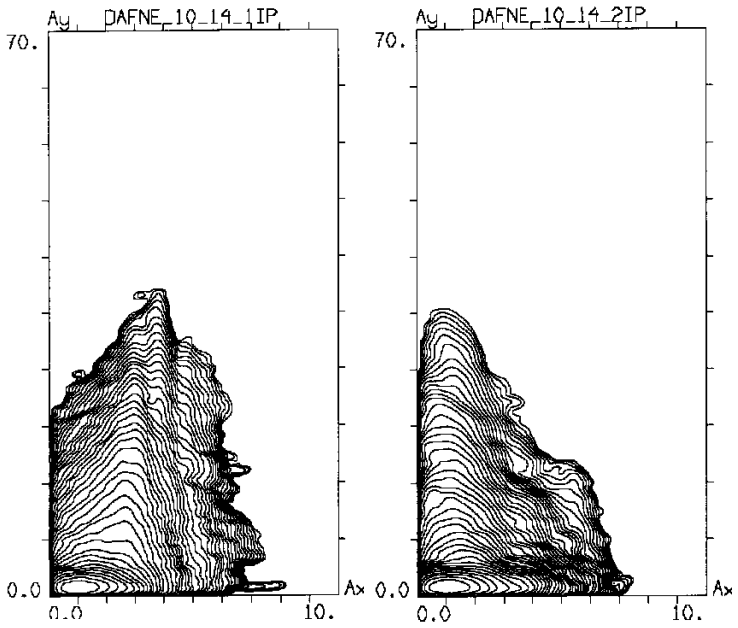

Figure 5.9: Beam distribution tails relative to the tunes (5.10;5.14) (a) for 1-IP and (b) for 2-IPs and no radial tune advance difference between them.

is also shown the horizontal phase advance between the IPs where the maximum luminosity is achieved. The normalized beam size blow up due to the beam-beam interaction is reported in the vertical and horizontal plane for the 2-IPs case (fourth and fifth columns respectively). To conclude:

1. The best point for the two IPs is (5.150; 5.210) since it has high luminosity and short tails (even shorter than in the case of a single IP). Besides $\Delta Q_x = 0.31$ between the IPs is not far from the actual one of $\Delta Q_x = 0.24$. So it will not require major lattice modifications.

2. The working point (5.16;5.21) provides lower luminosities but, even more important, long horizontal tails reaching the machine dynamic aperture in case of two IPs can be observed. For this reason we expect short lifetime for working point .

3. (5.11;5.21) seems to give good luminosity in both 1-IP and 2-IPs collisions. However this point is close to the resonance $2Q_x - Q_y = 5$ which limits the dynamic aperture and makes more difficult the coupling correction.

4. (5.145;5.09) is the point which is worth to try: the luminosity is good and the tails are well within the dynamic apertures. The only disadvantage is that

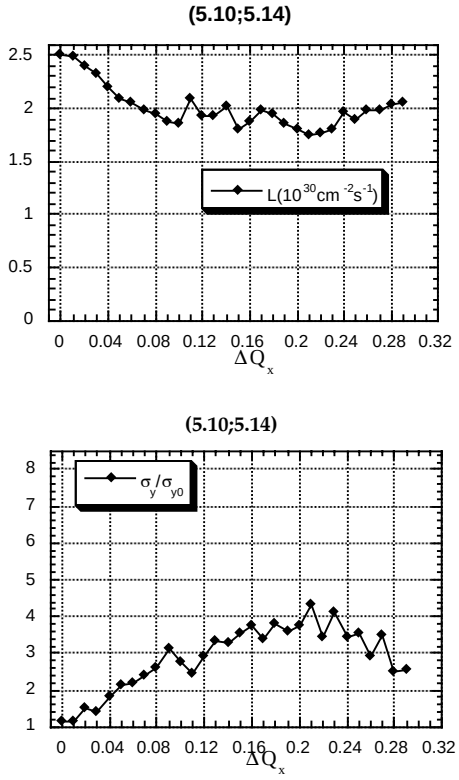

Figure 5.10: Luminosity (above) and normalized vertical beam size (below) as functions of the horizontal tune advance difference for the working point (5.10;5.14).

the maximum luminosity is reached with the phase advance difference close to zero and some lattice modifications are necessary to fulfill this condition.

5. The same conclusion as the previous one can be applied to the point (5.10;5.14).

6. The point (5.52;5.59) is good for single IP collisions. Moreover this is one of the few points on the tunes diagram where the design luminosity of $\mathcal{L} = 4.3 \cdot 10^{30}$ cm^{-2}s^{-1} is achieved with the beam-beam code. However for the optimal ΔQ_x in this case a 70% blow up is observed in the code output when colliding with two IPs. It can be underlined that being close to the half integer the point can be a challenge for the machine optics.

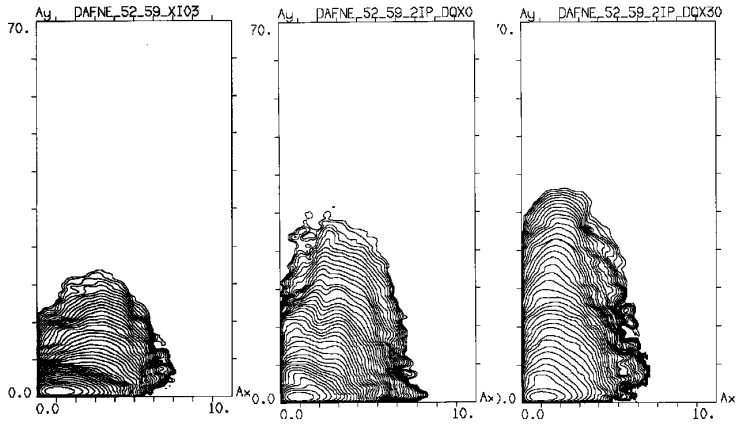

Figure 5.11: Beam distribution tails relative to the tunes (5.52;5.59) (a) for 1-IP and (b) for 2-IPs and no radial tune advance difference between them and (c) for a tune difference of $\Delta Q_x = 0.30$.

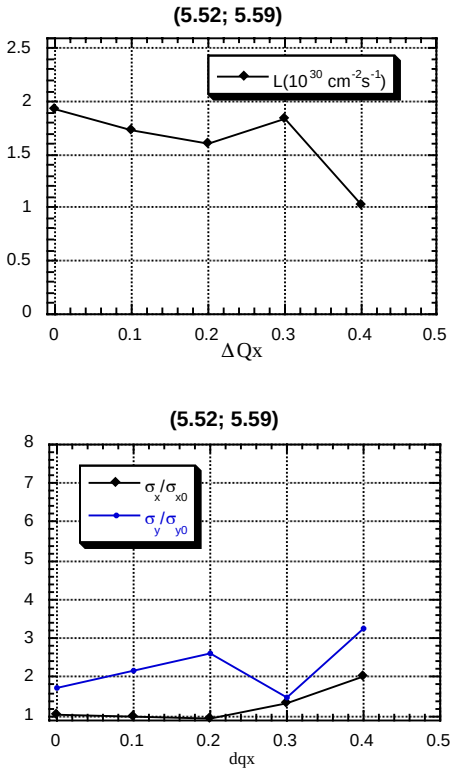

Figure 5.12: Luminosity (above) and normalized vertical and horizontal beam sizes (below) as functions of the horizontal tune advance difference for the working point (5.52;5.59).

Table 5.1: Predicted values of luminosity with 1-IP and with 2-IPs, for the best ΔQ_x between them, and normalized beam sizes for each working point .

WP	$\mathcal{L}_{2IP}$ (10^{30} cm^{-2}s^{-1})	$\mathcal{L}_{1IP}$ (10^{30} cm^{-2}s^{-1})	σ_y/σ_{y0} (2IP)	σ_x/σ_{x0} (2IP)
(5.150; 5.210) $\Delta Q_x = 0.31$	2.24	2.20	1.05	1.12
(5.16;5.21) $\Delta Q_x = 0.30$	1.80	1.64	1.49	1.33
(5.11;5.21) $\Delta Q_x = 0$	2.47	2.24	1.03	0.94
(5.145;5.21) $\Delta Q_x = 0.01$	2.37	2.20	1.44	1.00
(5.10;5.14) $\Delta Q_x = 0.01$	2.43	2.34	1.14	0.94
(5.52;5.59) $\Delta Q_x = 0$	1.90	2.50	1.71	1.03

Chapter 6

Experimental Results

This chapter has been divided in two parts, corresponding to the two commissioning phases: the first one called *DAY-ONE* is before KLOE installation and the second one is after KLOE installation. Machine performance and most significant results are presented for the two phases of commissioning with particular attention to the latest measurements.

6.1 Commissioning at the DAY-ONE

In the *DAY-ONE* commissioning phase the goal has been to tune the machine for collisions and optimize the single bunch luminosity before KLOE's installation in order that with the *KLOE-IR* configuration only the perturbation introduced by the KLOE solenoidal magnet should be corrected and the machine could be ready for operation [37]. The DAΦNE performance achieved during the first phase of operation for single beam and colliding beams with particular attention to the beam-beam performance is reported in the following.

During this first phase electron and positron currents larger than twice the design value have been stored separately with no instabilities, that is 110 mA have been reached where the design value is 44 mA. Moreover, the beams parameters (some are for example emittance, coupling, beam sizes, optical functions, chromaticity) have been measured and well agree with design values derived from the theoretical models. The chosen working point is (5.15;5.21) that is far from integers and from sextupolar resonances, the machine is not too sensible to closed orbit distortion, the dynamic aperture is good enough and also lifetime. A coupling of the order of $\kappa \sim .002$ has been obtained, much smaller than its design value $\kappa = .01$ also with

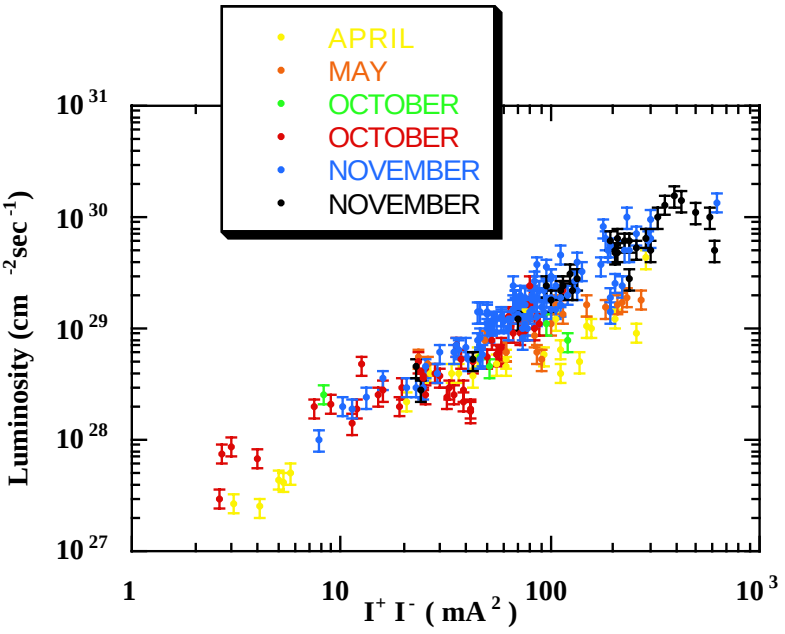

Figure 6.1: Luminosity versus the product of the positron and electron currents.

sextupoles on. The maximum single bunch luminosity obtained is $1.6 \cdot 10^{30}\mathrm{cm}^{-2}\mathrm{s}^{-1}$ with $I^+ = 19$ mA and $I^- = 21$ mA. Assuming equal tune shifts for the two beams this corresponds to $\xi_y \sim .03$, which is in a good agreement with the beam-beam simulations with one interaction point at this working point. Using the RF phase jump procedure a luminosity of the order of $10^{31}\mathrm{cm}^{-2}\mathrm{s}^{-1}$ has been obtained with 13 positron and 13 electron bunches. A short time has been dedicated to multibunch luminosity measurements with two interaction points. In this case there is a luminosity degradation of the order of $\sim 40\%$ for each IP, in agreement with simulations.

6.2 Commissioning after KLOE installation

The KLOE experiment has been installed in winter 1999. The main issue after the KLOE installation was to reproduce at least the same luminosity reached before, while increasing the beam lifetime. In the first month of operation the machine energy has been tuned to the Φ-resonance. Figure 6.2 shows the Φ-resonance line shape obtained by the KLOE experiment.

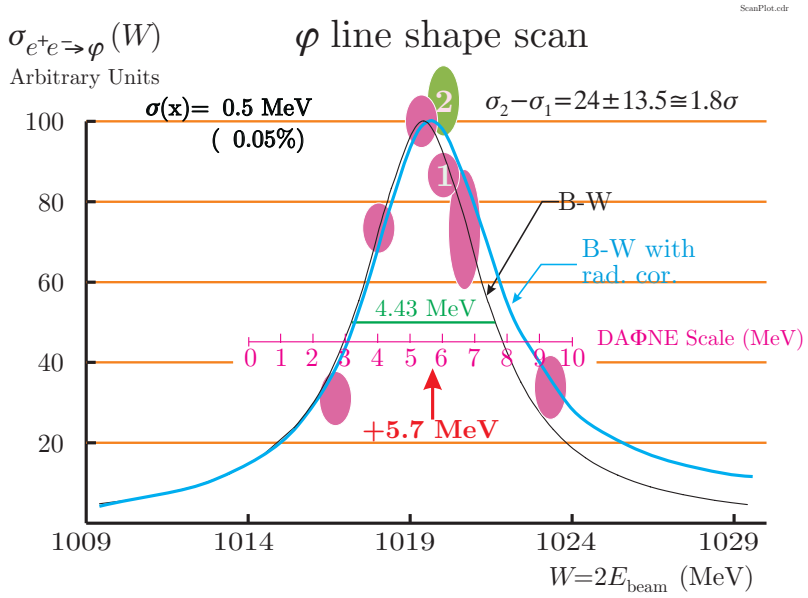

Figure 6.2: Φ-resonance line shape obtained by the KLOE experiment

6.2.1 KLOE Solenoid Compensation

The high integrated field of KLOE solenoid (2.4 Tm) is a strong perturbation for the low energy DAΦNE beam. It rotates the beam by about 45° in the transverse plane and it is the main source of beam coupling. A compensation scheme has been adopted to cancel this coupling. This scheme requires two compensating solenoids symmetrically placed with respect to the main one and a rotation of the low-β triplet quadrupoles.

The rotation angles of the quadrupoles in the triplets with respect to each other have been set first, then the two triplets as a whole have been aligned with respect to their mechanical supports. After the installation each triplet can be moved rigidly with five degrees of freedom -horizontal and vertical angle, displacement and rotation angle. The alignment of each triplet has been measured looking at four reference points. In the horizontal plane the alignment is quite satisfactory, the vertical displacement of one triplet and the rotation angle of both would need instead further correction. At this stage the effects of these errors are compensated by adjusting the field of the detector and of the compensating solenoids and also with eight skew quadrupoles in each ring. The minimum coupling measured after the adjustment of the fields of KLOE and of the compensating solenoids is $\kappa = 0.008$ for the positron beam. For the electron ring two skew quadrupoles have also been used and a coupling of $\kappa \approx 0.01$ has been obtained.

6.2.2 Beam-Beam Measurements

In September 1999 beam-beam measurements have been done in order to optimize the luminosity and the lifetime [38]. Luminosity depends on emittance, coupling and on the following parameters at IP: β-functions, vertical waist position, longitudinal IP position, transverse tilt angle and horizontal crossing angle. Coupling has been adjusted as it is described in the latter Section and in normal working conditions is $\kappa(e^+) \sim 1.5\%$ for positrons and $\kappa(e^-) \sim 1\%$ for electrons. An estimate of the coupling factor can be derived from the roundness $R = \sigma_y / \sigma_x$ measured at the Synchrotron Light Monitor (SLM). Emittance is set by the chosen lattice and it is about half of its nominal value that is $\varepsilon(e^+) = 0.5 \cdot 10^{-6}$ m rad for positrons and $\varepsilon(e^-) = 0.7 \cdot 10^{-6}$ m rad for electrons.

In order to achieve high luminosity the longitudinal and transverse positions of the two beams must be adjusted to provide maximum overlap at the IP. Moreover, the waists of the vertical β-functions should be the same for the two rings and coincide with the IP.

Longitudinal and transverse overlap of colliding beams at the nominal IP have to be obtained simultaneously. In the *DAY-ONE* configuration a seventh BPM in each IR was installed at the IP position. This simplified beam superposition and horizontal β-function measurements at the IP, thanks to the IP quadrupole. This BPM was removed before KLOE detector roll-in. At present the luminosity monitor is used to measure the effective cross section of the interacting beams. The measurements are performed by scanning the position of one beam with respect to the other and measuring the luminosity value on the monitor. All these measurements have to be done with weak beams (current of about $2-3$ mA) to avoid beam-beam blow up. With this technique it is possible to determine the vertical and horizontal beam size at the IP and in particular the maximum luminosity is obtained by optimizing the transverse overlap. The vertical overlap is the most effective one being the beams flat. Figure 6.3 shows the ratio between the measured luminosity and its maximum value as a function of the vertical position of one beam with respect to the other one. A nice Gaussian shape centered in zero with a Σ_y ranging between 35 and 50 μm can be noticed. This shape is the convolution of the two beams distributions. The vertical sigma of one beam σ_y can be obtained by assuming equal size beam distribution being $\Sigma_y = \sqrt{2}\,\sigma_y$.

The longitudinal overlap of colliding bunches at the nominal IP has been synchronized by monitoring the distance between the combined signals of the two beams

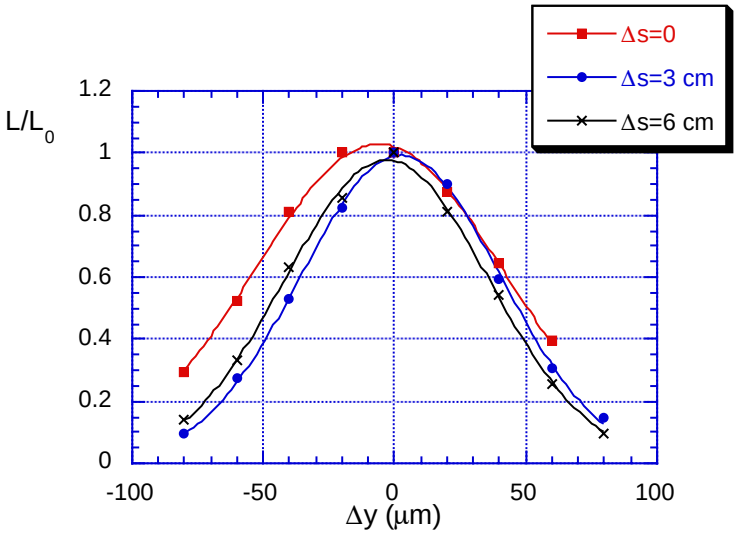

Figure 6.3: Vertical luminosity scan for different RF phases.

on two sets of symmetric BPMs on either side of the IP. A good longitudinal timing has been achieved by varying the RF phase of one of the two beams in order to minimize the vertical sigma σ_y or equivalently maximize the luminosity . Figure 6.4 shows the effective vertical sigma Σ_y as a function of the RF phase. 0.1 V of the RF phase corresponds to 1 cm shift of the IP along the longitudinal direction. The minimum corresponds to the best longitudinal overlapping.

Measurements with two weak beams were done to check the dependence of luminosity on the relative transverse tilt of the two beams. The positron tilt angle has been changed by using a skew quadrupole near the SLM where it is monitored. Together with the tilt angle also roundness is varied with this procedure so that the largest effect on the luminosity is due to the roundness change. The expected and measured luminosities are shown Figure 6.5 as a function of the positron tilt angle measured at the SLM. The expected luminosity is calculated taking into account only the change of the coupling as measured at the SLM. The difference between the measured and expected value can be interpreted as due to different tilt between bunches. Since the difference in luminosity is within 30% the relative tilt angle at the IP must be small. On the other hand the relative tilt angle at the IP cannot be monitored and the extrapolation from the SLM is not an easy task. Another way to approach the problem is via the beam-beam simulations. Figure 6.6 (a) shows the ratio between the luminosity from the simulation and the nominal value with no tilt angle as a function of the strong beam's current for a tilt angle between the beams of 1 degree. It can be seen that the decrease in luminosity is about 30% at

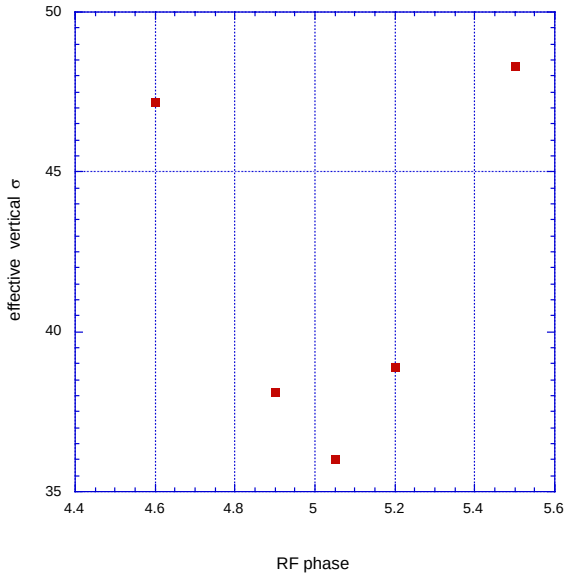

Figure 6.4: Effective vertical beam size vs RF phase.

low current. This confirms that in the previous experiment (see Figure 6.5) the tilt angle at the IP cannot exceed values of about 1 degree.

Higher decrease of luminosity due to the tilt angle can be observed for larger strong beam's current (as shown in Figure 6.6 (a)). It is due to the vertical beam-beam blow up shown in Figure 6.6 (b) where is plotted the weak beam vertical size normalized to its unperturbed value as a function of the strong beam's current. This weak beam behavior has been confirmed experimentally. Figure 6.7 shows the results of a dedicated weak-strong run where a weak electron beam of 4.5 mA collides with a strong positron beam of 9 mA. The variation of the roundness R_+ of the strong beam is due to the method used to vary the tilt angle at IP as said before. The important thing to be noticed is that in correspondence of the decrease of luminosity is the weak beam vertical blow up and viceversa. Comparing the weak beam roundness R_- in Figure 6.7 with the simulation results in Figure 6.6 (b) for a $\xi \sim 0.015$ the measured blow up is in good agreement with simulations.

For the best overlap condition usually obtained in run condition a vertical beam size of $\sigma_y = (19.0 \pm 0.4)$ μm has been measured in good agreement with the theoretical expectation of $\sigma_y = 18.6$ μm calculated with an emittance of $0.5 \cdot 10^{-6}$ m rad, a coupling of $\kappa = 1.5\%$ and $\beta_y^* = 4.5$ cm.

The measured luminosities are close to the expected values at low current. The maximum single bunch luminosity reached is $\mathcal{L}_{SB} = 3.3 \cdot 10^{29}$ cm^{-2}s^{-1} obtained with

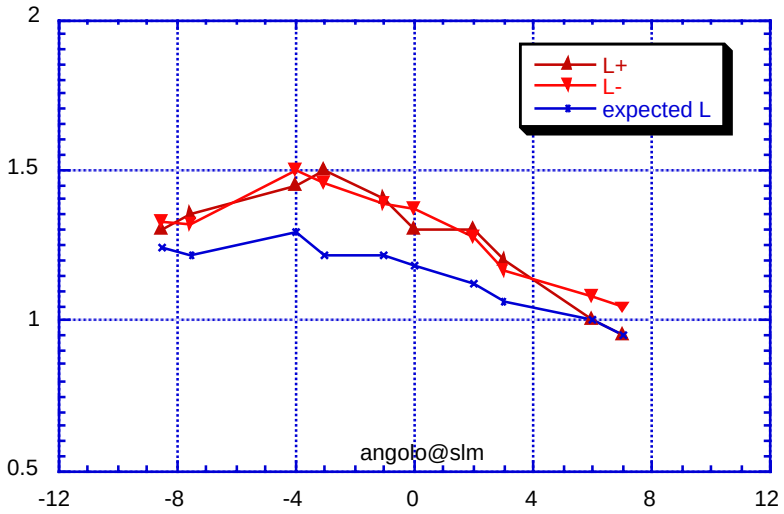

Figure 6.5: Luminosity expected and measured versus the positron rotation angle.

currents $I_- = 18$ mA and $I_+ = 12$ mA and lifetime of about 2000 s. Different sets of current were used to increase this value, but the beam blow-up prevented any increase of the maximum luminosity . Values between 2.5 and $3 \cdot 10^{29}$ cm^{-2}s^{-1} with good beam lifetimes have been obtained.

The behavior of one beam roundness and lifetime as a function of the current of the opposite beam has been analyzed for different working points (see Figure 6.8). The roundness is expected to increase with current above a particular threshold that depends on the chosen working point due to the vertical beam-beam blow up. The Figure 6.8 shows that the point (5.16;5.21) exhibits the highest current threshold in the roundness behavior and the slowest decay of the lifetime in the scanned area near the working point (5.150; 5.210). The current threshold that has been found experimentally is at about 10 mA for each bunch corresponding to a luminosity of $\mathcal{L} = 1.5 \cdot 10^{29}$cm^{-2}s^{-1}.

6.2.3 Multibunch Operation

Multibunch luminosity is given by

$$\mathcal{L} = f n_b \cdot \frac{N_- N_+}{4\pi \sqrt{\frac{\sigma_{y-}^2 + \sigma_{y+}^2}{2}} \sqrt{\frac{\sigma_{x-}^2 + \sigma_{x+}^2}{2}}} \tag{6.1}$$

directly derived from the single bunch luminosity expression in Equation B.6 where n_b is the number of colliding bunches. In terms of the total number of particles the

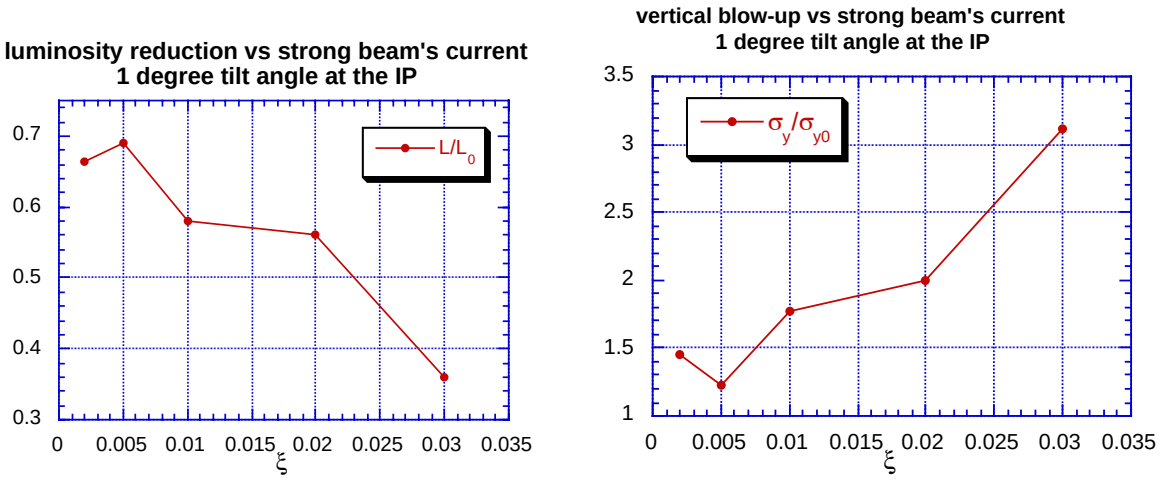

(a) (b)

Figure 6.6: (a) Luminosity reduction vs the strong beam's current; (b) Weak beam vertical blow up vs the strong beam's current in case of a tilt angle of 1 degree at the IP.

previous expression can be written as:

$$\mathcal{L} = \frac{f}{n_b} \frac{N_{t-} N_{t+}}{4\pi \sqrt{\frac{\sigma_{y-}^2 + \sigma_{y+}^2}{2}} \sqrt{\frac{\sigma_{x-}^2 + \sigma_{x+}^2}{2}}} \tag{6.2}$$

where $N_{t\pm} = n_b N_{\pm}$ and the bunches are assumed to be all equal. From this formula it can be easily seen that in order to have the maximum possible luminosity the choice on the number of bunches must be done carefully. It is desirable to have the maximum possible current per bunch rather than increase the number of bunches.

DAΦNE operates in multibunch mode for the physics runs with a number of bunches ranging from 30 to 50. In these runs an integrated luminosity of about 3 pb^{-1} has been collected by the KLOE experiment in about one month. Figure 6.9 shows an example of a typical run. From the top side of the figure may be seen that the two beams are refilled during collision. This operation is called *topping-up* and it helps to increase the integrated luminosity . The initial peak luminosity is about $3 \cdot 10^{30} \text{cm}^{-2}\text{s}^{-1}$ with currents of about 250 mA.

During multibunch operation a technique has been found to stabilize the beams in collision. This works thanks to the Landau beam-beam damping. On the top of Figure 6.10 is shown the injected electron beam out of collision with a high vertical instability due to the sextupoles used for injection. As the second beam is injected and brought to collision the electron beam instability is damped.

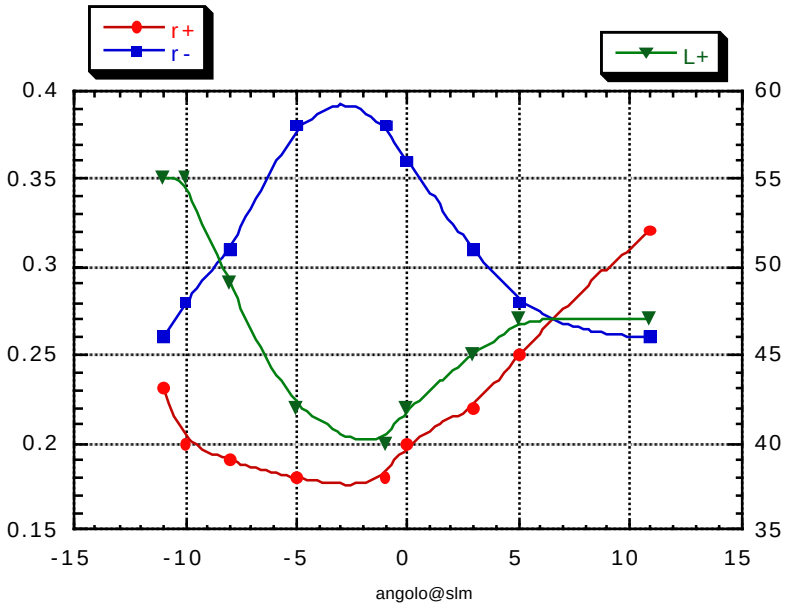

Figure 6.7: Luminosity vs positron rotation angle together with the electron and positron roundness simultaneously measured.

6.3 Coherent Beam-Beam Tune Shift Measurement

The beam-beam interaction excites coherent bunch oscillations, in which each bunch behaves like a rigid distribution of particles, while the center-of-mass of the bunches oscillate. The center-of-mass coordinates of the two bunches move like weakly coupled oscillators. This system exhibits two normal modes.
The first mode gives the eigenfrequency in the undisturbed betatron frequency ($0-mode$) and the second mode gives the perturbed one ($\pi-mode$) [39]. In the $0-mode$ the two bunches move up and down together in phase at the interaction points. The bunches do not feel the beam-beam forces and the mode frequency is equal to the unperturbed betatron frequency. This mode is always stable.
In the $\pi-mode$ the two bunches move out of phase. In the linear approximation of the beam-beam force the tune shift experienced by the bunch center would be exactly ξ. However the beam-beam force is highly nonlinear and since the force gets weaker with distance only the central part of the beam will oscillate coherently while the outer part does not move (see Section 2.10). The complete calculation for the center-of-mass motion can be found in [40]. For DAΦNE the eigenvalue is about 1.33ξ.

This effect can be used to measure the beam-beam tune shift ξ by exciting with white noise the beam and looking at the spectrum analyzer at the resonant frequen-

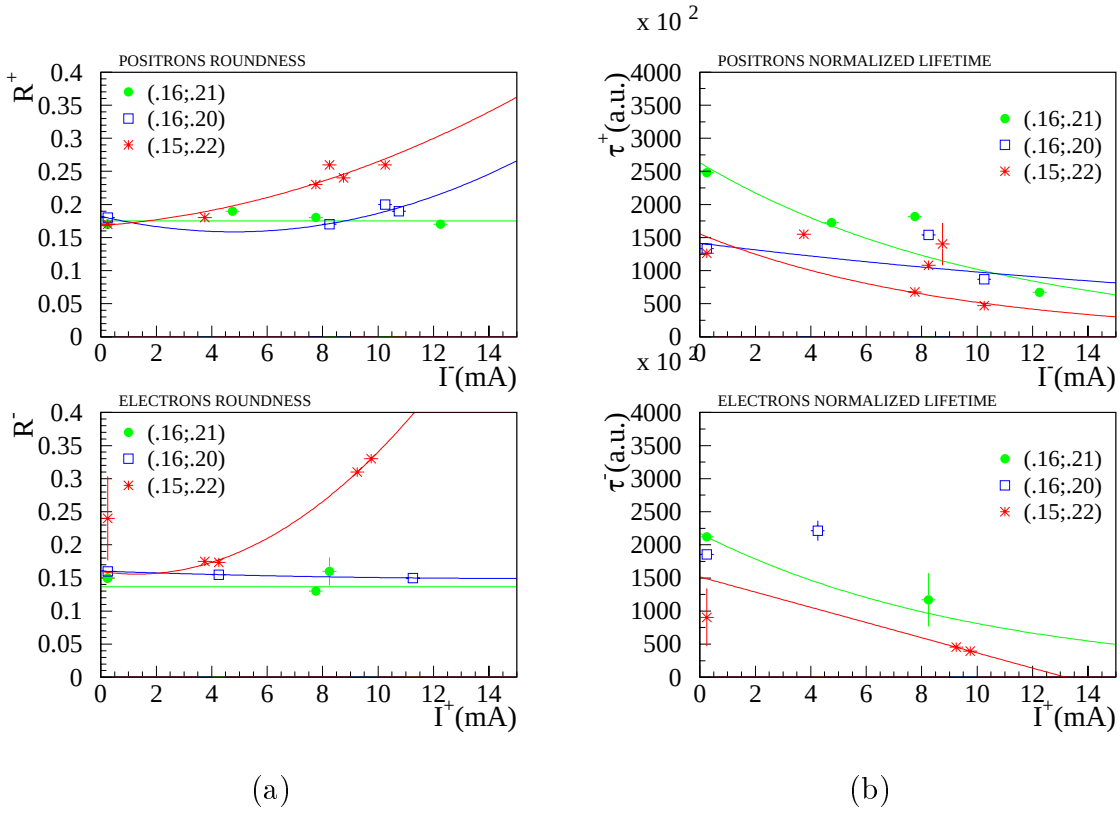

(a) (b)

Figure 6.8: (a) e^+ (e^-) roundness and (b) e^+ (e^-) lifetime normalized on the ratio between the beam current and roundness vs the opposite beam current for different working points.

cies. Figure 6.11 shows an example of coherent beam-beam tune split measurement.

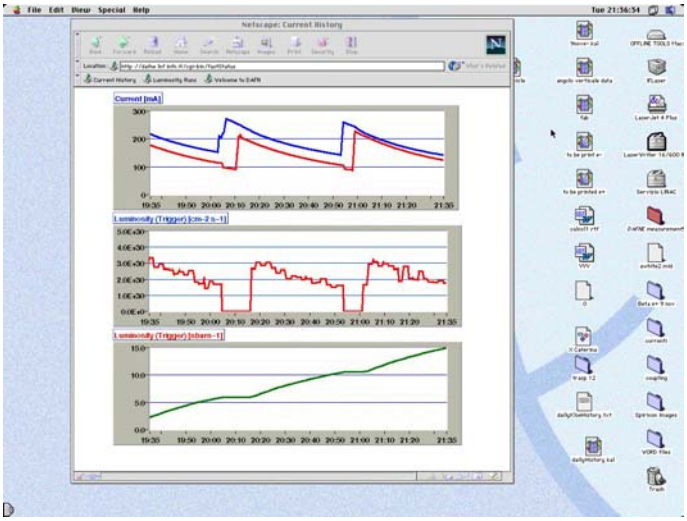

Figure 6.9: Luminosity monitor for a typical multibunch (40+40 bunches) mode run. Topping up is visible on the top of Figure.

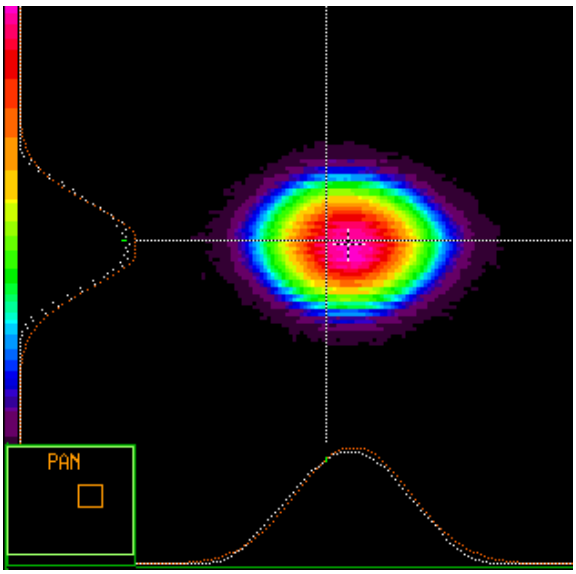

Ie-= 250mA
Ie+= 0 mA

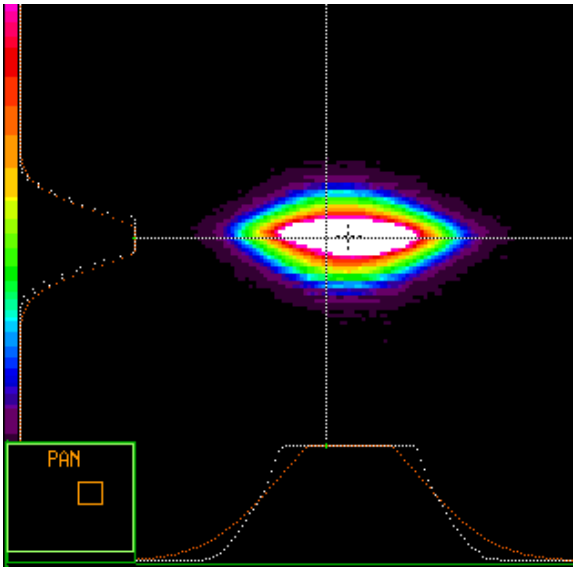

Ie-= 250mA
Ie+= 80 mA

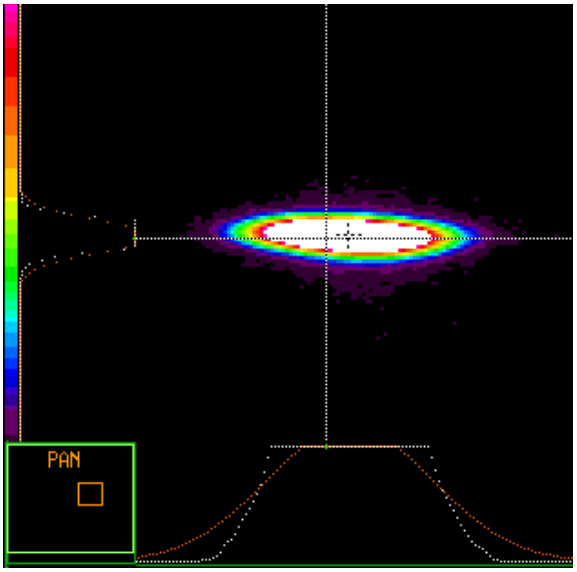

Ie-= 250mA
Ie+= 200mA

Figure 6.10: Beam-Beam damping in multibunch operation.

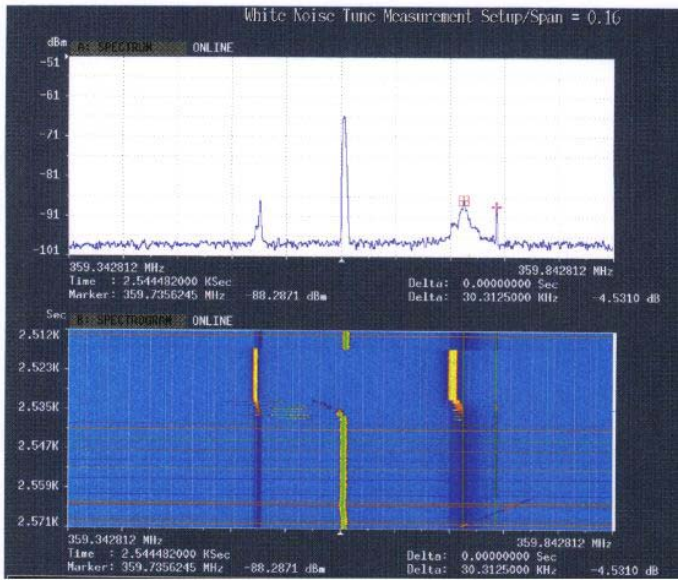

Figure 6.11: Example of coherent tune shift measurement.

Appendix A

Kicks on the transverse axes

It is shown here that the radial beam-beam kick:

$$\Delta x' = -\frac{4Nr_e}{\gamma\sqrt{2(\sigma_x^2-\sigma_y^2)}}\int_r^1 a\ e^{a^2(t^2-1)+b^2(1-\frac{1}{t^2})}dt \tag{A.1}$$

where

$$r = \sigma_y/\sigma_x; \qquad a = \frac{x}{\sqrt{2(\sigma_x^2-\sigma_y^2)}}; \qquad \text{and} \qquad \mathrm{b} = \frac{\mathrm{y}}{\sqrt{2(\sigma_\mathrm{x}^2-\sigma_\mathrm{y}^2)}}$$

in y=0 can be written as:

$$\Delta x' = -\frac{4Nr_e}{\gamma\sqrt{2(\sigma_x^2-\sigma_y^2)}}\Big[F_D\Big(\frac{x}{\sqrt{2(\sigma_x^2-\sigma_y^2)}}\Big) - e^{-\frac{x^2}{2\sigma_x^2}}\cdot F_D\Big(\frac{x}{\sqrt{2(\sigma_x^2-\sigma_y^2)}}\cdot\frac{\sigma_y}{\sigma_x}\Big)\Big] \tag{A.2}$$

where F_D is the Dawson function defined by:

$$F_D(x) = e^{-x^2}\int_0^x e^{t^2}dt.$$

For y=0 b is equal to zero and Equation A.1 becomes:

$$\Delta x' = -\frac{4Nr_e}{\gamma\sqrt{2(\sigma_x^2-\sigma_y^2)}}\int_r^1 a\ e^{a^2(t^2-1)}dt. \tag{A.3}$$

The latter integral can be written as

$$\int_r^1 a\ e^{a^2(t^2-1)}dt = a\ e^{-a^2}\int_r^1 e^{a^2t^2}dt.$$

With the substitution z=at the integral becomes

$$e^{-a^2}\int_{ar}^{a} e^{z^2}dz = e^{-a^2}\Big[\int_{ar}^{0} e^{z^2}dz + \int_0^a e^{z^2}dz\Big]$$

that is

$$e^{-a^2}\Big[\int_0^a e^{z^2}dz - \int_0^{ar} e^{z^2}dz\Big]$$

which is equal to

$$e^{-a^2}\int_0^a e^{z^2}dz - e^{-a^2(r^2-1)}e^{-a^2r^2}\int_0^{ar} e^{z^2}dz$$

just equal to

$$F_D(a) - e^{-a^2(r^2-1)}F_D(ar).$$

Substituting a and r:

$$F_D\Big(\frac{x}{\sqrt{2(\sigma_x^2-\sigma_y^2)}}\Big) - e^{-\frac{x^2}{2\sigma_x^2}}\cdot F_D\Big(\frac{x}{\sqrt{2(\sigma_x^2-\sigma_y^2)}}\cdot\frac{\sigma_y}{\sigma_x}\Big)$$

so that:

$$\Delta x' = -\frac{4Nr_e}{\gamma\sqrt{2(\sigma_x^2-\sigma_y^2)}}\Big[F_D\Big(\frac{x}{\sqrt{2(\sigma_x^2-\sigma_y^2)}}\Big) - e^{-\frac{x^2}{2\sigma_x^2}}\cdot F_D\Big(\frac{x}{\sqrt{2(\sigma_x^2-\sigma_y^2)}}\cdot\frac{\sigma_y}{\sigma_x}\Big)\Big]. \quad (A.4)$$

Analogously it is shown that the vertical beam-beam kick

$$\Delta y' = -\frac{4Nr_e}{\gamma\sqrt{2(\sigma_x^2-\sigma_y^2)}}\int_r^1 \frac{b}{t^2}exp[a^2(t^2-1)+b^2(1-\frac{1}{t^2})]dt \quad (A.5)$$

in x=0 can be written as:

$$\Delta y' = -\frac{4Nr_e e^{b^2}}{\gamma\sigma_x\sqrt{2(1-r^2)}}\frac{\sqrt{\pi}}{2}\Big[erf\Big(\frac{y}{\sigma_y\sqrt{2(1-r^2)}}\Big) - erf\Big(\frac{y}{\sigma_x\sqrt{2(1-r^2)}}\Big)\Big] \quad (A.6)$$

where erf(x) is the error function defined by:

$$erf(x) = \frac{2}{\sqrt{\pi}}\int_0^x e^{-t^2}dt.$$

For x=0 a is equal to zero and Equation A.5 becomes

$$\Delta y' = -\frac{4Nr_e}{\gamma\sqrt{2(\sigma_x^2-\sigma_y^2)}}\int_r^1 \frac{b}{t^2}e^{b^2(1-\frac{1}{t^2})}dt. \quad (A.7)$$

Changing the integration variable t in q=1/t the latter integral becomes:

$$b\ e^{b^2}\int_1^{1/r} e^{-b^2q^2}dq$$

Changing the integration variable q in z=bq :

$$e^{b^2}\int_b^{b/r} e^{-z^2}dz = e^{b^2}\Big[\int_b^0 e^{-z^2}dz + \int_0^{b/r} e^{-z^2}dz\Big]$$

that is

$$e^{b^2}\Big[\int_0^{b/r} e^{-z^2}dz - \int_0^{b} e^{-z^2}dz\Big]$$

that is also:

$$e^{b^2}\frac{\sqrt{\pi}}{2}\Big[\frac{2}{\sqrt{\pi}}\int_0^{b/r} e^{-z^2}dz - \frac{2}{\sqrt{\pi}}\int_0^{b} e^{-z^2}dz\Big]$$

which can be written as

$$e^{b^2}\frac{\sqrt{\pi}}{2}\Big[erf(b/r) - erf(b)\Big]$$

and substituting b and r

$$e^{b^2}\frac{\sqrt{\pi}}{2}\Big[erf\Big(\frac{y}{\sigma_y\sqrt{2(1-r^2)}}\Big) - erf\Big(\frac{y}{\sigma_x\sqrt{2(1-r^2)}}\Big)\Big]$$

so that:

$$\Delta y' = -\frac{4Nr_e e^{b^2}}{\gamma\sigma_x\sqrt{2(1-r^2)}}\frac{\sqrt{\pi}}{2}\Big[erf\Big(\frac{y}{\sigma_y\sqrt{2(1-r^2)}}\Big) - erf\Big(\frac{y}{\sigma_x\sqrt{2(1-r^2)}}\Big)\Big]. \quad \text{(A.8)}$$

Appendix B

General Expression for the Luminosity

It is derived here the generical expression of luminosity in the case of different beam sizes of the two interacting beams. Let's assume a Gaussian transverse density of the positron beam:

$$\rho_+(x,y) = \frac{N_+}{2\pi\ \sigma_{x+}\ \sigma_{y+}} exp[(-\frac{y}{\sqrt{2}\ \sigma_{y+}})^2 + (-\frac{x}{\sqrt{2}\ \sigma_{x+}})^2] \tag{B.1}$$

and analogously for the electron beam:

$$\rho_-(x,y) = \frac{N_-}{2\pi\ \sigma_{x-}\ \sigma_{y-}} exp[(-\frac{y}{\sqrt{2}\ \sigma_{y-}})^2 + (-\frac{x}{\sqrt{2}\ \sigma_{x-}})^2]. \tag{B.2}$$

Let's solve the integral

$$\int \rho_+ \rho_- dxdy \tag{B.3}$$

which is of course related to the luminosity by

$$\mathcal{L} = f \int \rho_+ \rho_- dxdy \tag{B.4}$$

where f is the revolution frequency. The integrals to solve are of the following kind:

$$\int e^{-at^2} dt = \frac{1}{\sqrt{a}} \int e^{-at^2} \sqrt{a} dt = \frac{1}{\sqrt{a}} \int e^{-z^2} dz = \sqrt{\pi a}. \tag{B.5}$$

It follows the generical expression of luminosity in the case of different beam sizes of the two interacting beams:

$$\mathcal{L} = f \cdot \frac{N_- N_+}{4\pi \sqrt{\frac{\sigma_{y-}^2 + \sigma_{y+}^2}{2}} \sqrt{\frac{\sigma_{x-}^2 + \sigma_{x+}^2}{2}}} \tag{B.6}$$

For the well-known case of equal beam sizes it is found the well-known result defined in Equation 2.4

$$\mathcal{L} = f\frac{N_- N_+}{4\pi\ \sigma_x\ \sigma_y} \tag{B.7}$$

The relation between the beam sizes of the two interacting beams can be found comparing Equations B.6 and B.7:

$$\sigma_y^2 = \frac{\sigma_{y-}^2\ +\ \sigma_{y+}^2}{2} \qquad \text{and} \qquad \sigma_{\mathrm{x}}^2 = \frac{\sigma_{\mathrm{x}-}^2\ +\ \sigma_{\mathrm{x}+}^2}{2} \tag{B.8}$$

Conclusions

A study of the beam-beam effect has been carried out in DAΦNE collider. This work has been particularly important in order to optimize the luminosity performances and beams stability in DAΦNE .

An analysis has been performed to find a working point for beam-beam collisions with a single interaction point during the DAΦNE commissioning. The influence on the luminosity and lifetime of the horizontal and vertical beam-beam separations at the second interaction point has also been investigated. Being the beam-beam interaction highly nonlinear detailed simulations have also been carried out in order to study the possible effects of closed orbit distortions (vertical angle, tilt angle, dispersion) at the interaction point. Also machine sextupole nonlinearities have been included in the simulations to evaluate the luminosity and lifetime degradation.

The proposed working point (5.150; 5.210) has been used successfully for the experimental runs before and after the KLOE installation.

A detailed study has been carried out to find a working point for two interaction points operation. In this case for a given working point the phase advance between the two interaction points has been found to be an important parameter that can be tuned in order to optimize luminosity and lifetime. Simulations show that the working point (5.150; 5.210) can be used also in two interaction points operation.

A comparison of beam-beam simulations with experimental results has led to a deeper understanding of the beam-beam interaction in the DAΦNE collider. Luminosity and lifetime results from the simulation scans around the working point (5.150; 5.210) are in good agreement with experimental observations. Beam-beam measurements have been discussed and compared to simulation results. In particular the vertical beam-beam blow up has been observed when a relative transverse angle between the beams is introduced. The beam-beam effect has also showed up as Landau damping of the two interacting beams in multibunch operation and it has been used to stabilize the beams. The beam-beam tune shift has been measured

from the coherent beam-beam effect and is now about $\xi_x \sim 0.02$ and $\xi_y \sim 0.015$, in agreement with the expected values from the luminosity measurements.

Acknowledgments

I would like to thank the DAΦNE project leader Gaetano Vignola for giving me the opportunity to study beam-beam interaction effects in the DAΦNE collider.

I also thank my academic advisor at the University of Rome 'La Sapienza' Luigi Palumbo for his guidance and support.

I am very grateful to Mario Bassetti for helping me gain an understanding of the beam-beam interaction and for the valuable time I spent working with him.

I would also like to thank Mikhail Zobov for his assistance and valuable advice in the course of my learning the tools of the work.

I wish to thank Miro Preger for his very precise comments and suggestions during the writing of this dissertation.

My discussions with Caterina Biscari always proved to be helpful. I acknowledge all the people in the Accelerator Division at Frascati whom have helped me in many ways during my research work, in particular Mario Serio, Susanna Guiducci, Andrea Ghigo, Fernando Sannibale.

Bibliography

[1] G.Vignola and DAΦNE Project Team, DAΦNE *: The First Φ-Factory*, in Proc. of 5th EPAC, Sitges (Spain), June 1996, p.22

[2] The KLOE collaboration, *KLOE, a General Purpose Detector for DAΦNE* Frascati Internal Note LNF-92/109, April 1992

[3] The FINUDA collaboration, *FINUDA, a detector for nuclear physics at DAΦNE*, Frascati Internal Note LNF-93/021, May 1993

[4] The DEAR Collaboration, *The DEAR Proposal*, LNF-95/055(IR), (1995)

[5] M.Sands, *The Physics of electron storage rings, an introduction*, SLAC-121, May (1979)

[6] F.Sannibale for the DAΦNE Comm. Team, *Luminosity Optimization in* DAΦNE , in Proc. of DIPAC99, Chester (1999)

[7] S.Bartalucci et al., DAΦNE *Storage Ring* in Proc. PAC91, San Francisco (1991), pag.2850

[8] A. Alavi-Harati et al., Phys. Rev. Lett. 83 (1999) 22.

[9] The NA48 Collaboration: V. Fanti, et al.,Phys.Lett. B465 (1999) 335-348

[10] E.D.Courant and H.S.Snyder, *Theory of the AG synchrotron*, Ann.Phys.3 (1958)

[11] M.Bassetti, private communications

[12] M.Bassetti, *Numerical Computations of space charge effects in a positron and electron storage ring* in Proc. 5th Int.Conf. on High Energy Particle Accelerators, Frascati (1965).

[13] S.Kheifets, *Potential of a three-dimensional Gauss bunch*, PETRA Note 119 (1976)

[14] M.Bassetti and G.A Erskine, *Closed expression for the electrical field of a two-dimensional Gaussian charge*, CERN-ISR-TH/80-06 (1980)

[15] H.Mais, C.Mari, *Introduction to Beam-Beam Effects*, DESY M-91-04 (1991)

[16] S.Tazzari,*Beam-Beam Effects at the 1.5 GeV e^+e^- Storage Ring ADONE*, AIP Conf.Proc.N.57, BNL (1979)

[17] W.Herr, *Experience with beam-beam effects in LEP* in Proc. of LHC99, CERN-SL-99-039 AP, Geneva (1999)

[18] B. V. Chirikov, *A Universal Instability of Many-Dimensional Oscillator Systems*, Phys. Rept. 52 (1979).

[19] T.Chen,J.Irwin and R.H.Siemann, *The Effect of Phase Advance Errors Between Interaction Points on Beam Halos*, in Proc. of the 16th IEEE PAC95 and International Conference on High Energy Accelerators, Dallas, Texas, 1-5 May 1995, pp.2913-2915.

[20] R.D.Ruth, *Single Particle Dynamics and nonlinear resonances in circular accelerators*, SLAC-PUB-3836, (1985)

[21] H. Bruck, *Accelerateurs circulaire de particules*, Presses Universitaires de France, Paris (1968)

[22] R. Siemann, *The beam-beam interaction in e^+e^- storage rings*, Proc. Joint US-CERN School on Particle Accelerators, Spain October (1992)

[23] M. E. Biagini and M. Zobov, DAΦNE *8th Machine Review*, Frascati February 1995

[24] A.A. Zholents, *Beam-Beam Effects in Electron-Positron Storage Rings*, Proc. Joint US-CERN School on Particle Accelerators, Hilton Head Island November 1990

[25] B. Podobev, R. Siemann, SLAC-PUB-6705, Oct. (1994)

[26] D.Shatilov, *Beam-Beam simulations at large amplitudes and lifetime determination* Part.Acc,1996, Vol.52,pp.65-93

[27] T.Chen at al., *Comparison of beam-beam simulations*, in Proc.of VII ICFA Beam Dynamics Workshop, Dubna (1995)

[28] E.Simonov, undocumented code TURN

[29] K.Ohmi, *Strong-strong Simulation for beam-beam effect in KEKB* in Proc. of the Int. Workshop on Performance Improvement of e+e- Collider Particle Factories, KEK in Tsukuba, Japan (1999)

[30] K. Hirata and M. Zobov, *Beam-beam interaction study for* DAΦNE in Proc. of 5th EPAC, Sitges (Spain), June 1996,pp. 1158-1160

[31] M.Boscolo, M.Zobov and D.Shatilov, *Beam-Beam interactions at the working point (5.15; 5.21)* DAΦNE Technical Note G-51, March 1999

[32] A.Verdier, *Chromaticity* in Proc. of CAS 5th Adv. Course, CERN 95-06, Vol.1 (1995)

[33] K. Hirata, Phys. Rev. Lett. 74, 2228 (1995)

[34] A.Gallo et al., in Proc. of PAC99, New York (1999)

[35] D.H.Rice and J.T.Haylas, *Optimization of Specific Luminosity in CESR*, in Proc. of the Int. Workshop on Performance Improvement of e+e- Collider Particle Factories, KEK in Tsukuba, Japan (1999)

[36] M.E.Biagini,C.Biscari, S.Guiducci, DAΦNE *Main Rings Lattice Update*, DAΦNE Techn. Note L-22, March (1996)

[37] S.Guiducci for the DAΦNE Comm.Team, DAΦNE *Operating Experience*, in Proc. of PAC99, New York (1999)

[38] C.Biscari et al., DAΦNE *beam-beam measurements*, DAΦNE Technical Note BM-4, Sept. 1999

[39] A.Piwinski, *Observation of beam-beam effects in PETRA*, IEEE Trans. on Nucl. Sc., Vol. NS-26, No. 3, June 1979

[40] K.Yokoya et al.,*Tune shift of coherent beam-beam oscillations*, KEK Preprint 89-14, May (1989)